Research Grant NsG-306-63

National Aeronautics
and Space Administration

PULSED ELECTROMAGNETIC GAS ACCELERATION

Eleventh Semi-Annual Progress Report
1 July 1967 to 31 December 1967

Report 634j

Prepared by:___*Robert G. Jahn*_____
                Robert G. Jahn
                Professor and
                Research Leader

and:___*Woldemar v. Jaskowsky*___
        Woldemar F. von Jaskowsky
            Research Engineer
            and Lecturer

January 1, 1968

Guggenheim Laboratories for the Aerospace Propulsion Sciences
Department of Aerospace and Mechanical Sciences
Princeton University
Princeton, New Jersey

Abstract

The previously reported phenomenon of current sheet transition from a propagating "sweeping" mode to a quasi-steady "blowing" mode has been studied in detail in a parallel plate accelerator with partially insulated electrodes, and in a coaxial MPD arc configuration. In the parallel plate device, a related sequence of magnetic and electric probe surveys, Kerr-cell photographs, inner and outer voltage signatures concur on a model of the transition process which invokes incompletely accelerated gas passed over by the propagating sheet as a starting inflow for the later, steady acceleration phase. The characteristic time for attainment of steady gasdynamic flow through the arc from an external reservoir considerably exceeds that for stabilization of the discharge current pattern, thus requiring longer driving current waveforms and more sophisticated gas injection procedures to achieve complete simulation of a steady flow accelerator. In the MPD simulator, this is achieved by a modification of the capacitor pulse line to provide longer duration, lower amplitude driving pulses, and by a coaxial, shock tube gas injection system appropriately synchronized with the the electrical pulse. Early results of this experiment indicate that such complete stabilization can essentially be achieved, including prolific thermionic emission from the cathode on the available time scale. Experimental maps of current distribution throughout the discharge indicate that under the conditions studied, some one-third of the arc current flows in the exterior plume and attaches far out on the anode surface.

The program to optimize energy transfer from a pulse line to an accelerating current sheet has revealed the anticipated strong, nonlinear interaction between the dynamics of the circuit and that of the plasma. As the impedance of the

driving line is brought down toward that of the accelerating plasma, the current waveform is observed to distort considerably, and the relative duration of pulse length to plasma propagation time also becomes important to optimization of energy transfer, in addition to the impedance ratio.

High-speed pressure transducer studies, supplemented by photographic and interferometric techniques continue to reveal interesting aspects of current sheet structure. One particularly interesting feature is the origin and growth of the peculiar "anode-foot" interaction which may have some relevance to the troublesome anode loss mechanism in MPD arcs.

CONTENTS

LIST OF ILLUSTRATIONS

CURRENT STUDENT PARTICIPATION

Student	Period	Degree	Thesis Topic
BRUCKNER, Adam P.	1966-	Ph.D. Cand.	Gas Laser Interferometry of Closed Chamber Discharges
CLARK, Kenn E.	1965-	Ph.D. Cand.	Magnetoplasmadynamic Arc Simulation
DI CAPUA, Marco S.	1966-	Ph.D. Cand.	Current-voltage Characteristics of High Current Discharges
ECKBRETH, Alan C.	1964-	Ph.D. Cand.	Stabilization of a Current Sheet for Quasi-Steady Plasma Acceleration
OBERTH, Ronald C.	1966-	Ph.D. Cand.	Current Sheet Anode Foot Phenomena
TURCHI, Peter J.	1963-	Ph.D. Cand.	Unsteady Plasma Diagnostics
WILBUR, Paul J.	1966-	Ph.D. Cand.	Optimization of Energy Transfer to Accelerating Plasmas
YORK, Thomas M.	1965-	Ph.D. Cand.	Gas Pressure Distributions in Accelerating Plasmas

I. INTRODUCTION

Over the past several months, the major emphasis of the laboratory program has continued to shift from the simpler closed-chamber studies which characterized the early efforts, toward more sophisticated experiments on more elaborate apparatus capable of long-pulse and/or plasma ejection operation. Partially this is attributable to a maturing of understanding of the more elementary phenomena, but more essentially to the overall predisposition of the work to ultimate propulsion application. While some closed-chamber studies remain, these largely are reserved for development of new diagnostic techniques, or for preliminary examination of new concepts in the plasma acceleration processes. The more extensive efforts are now focused on programs such as MPD simulation, current sheet stabilization, and optimization of energy transfer from power source to accelerating plasma which bear more directly on the ultimate engineering realities of plasma propulsion.

The composition of this status report reflects this trend in the laboratory program. The three major topics just mentioned are discussed first, each in some detail. These are followed by a review of the high-speed pressure probe studies which are nearing completion, and by a discussion of the latest "anode-foot" results which seem to have considerable implication for both pulsed and steady thruster performance. More preliminary results of a gas laser interferometer technique for electron density measurements, and of an experiment to map current-voltage characteristics of very high current arcs are included briefly to provide some flavor of the overall program.

Two special items are included in the Appendices. First, this laboratory was honored last fall by the award

to one of its undergraduates, Mr. Peter J. Turchi, of the
National AIAA Student Research Prize, at the Annual Meeting
of the Institute in Anaheim. The text of his winning paper,
soon to be published in the AIAA Student Journal, is in-
cluded intact in Appendix I.

During the past summer, this same student conducted
a detailed bibliographical survey of diagnostic techniques
appropriate to pulsed plasma acceleration. The resulting
series of abstracts and commentaries has proven useful in
the indoctrination of new students into the laboratory pro-
gram here, and is available in full to any member of the
distribution list who cares to request it. The procedure
and references followed are outlined in Appendix II.

II. TRANSITION FROM UNSTEADY TO STEADY PLASMA ACCELERATION IN A RECTANGULAR CHANNEL
(Eckbreth)

The previously reported preliminary observations of spontaneous transition of a propagating, gas-sweeping current sheet to a stationary, gas-pumping current distribution in a parallel plate accelerator,[48,49] have been verified in a more precise and detailed series of experiments. The parallel plate device, shown in Fig. 1 and described in detail in Ref. 48 has now been equipped with a pair of aluminum electrodes permanently inlaid with 1/4" thick nylon insulation over all but the first 5-1/4" of their length. The acceleration channel formed by these electrodes thus has a sharp conductor-insulator discontinuity about 2.6 channel heights downstream of the discharge initiation position, which serves to arrest the propagation of the current sheet along the electrodes, and thereby eventually to stabilize the entire discharge conduction pattern.

The accelerator now is also equipped with a variety of probe access glands and interior supports which permit detailed electric, magnetic, and gasdynamic probing of the entire discharge pattern. Also, a shock tube gas injection system, shown in Fig. 2, has been added as a means to provide mass flow to the stabilizing current pattern, or to study the effect of ambient pressure gradients on the stabilization process. The shock tube consists of a 3" diameter x 6" long driver section with a diaphragm plunger, connected to a 12" Plexiglas driven section through a large ball valve. The end wall of the driven section feeds 5 tubes, 4 of which connect via holes in the backstrap to orifices in the rear wall of the accelerator channel, and 1 of which supplies a gas trigger pulse to the switch.

Using the above equipment, the transition from a

RP25 IC 4350 68

INSULATOR

METAL TO
INSULATOR JUNCTION

5.3"

6"

+X

−X
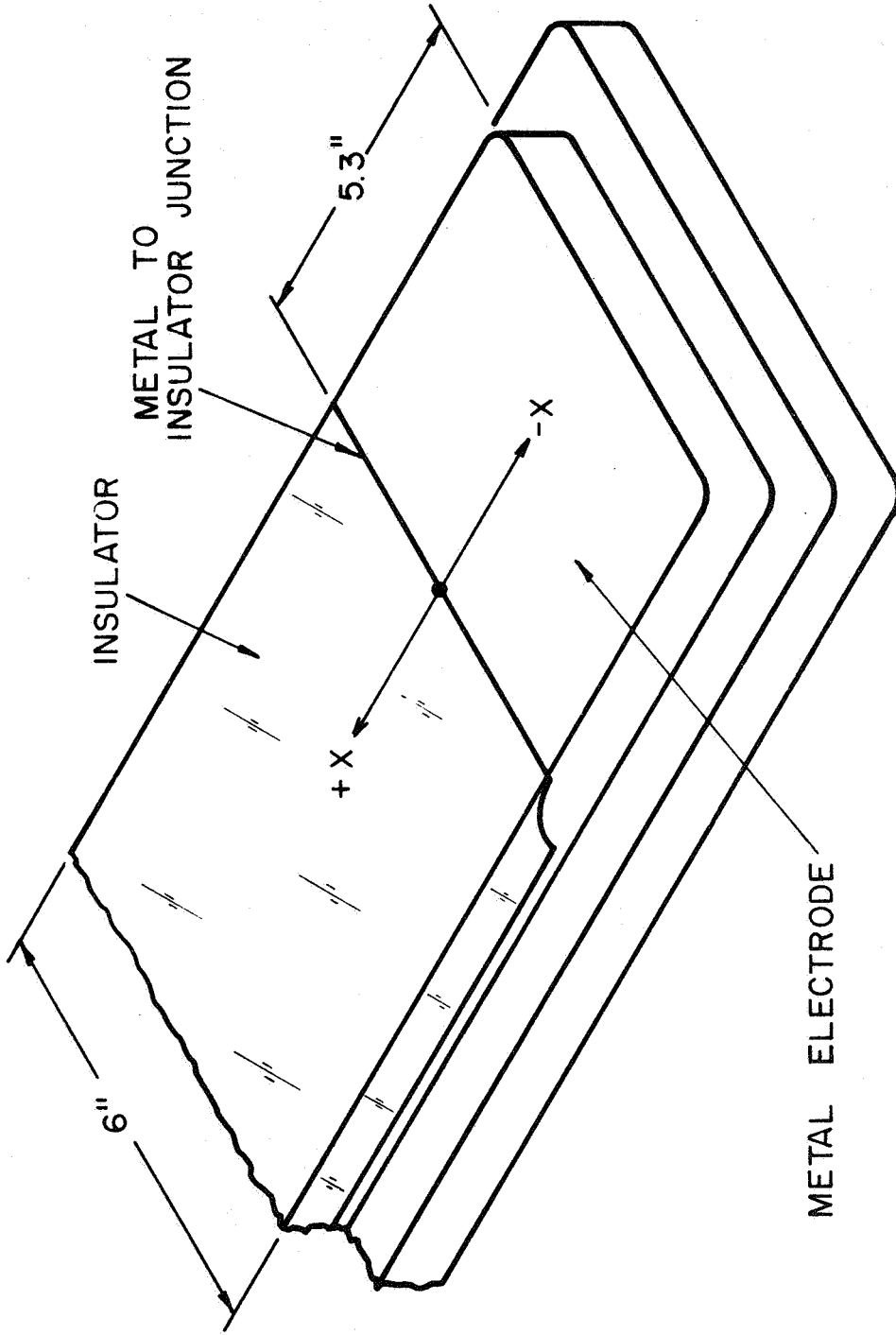
METAL ELECTRODE

METAL ELECTRODE WITH INLAID INSULATION

FIGURE I
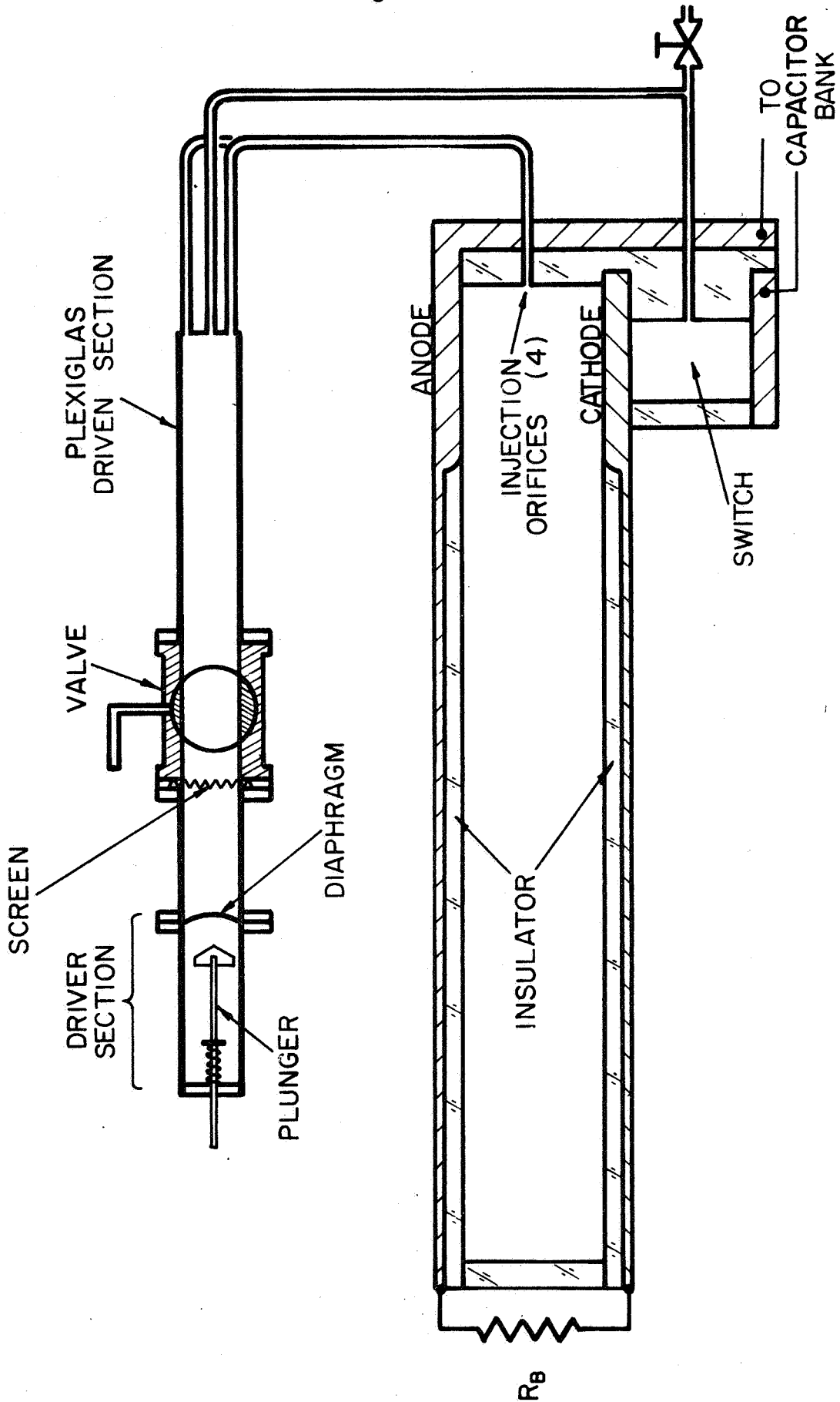
SHOCK TUBE GAS INJECTION SYSTEM

FIGURE 2

sweeping current sheet to a stabilized current distribution has been examined with a variety of diagnostics, including magnetic probes, voltage probes, electric field probes, and Kerr cell photography of the discharge patterns and of the plasma flow over miniature wedges. The current pulse used in all of these studies (except where otherwise noted) is rectangular in form, 120,000 amperes in magnitude with a 20 μsec duration. In the results to be displayed, the reference system employs x as the axial coordinate, such that the metal to insulation junction is at x = 0. x > 0 runs downstream along the insulation and x < 0 runs upstream along the metal electrode to the back wall where the discharge initiates. Kerr cell photographs of the propagating current sheet are shown in Fig. 3, while the transition from a propagating sheet to a stabilized distribution is shown in Fig. 4. Note that the current sheet initiates at the back wall (x = -5-1/4") and propagates down the channel with a slight forward tilt from cathode to anode, and with an evergrowing "anode foot." Upon reaching the metal to insulation junction, the bulk of the luminosity pattern continues to propagate into the insulated channel, unrolling, as it were, the stabilized pattern of two broad, nearly axial and highly luminous bands emanating from the electrode discontinuity. The visual simularity of these bands to the anode and cathode jets of the MPD arc is one suggestion of valid simulation of steady arc phenomena in this type of experiment.

The development of the corresponding patterns of discharge current distribution is presented in Figs. 5a-5e in the form of enclosed current contours at a succession of times during the pulse. Again we see the slight tilt of the propagating current sheet, its broader anode attachment region, and its abrupt, balloon-like arrest at the electrode discontinuity. The stabilized pattern bows downstream in a hairpin fashion with the bulk of the current conducted across the mid-

ANODE

A 894

1 μ sec

CATHODE

A 892

2 μ sec

A 891

3 μ sec

X ← -2.9"   -5.3"

A 897

4 μ sec

A 898

5 μ sec

X ← 0.38" 0   -2.1"
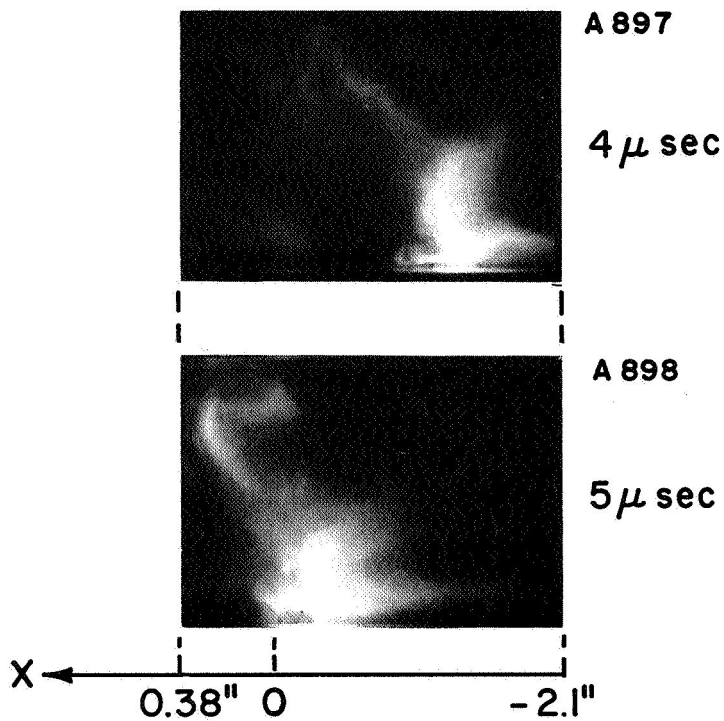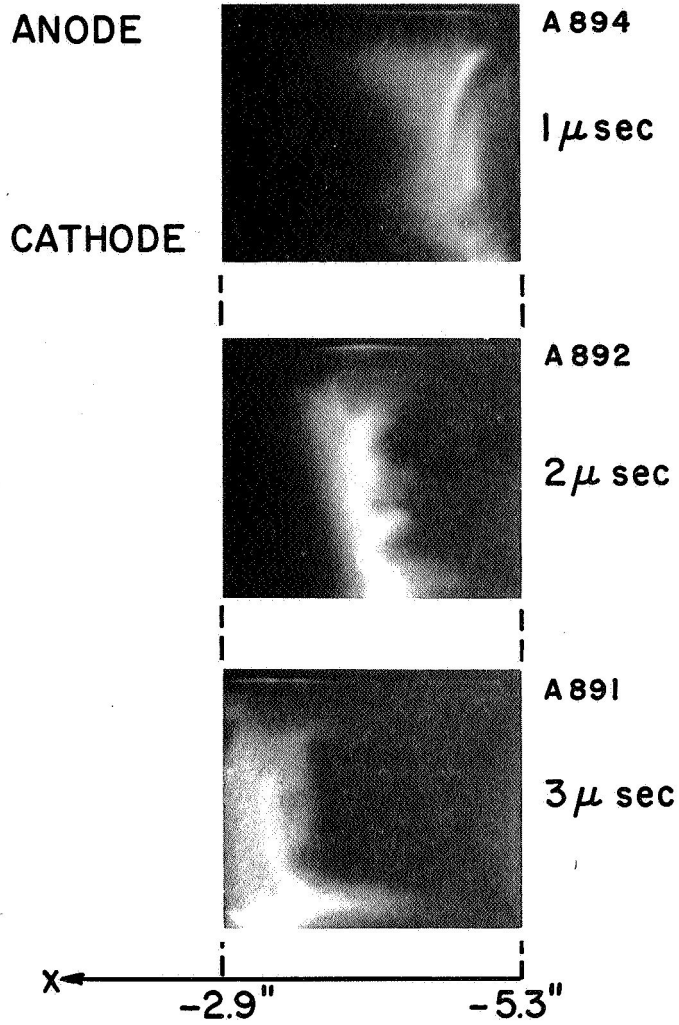
KERR CELL PHOTOGRAPHS OF PROPAGATING
CURRENT SHEET

FIGURE 3

A 904 8 A 907
5 μ sec 10 μ sec

A 903 A 911
6 μ sec 12 μ sec

A 902 A 910
7 μ sec 14 μ sec

A 905 A 909
8 μ sec 16 μ sec

A 906 A 908
9 μ sec 18 μ sec

X ← +1.13" O   X ← +1.13" O
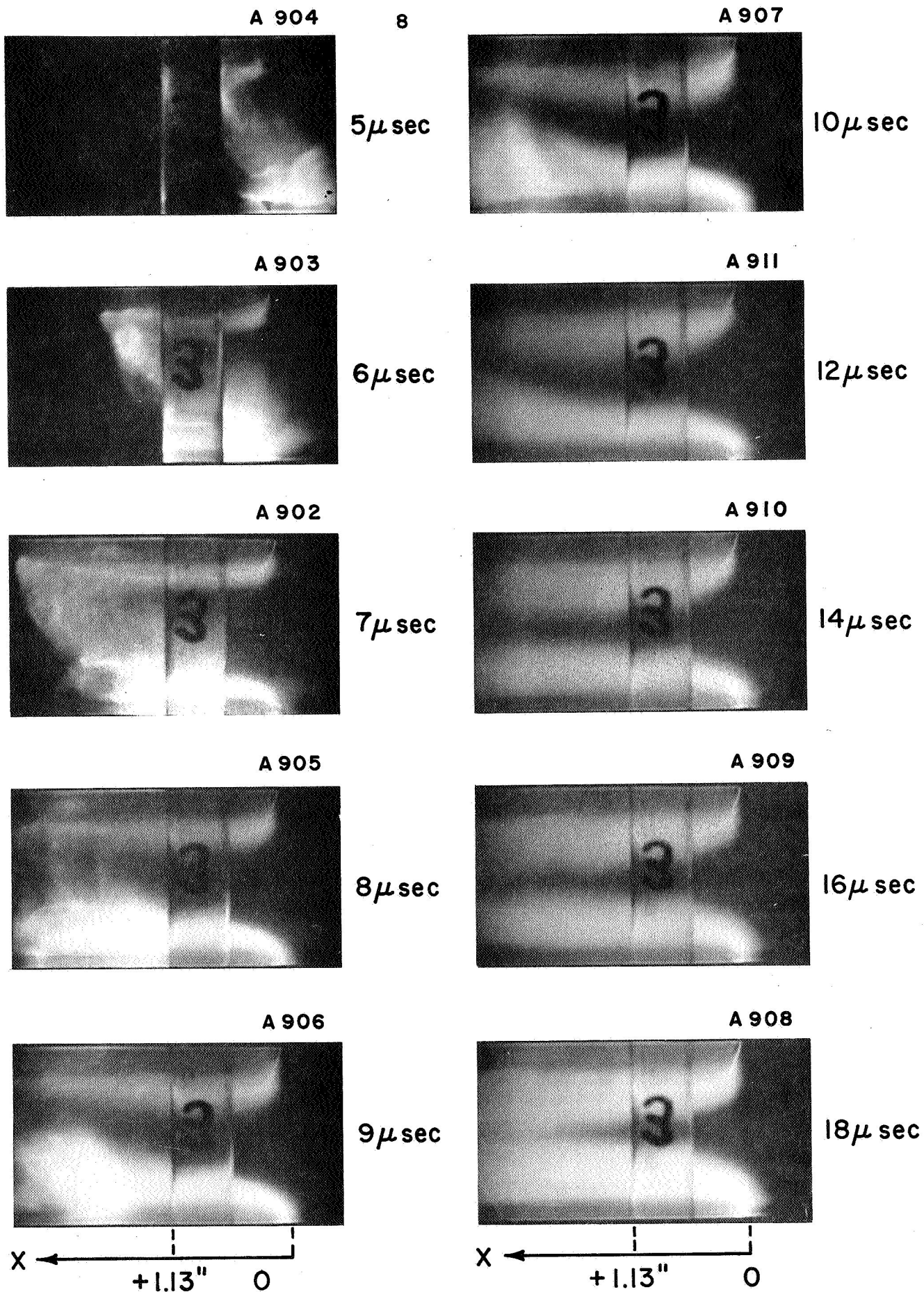
KERR CELL PHOTOGRAPHS OF TRANSITION
TO STABILIZED CURRENT DISTRIBUTION

FIGURE 4

X=-5.3

X=0

X=+4

INSULATION

120

100

80

60

40

20

t = 2 μ sec

120

100

80

60

40

20

t = 4 μ sec

ENCLOSED CURRENT CONTOURS (K-Amp) IN PARALLEL PLATE ACCELERATOR
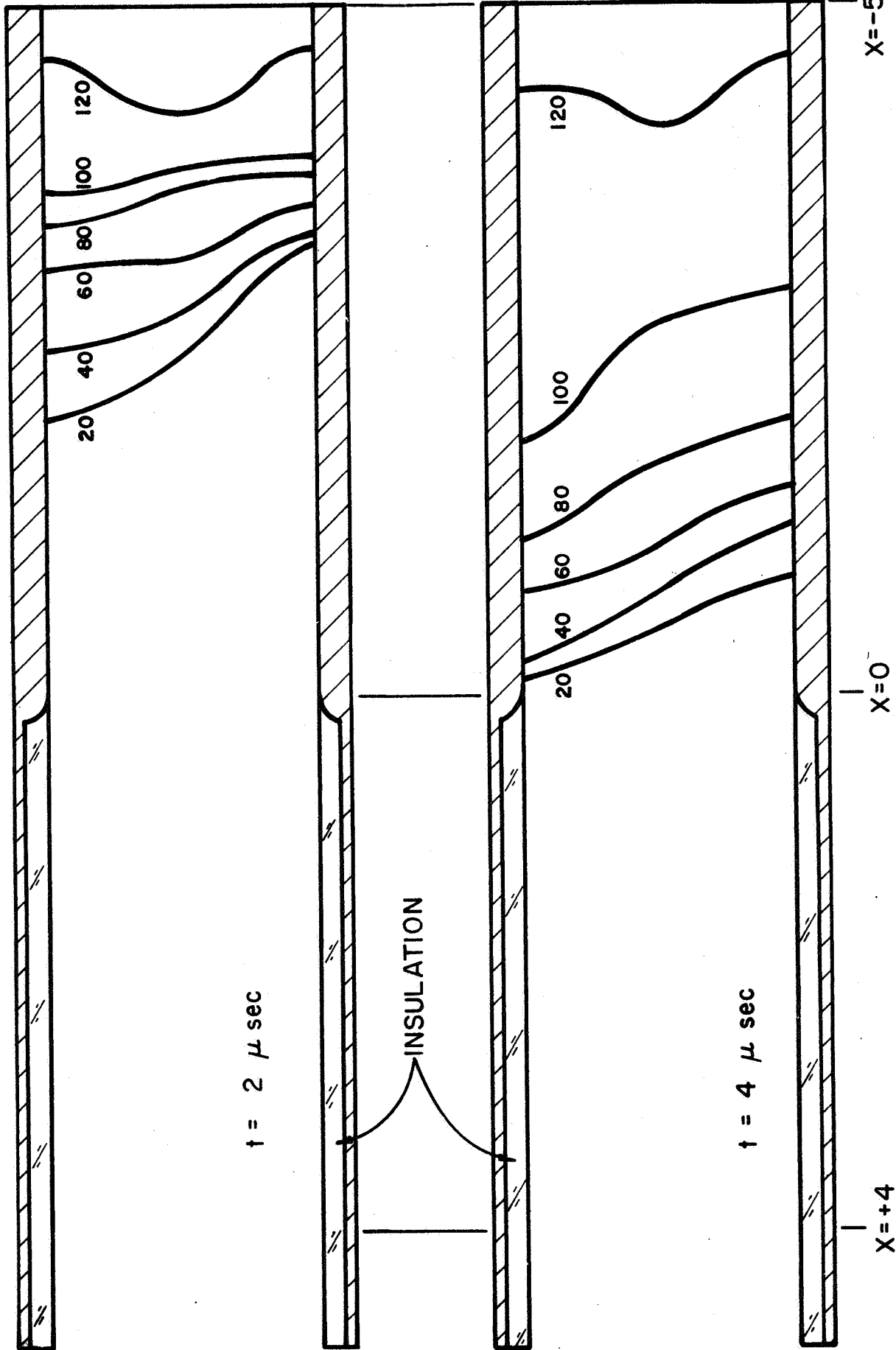
FIGURE 5a

FIGURE 5b

ENCLOSED CURRENT CONTOURS (K-Amp) IN PARALLEL PLATE ACCELERATOR
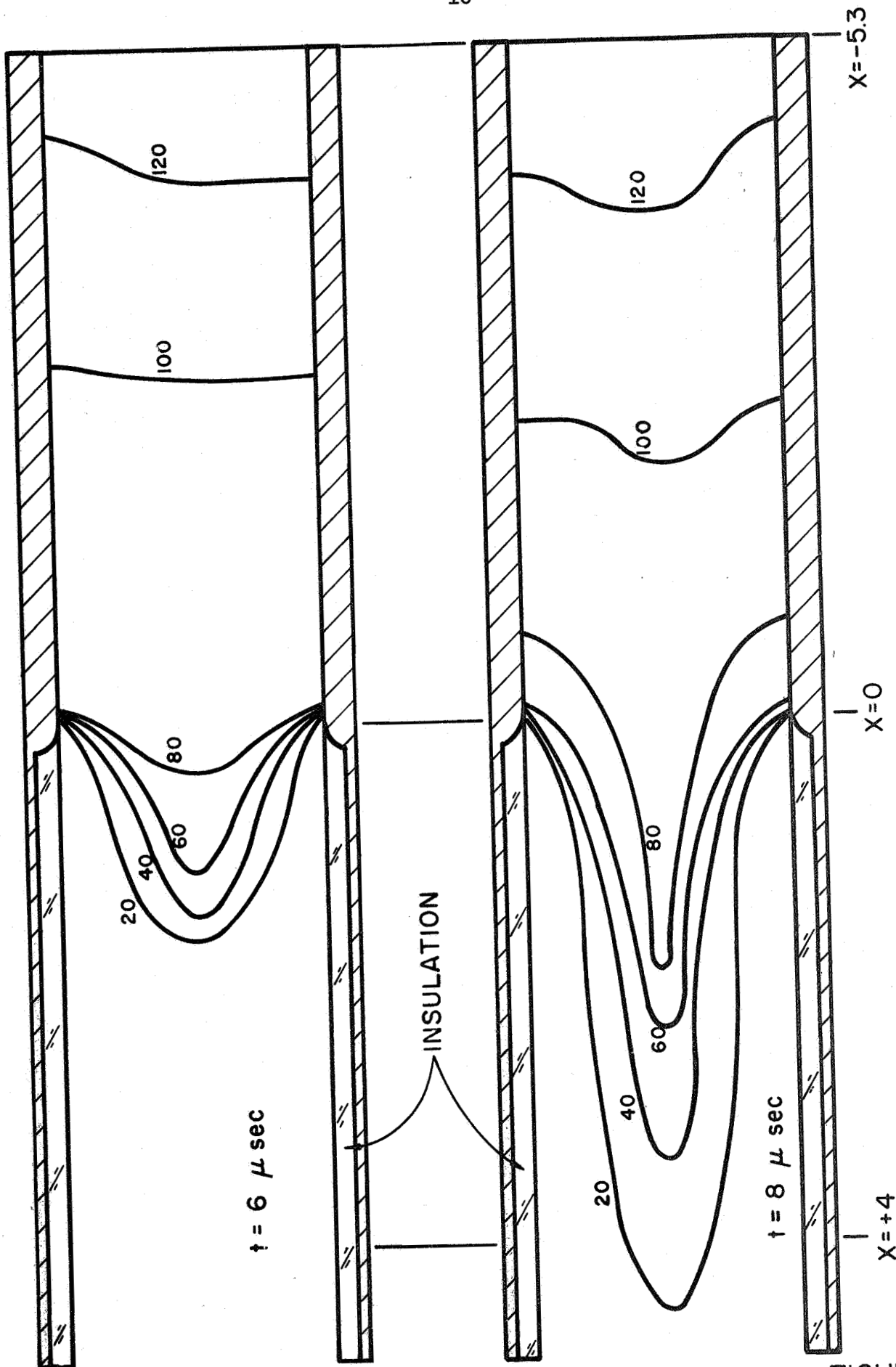
ENCLOSED CURRENT CONTOURS (K-Amp) IN PARALLEL PLATE ACCELERATOR
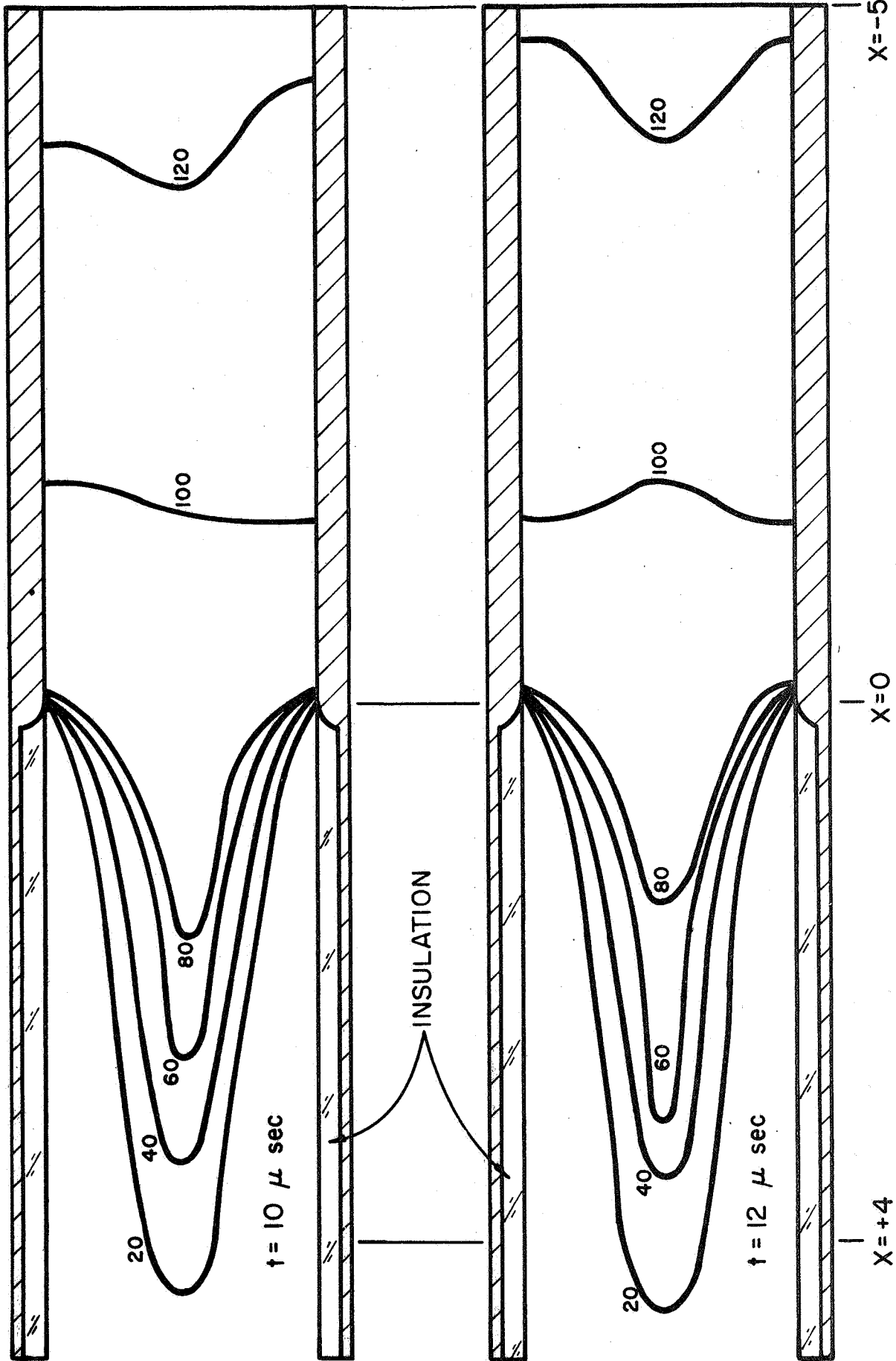
FIGURE 5c

ENCLOSED CURRENT CONTOURS (K-Amp) IN PARALLEL PLATE ACCELERATOR
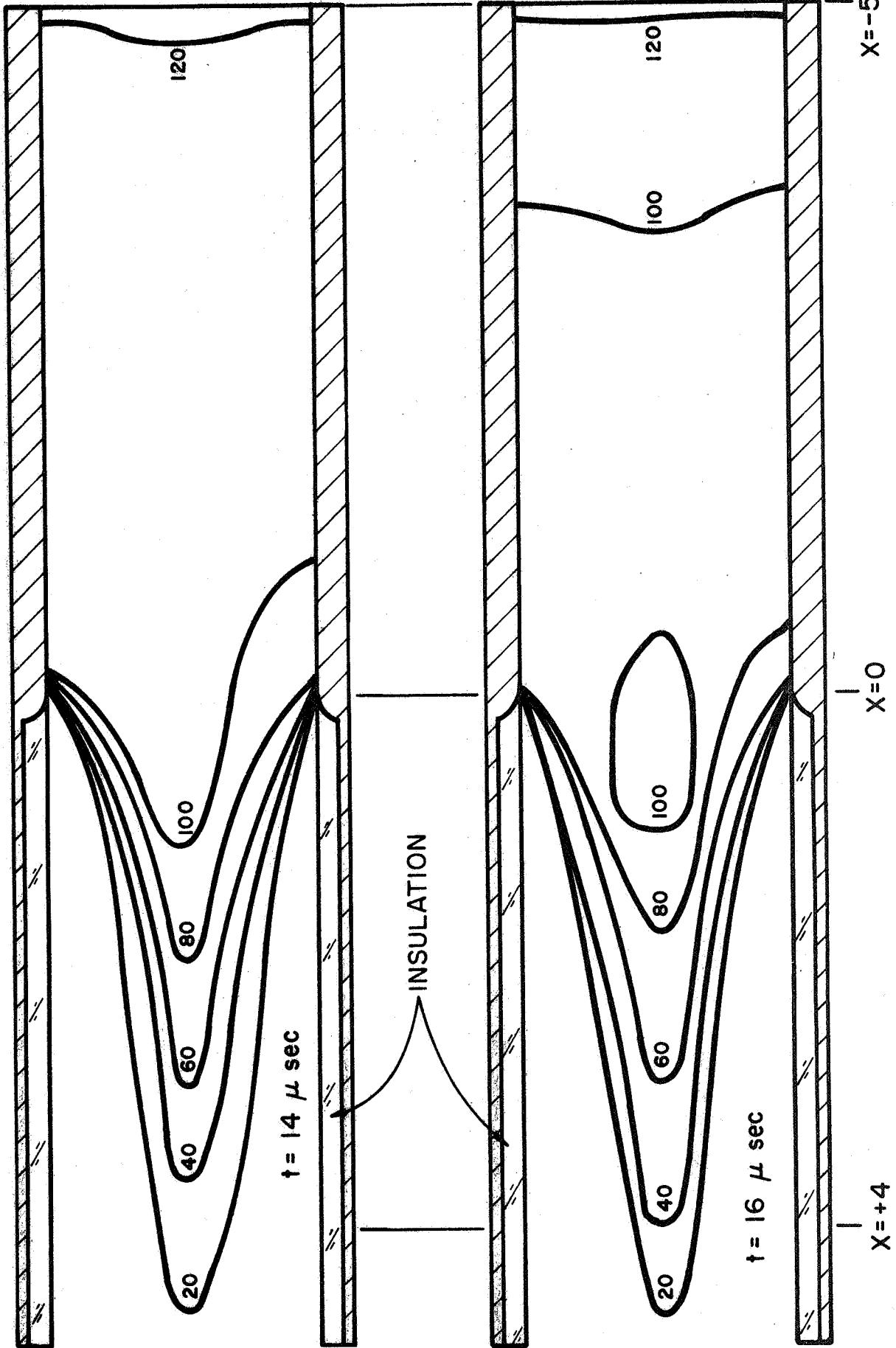
FIGURE 5d

13

x=-5.3

80

80

80

60

40

20

x=0

t=18 μ sec

INSULATION

x=+4
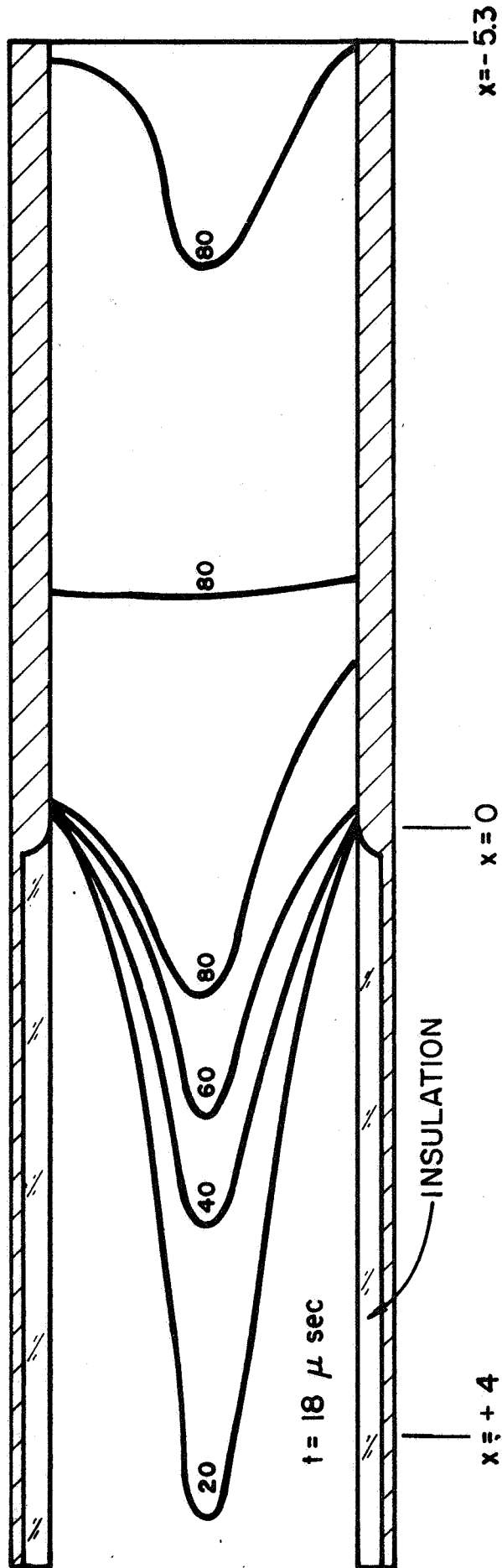
ENCLOSED CURRENT CONTOURS (K-Amp) IN PARALLEL PLATE ACCELERATOR

FIGURE 5e

plane in the 0 < x < 6" region, i.e., within three channel
heights downstream of the metal-to-insulation junction.

Although the current has ceased to propagate, accel-
eration of gas by the stabilized current distribution appears
to continue. The most vivid demonstration of this is a photo-
graphic sequence of flow patterns over small 15° half angle
wedges set in three planes--1/4 inch off the anode and cath-
ode and in the midplane--at various axial positions along
the channel. For example, the status of the inlet flow to
the stabilized current distribution can be observed by wedges
upstream of the current stabilization region; such a series
of pictures taken at 10, 14, and 18 μsec respectively is
shown in Fig. 6 where the wedge tips are located at approxi-
mately x = -1-3/8 inch. Note that shocks are visible at each
of these times indicating that the inflow is supersonic over
the stabilized portion of the current pulse. Note also, how-
ever, that the luminosity of these shocks decreases with
time suggesting that the mass flow into the stabilized cur-
rent zone is decreasing.

Figure 7 displays the flow over the wedges at
x = + 2-3/8", + 5-5/8", and + 8-3/8" for a series of times
during the pulse. Comparing these positions with the patterns
of enclosed current shown earlier, one sees that they corre-
spond respectively to the middle of the stabilized current
zone, to the downstream fringe of the current zone, and to
a completely exterior position. At the three times shown,
14, 16, and 18 μsec, it is apparent that the Mach number
of the flow increases downstream through the stabilized
current zone. At the first position, the shocks are some-
what detached; at the second, the shocks are attached; and
at the third they are yet more inclined to the flow. Fur-
ther interpretation is somewhat ambiguous since either a flow
acceleration or a decrease in the local sound speed could
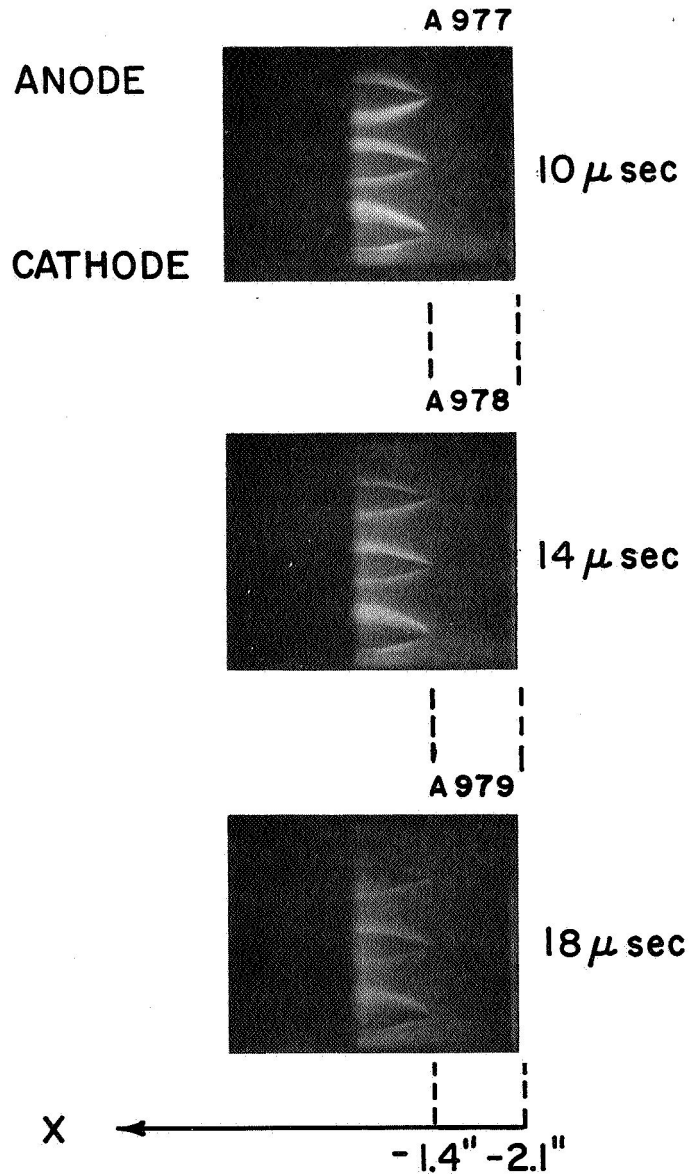
AIRFOIL VISUALIZATION OF GAS FLOW
INTO STABILIZED CURRENT DISTRIBUTION

FIGURE 6

A 965   14 μ sec

A 964   16 μ sec

A 963   18 μ sec

A 951

A 950

A 948

A 985

A 983

A 982

ANODE

CATHODE

1.1"   2.4"   3.7"

4.4"   5.7"   6.9"

8.8" 7.7"

X
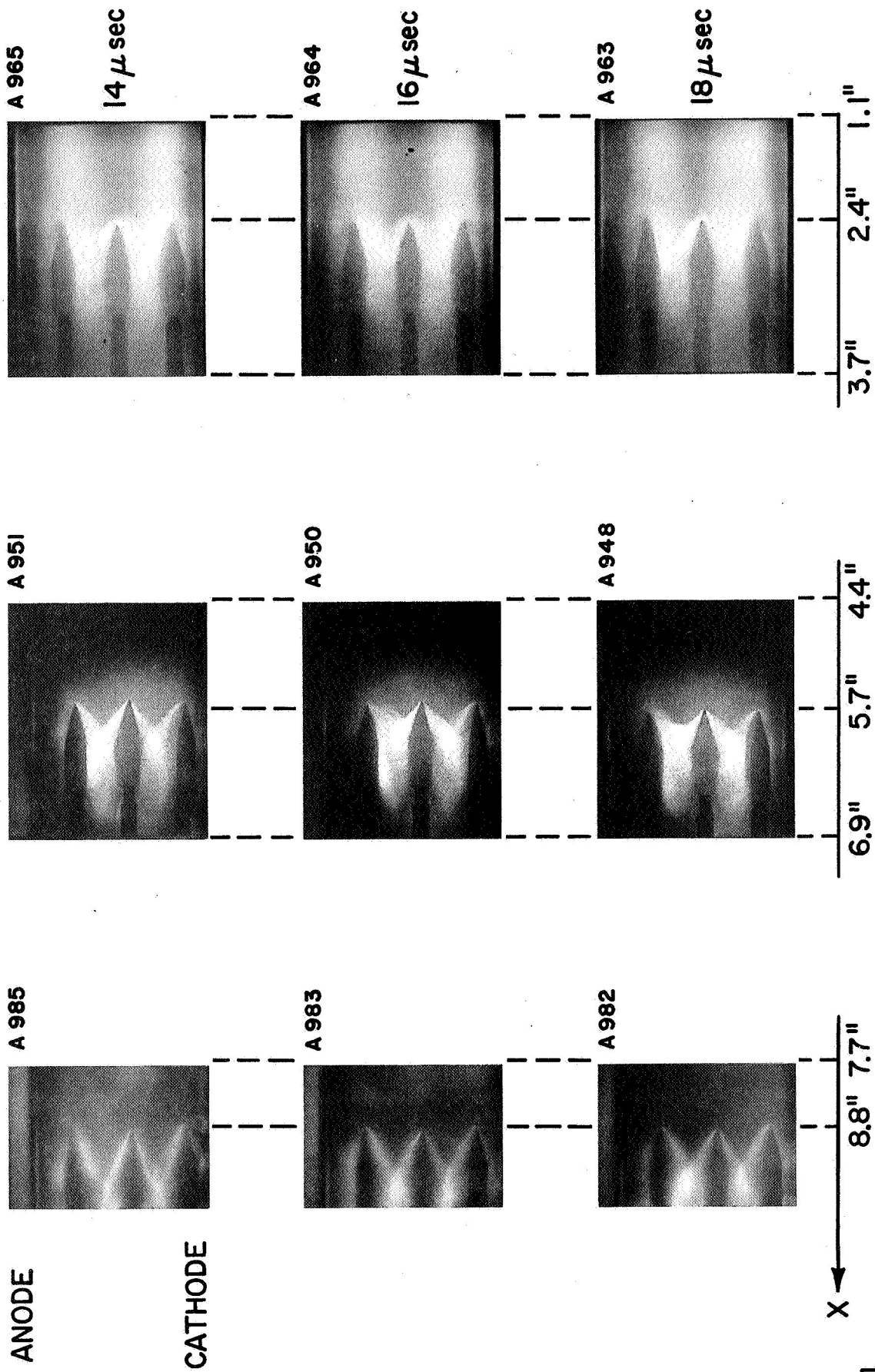
AIRFOIL VISUALIZATION OF GAS FLOW THROUGH
STABILIZED CURRENT DISTRIBUTION

FIGURE 7

produce the observed Mach number increase. However, since
the effect of joule heating in the current zone would tend
to raise, rather than to lower the sound speed, and since
the similarity in probe responses at the three transverse
positions speaks against major transverse gradients and
excessive wall cooling, a valid flow acceleration through
the current zone seems the more likely alternative.

Supporting evidence for the continued acceleration of
gas through the stabilized current zone is provided by voltage
signatures of an inner divider and of an exterior probe across
the electrodes at the far downstream end (see Ref. 48). In
Fig. 8a is shown the inner divider signature at $x = -2-1/4"$
indicating a plasma resistive drop of 50 to 60 volts (corre-
sponding to a plasma resistance of .0005 Ω), followed in
succession by a $\dot{\phi}$ contribution as the sheet sweeps by, and
then by a $\vec{u} \times \vec{B}$ back emf as $\dot{\phi}$ vanishes during the stabilization
sequence. If this is truly a steady process, only the resis-
tive drop and the $\vec{u} \times \vec{B}$ contribution should appear at the
front end of the device and Fig. 8b shows that this is indeed
the case. Here the voltage climbs gradually from the resis-
tive level at breakdown to the same steady $\vec{u} \times \vec{B}$ value as the
pattern stabilizes.

In an effort to unravel a bit more of the mechanisms
of gas acceleration in the two phases, attempts have been
made to map the patterns of electric field within the current-
carrying regions of the plasma. Both coaxial probes to measure
the axial (x) fields, and forked probes to measure the trans-
verse (y) fields have been employed, but only the former has
sofar proven sufficiently reproducible to encourage any inter-
pretation. The probe response along the metal electrode
portion of the channel (x < 0) corresponds to that commonly
observed for a propagating current sheet in a closed chamber
pinch discharge, namely, a "spike" of forward facing electric
field, followed by a weaker region of field reversal. An

a) INNER DIVIDER AT X = -2.3"

b) VOLTAGE ACROSS R_B
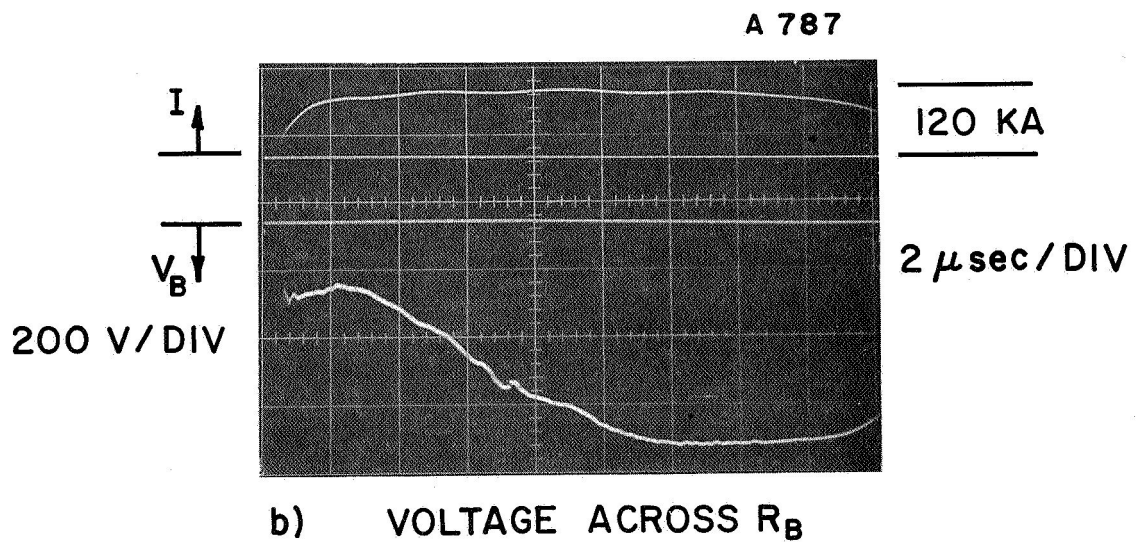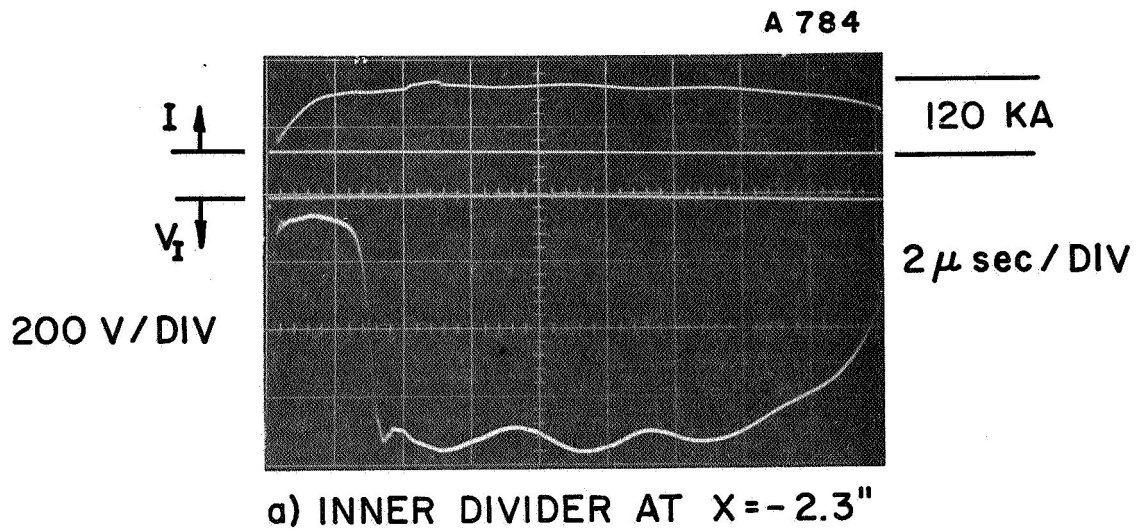
VOLTAGE SIGNATURES OF CURRENT
SHEET STABILIZATION

FIGURE 8

example of such a signal taken at $x = -3-1/4$" is shown in Fig. 9a. In contrast, Figs. 9b,c,d show typical electric probe responses at three positions in the midplane of the stabilized current distribution downstream of the metal to insulation junction ($x > 0$). The dominant features here consist of a vestige of the current sheet spike, followed by a null period, followed by a step function increase in E_x lasting until the end of the pulse, of magnitude decreasing with distance down-stream of the discontinuity. Arrival times of the spike and onset of the plateau region have been plotted as a function of position in Fig. 10.

One may speculate that the first spike of E_x recorded by the probe announces the arrival of the snowplowed plasma accumulated by the propagating sheet upstream in the con-ducting portion of the channel, now continuing on its own inertia as the sheet is arrested near the discontinuity and diffuses into the quasi-steady conduction pattern. The plateau of electric field prevailing over the latter portion of the response presumably reflects the quasi-steady flow acceler-ation process in operation, possibly as a Hall voltage compo-nent of the total electric field. The rather well-defined null time between these two signals is somewhat puzzling, particularly since no correspondingly abrupt processes are evident in the development of the discharge current distri-bution in this region (see Fig. 5). Possibly this stems from a momentary void of mass flow supply to the accelerating region in the wake of the current sheet, but clearly much more information is needed to complete this model. Indeed, one may question how mass flow is provided for the stabilized phase at any time, if the propagating sheet has effectively swept out the ambient fill of the conducting portion of the channel. Actually, current sheets of this intensity are known from earlier work to be imperfect "sweepers" (Refs. 11,12,29), a fact confirmed by the observed magnitude of E_x spike too

20

2 μ sec/DIV

120 KA

50 V/cm

A 876

a) x = -3.3", MIDPLANE

120 KA

20 V/cm

A 744

b) x = 2.8", MIDPLANE

120 KA

20 V/cm

A 746

c) x = 3.8", MIDPLANE

120 KA

20 V/cm

A 747

d) x = 4.8", MIDPLANE

120 KA

20 V/cm

A 762
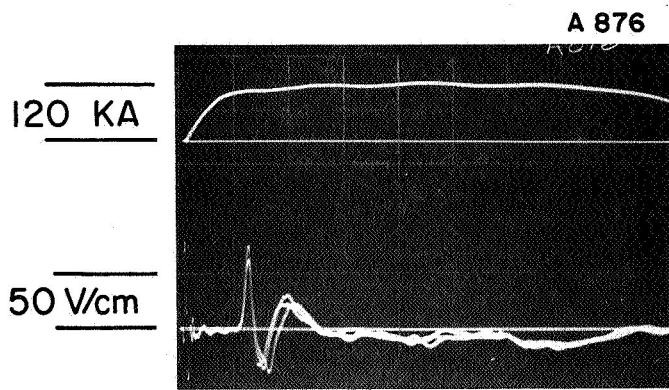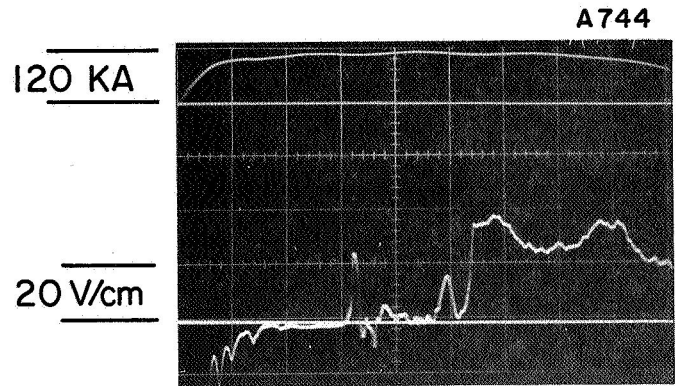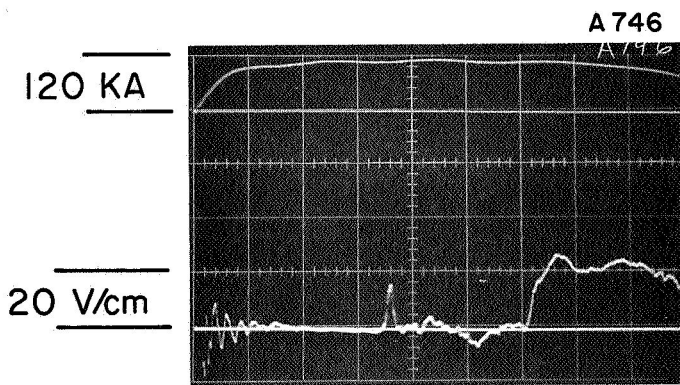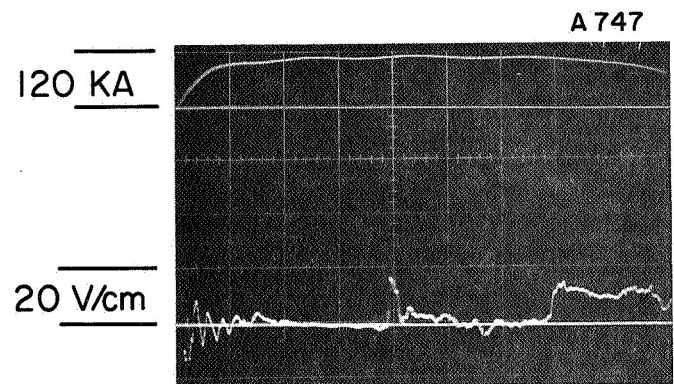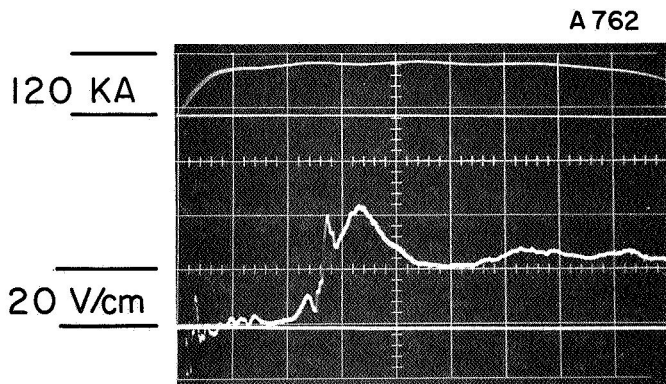
e) x = 0.75", 0.25" FROM ANODE

120 KA

20 V/cm

A 755
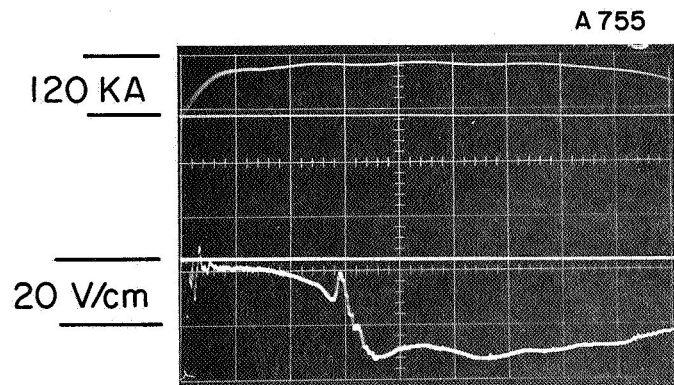
f) x = 0.75", 0.25" FROM CATHODE

ELECTRIC PROBE SIGNATURES OF CURRENT SHEET STABILIZATION
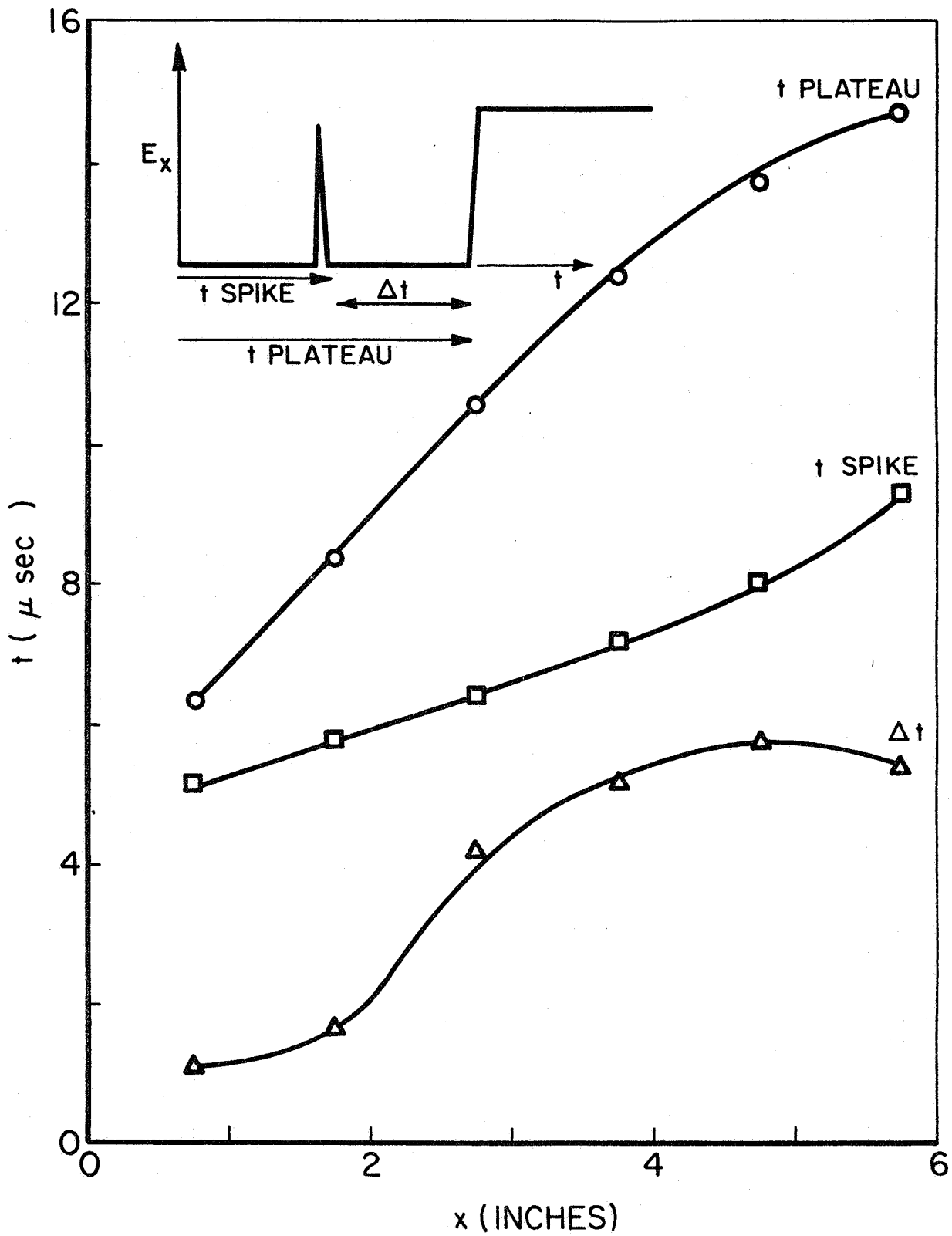
FIGURE 9

TRAJECTORIES OF CHARACTERISTIC FEATURES
OF ELECTRIC PROBE SIGNATURES

FIGURE 10

small to account for full acceleration of ions to sheet velocity (Refs. 41,42). Rather, it appears that the propagating sheet only partially accelerates the ambient gas, which later surges into, and is accelerated by, the quasi-steady current pattern. It is also possible that eroded insulator and electrode material provide some portion of the inlet mass flow to the acceleration zone, but their relative importance and duration cannot be judged in this experiment. As longer pulse lengths are applied to this device, it clearly becomes important to provide a source of inlet mass flow of well-defined flux and duration.

In passing, Figs. 9e,f display records of E_x obtained by a probe immersed in the conduction bands near the anode and cathode edge. Here the E_x field is essentially parallel to the current vector, hence is primarily a resistive component, nearly constant over the lifetime of the quasi-steady pattern, and opposite in sign near anode and cathode.

Summarizing to this point then, the diagnostic measurements on the parallel plate apparatus suggest the following picture of its operation: electrodynamically, the current sheet breaks down, propagates along the metal electrodes imparting some fraction of its velocity to the gas it passes through and, upon reaching the metal-to-insulation junction, decelerates quickly to a stabilized, hairpin-shaped current distribution. Gasdynamically, the flow set up by passage of the current sheet lags behind the sheet somewhat until it stabilizes, and then, following a transition period, this gas provides the inlet flow to the stabilized acceleration zone.

Experiments of the type described above, using uniform ambient fill of the channel to a prescribed pressure, compromise three important aspects of the problem under study. First, as already mentioned, no external supply of mass flow is provided to sustain the quasi-steady acceleration phase over longer pulse lengths; second, no downstream diagnostics

of the particle-collector or ion-analyzer class are possible because of the short mean free paths of accelerated particles emerging from the current zone; and third, the influence of major ambient density gradients, such as those encountered in space operation of a thruster, on the current stabilization process cannot be assessed. In an effort to remove these restrictions, the shock tube injection system described earlier (Fig. 2) was installed, with somewhat equivocal results.

Previous application of this type of gas injection procedure in connection with exhaust plume studies on a pinch-orifice device (Ref. 48), had successfully provided a steep axial density gradient from the discharge chamber out into the large Plexiglas vacuum vessel. Because of the uncertainties in transitional gas flow patterns in this density regime, however, it was not clear whether this steep gradient was determined more by the time scale of the gas injection wave pattern, or by the large ratio of volumes of the vacuum vessel to the discharge chamber. Application of this injection technique to the parallel plate accelerator now indicate, in retrospect, that the latter was the case. Referring to Fig. 2, the orifices in the lines feeding the chamber and switch are adjusted until the current sheet reaches the metal-to-insulation junction at the same time it would for a uniform 100 μ fill, and the dynamics of the current sheet are then examined by Kerr cell photography and magnetic probes. If a sharp density gradient exists along the channel, noticeable acceleration of the sheet should be observed. To the contrary, however, the sheet is found to behave almost identically with the 100 μ ambient case, implying an essentially uniform density pattern, i.e., that the entire channel fills almost hydrostatically with the injected gas.

We are thus forced to conclude that substantial ambient density gradients along a one-dimensional acceleration channel

cannot be achieved by this method. One may speculate whether other combinations of inlet port size and number, driving pressure or shock tube dimensions might remedy this situation, but it now appears that the difficulty is quite fundamental. Namely, we may expect that any major density variation in a one-dimensional flow must extend over at least a few mean free paths. Since we wish to construct a profile ranging from 100 μ down to a sufficiently low value that ejected particles may reach remote ion collectors without collision, it follows irrevocably that the dimensions of the full profile will exceed that of the channel. Only if one is willing to expand the flow into two or three dimensions at the accelerator exit can this density decrease be achieved more abruptly. We are thus forced to consider addition of a large expansion vessel to the channel if ion sampling diagnostics are to be applied to the accelerated flow stream. Since this may considerably complicate the steady current density pattern in this region, however, this procedure will be deferred pending development of alternative diagnostic techniques.

The most recent studies on this program have concerned the attainment of a suitable quasi-steady inlet gas flow for the stabilized current pattern to accelerate. Clearly, complete simulation of a steady acceleration process involves two aspects, phenomenologically coupled, but temporally distinct: 1) establishment of a steady discharge current distribution; and 2) establishment of a steady gas flow pattern through this current distribution. We have shown that the time scale to achieve the former in this experiment is of the order of ten microseconds. The time to establish a steady gas flow pattern probably is much longer. To a crude approximation, we may regard the propagating current sheet of the initial transient phase as having completely swept out the ambient gas over that portion of the channel it has passed on its way to the position of stabilization, in a period of only

a few microseconds. To "refill" this volume with gas from the exterior injection system should require a time of the order of the channel length involved divided by the sound speed of the injected gas, i.e., hundreds of microseconds for the present geometry.

Clearly this time can be reduced by shortening the channel length over which the propagating sheet runs before stabilization, and a series of studies are in progress to ascertain the minimum electrode length which still retains the essential features of the complete transition process. It should be noted in this respect, however, that regardless of this dimension, the downstream bowing of the stable current pattern also involves some evacuated volume of channel which must be filled with injected gas before the acceleration process can be regarded as truly steady.

It also seems advantageous to provide minimum restriction of the inlet flow to the channel, to hasten the filling process. Since the basic advantage of a shock tube injection system appears to be obviated in this particular experiment, other, more direct means of gas supply are under consideration. For example, attempts have been made to force the discharge to initiate some distance away from the rear wall of the channel, thus leaving an undisturbed ambient gas reservoir upstream of this position. With reference to Fig. 11a, 3/4" wide electrode strips were located 4-1/2" from the back wall, in the hope that breakdown would occur directly across the channel.

However, unlike the results found in the pinch devices (Ref. 2), the discharge was found not to initiate directly across the gap but to elect the minimum inductance path shown. This hairpin of current then sweeps forward to establish the usual stabilized configuration, again evacuating the intended gas reservoir as it sweeps through. In an effort to hinder this minimum inductance breakdown, a baffle was inserted in

A 1082

A 1083

INSULATOR

ELECTRODES

(+)   (−)

(+)   (−)

X

0 −0.75" −4" −5.3"
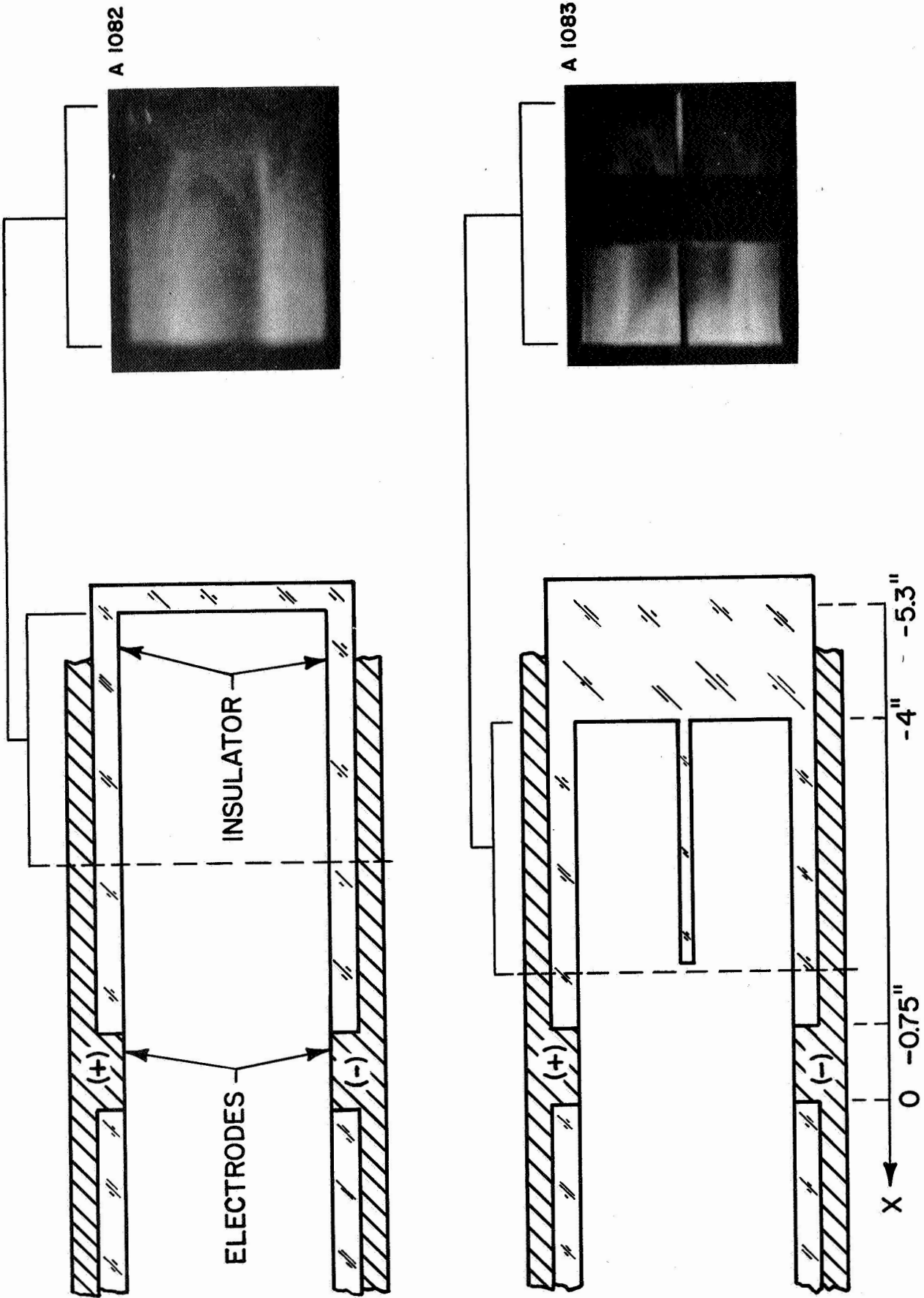
MINIMUM INDUCTANCE BREAKDOWN OF BAFFLED CHANNEL

FIGURE II

the midplane to increase the path length required for low inductance breakdown (Fig. 11b). Again the discharge chose the minimum inductance path in the form of two hairpins as shown. Addition of other baffles was not attempted, since the flow constriction of such an arrangement then becomes comparable with that of a multiported injection plate.

Also examined was the possibility that in the usual configuration the current sheet broke down not exactly at the back wall, but perhaps far enough removed from the wall that a small volume of relatively undisturbed gas was left next to the wall. A series of Kerr cell photographs and magnetic probe records indicated, however, that the sheet initiated right at the wall and essentially no sheet standoff distance existed at breakdown.

At present a variety of other gas supply possibilities are under study. Regardless of the final form chosen, it is clear that longer current pulses will be required to achieve complete quasi-steady operation of the accelerator from both the current distribution and gas flow pattern criteria. With the present capacitor bank available, this predicates lower current levels, and here the uniformity and accelerating effectiveness of the discharge pattern may be suspect. Thus, these factors are now being examined as the pulse length and amplitude are gradually lengthened and lowered, respectively. Should the essential features of the transition problem become indistinct before the desired testing times are achieved, it will be necessary to increase the capacity of the bank, to provide longer pulses at the higher current levels.

III. MPD ARC SIMULATION
(Clark)

The previous semi-annual report[48] described the
construction of a discharge chamber whose geometry closely
resembles the steady-state magnetoplasmadynamic arcjet. The
primary interest in this configuration, details of which are
shown in Fig. 12 is the simulation of steady MPD arc operating
characteristics on a quasi-steady basis, at power levels and
plume dimensions inaccessible to direct steady state experi-
ments. Such simulation will permit thorough exhaust plume
and discharge chamber diagnostics at current levels from
under 10,000 to over 100,000 amperes, and with back pressures
duplicating a space environment. From these it is hoped to
piece together the details of the gas acceleration process,
current conduction pattern, and electrode loss mechanisms
for the self-field MPD arcs.

A secondary, but equally important purpose of this
study is to acquire experience with the operation of pulsed
accelerators on progressively longer driving current pulses.
As has been argued previously, efficiency of pulsed operation
may well be improved by extending the pulse lengths substan-
tially, to the extent that the device becomes more an
"intermittent steady" accelerator--i.e., one in which steady
acceleration processes prevail over the bulk of the pulse--
rather than a conventional plasma gun. Thus, to the extent
feasible in thruster practice, by properly adjusting the
ratio of pulse length to dead time, one could combine the
benefits of high-power plasma acceleration processes, with
modest average power consumption.

In this report we confine our attention to the first
interest--MPD arc simulation--and almost exclusively to one
element of that problem. Clearly, two aspects of arc opera-
tion must be simulated if the analogy is to hold: 1) the
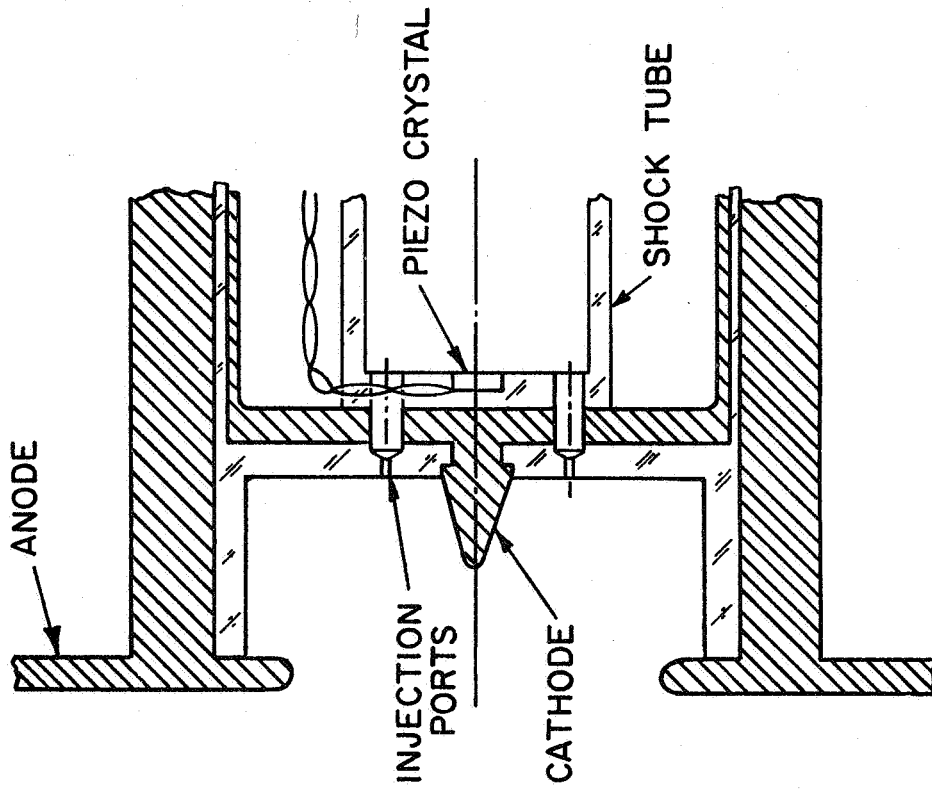
CROSS SECTION OF MPD ARC SIMULATOR

FIGURE 12

discharge current pattern, electrode voltage, and cathode emission processes must stabilize to quasi-steady situations similar to those of MPD arcs; and 2) the mass flow pattern through the electrode region must stabilize to a steady level in the interesting range of MPD operation. Only after both the electrical and gasdynamical requirements have been met can one claim full relevance of the detailed measurements. The previous report[48] dealt primarily with the effectiveness and time scale of the electrical simulation; here we mainly consider the gasdynamic problem.

Perhaps the most illustrative introduction to this problem is a comparison of the several time scales of the overall process. First, recall that there are three characteristic times associated with the output of the capacitor bank and the subsequent electrodynamic plume development (see Fig. 13):

τ_ℓ = duration of the flat top current pulse--controllable from 20 to several hundreds of microseconds in this experiment

τ_r = the rise time of the current to its steady value--typically a few microseconds.

τ_s = the time from current initiation until stabilization occurs. Typically $\tau_s \approx 0.4 \ \tau_\ell$ so that $\tau_r < \tau_s < \tau_\ell$.

In comparison to these, the following gasdynamic times are of interest:

τ_M = the interval over which the mass flow rate is constant

τ_R = the time required for the mass flow rate to reach its steady value

τ_A = the time required for a steady pressure to be reached in the arc chamber after the mass flow has become constant
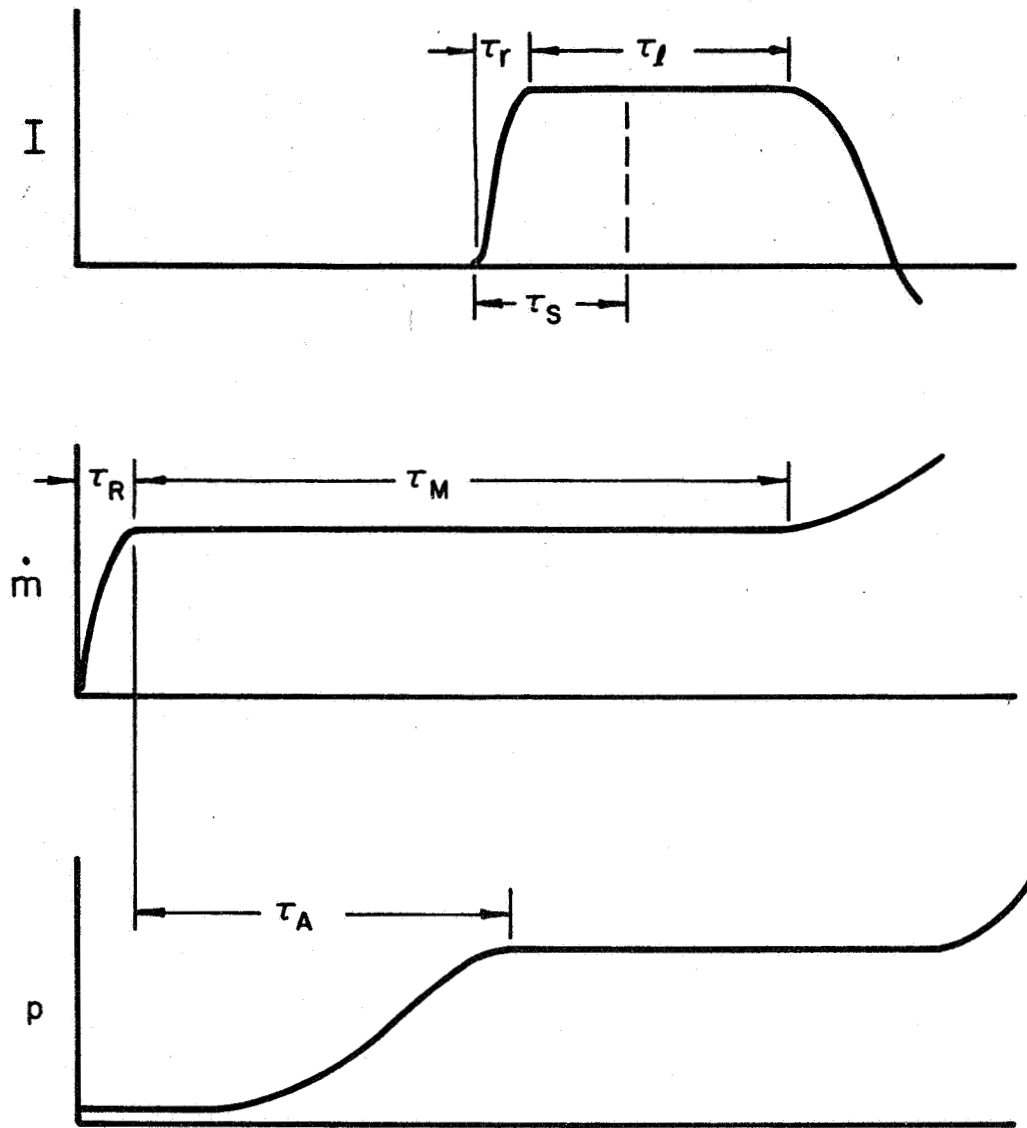
CHARACTERISTIC TIMES FOR CURRENT
PULSE AND MASS FLOW

FIGURE 13

In terms of these, the requirements of the gas injection system can then be summarized:

$$\tau_M > \tau_\ell$$ to ensure steady mass flow throughout the current pulse

$$\tau_R \ll \tau_M$$ so that during τ_R the pressure distribution in the vacuum tank does not increase enough to compromise the space environment requirement

$$\tau_A < \tau_M$$ to enable a steady pressure to prevail in the electrode region over the bulk of the current pulse

The first and third requirements can be combined to give

$$(\tau_M - \tau_A) > \tau_\ell$$

i.e., the current pulse should only occur after a steady arc chamber pressure has been reached and before the mass flow rate departs from its constant value.

The most effective means of satisfying the requirements for abrupt initiation of a rapidly stabilizing mass flow has proven to be via a shock tube injection system, incorporating the pressure reservoir behind the head-on reflection of a shock wave from the tube end wall to drive a group of injection ports of variable diameter. Because of this key role of the quasi-steady mass flow in the desired MPD simulation and in view of several related applications of this shock tube technique to other experiments in the laboratory, methods of analytical and experimental determination of the actual gas injection characteristics from this system will now be described.

Neutral density measurements with fast response ionization gauges showed that a previous shock tube gas injection system[48] provided a pressure profile in the electrode region which never attained a steady phase, but rose steadily at about 25 μ per 100 μsec in the pressure range of interest.

This rise was attributed to the low initial pressure in the shock tube driven section (0.01 µ) and the size of the gas reservoir (tube diameter = 7/8"). The present tube dimensions were selected (diameter = 2-3/8", driven section length = 7'-6", driver section length = 2') to give a constant pressure reservoir time of almost one millisecond. In addition, in order to decrease the shock thickness, i.e., to decrease τ_R, the initial pressure in the driven section was increased to 1 mm. The resulting leakage flow out the injection holes prior to shock tube firing did not increase the back pressure to more than about 1 µ due to the speed of the diffusion pump and the small size of the gas injection holes (diameter = 0.030").

In practice, the constant mass flow time, τ_M is terminated by the return to the end wall of the reflected shock after its interaction with the contact surface. This is best shown graphically on the x-t diagram of Fig. 14, which is based on ideal gas flow in a one-dimensional shock tube of the above dimensions with initial pressures of 1 mm and 35 psia in the driven and driver sections, respectively. The figure shows the conventional division of gasdynamic regions by number, and subsequent numerical subscripts refer to these regions. For the case shown, the ideal constant pressure time in the reservoir is roughly 1 millisecond. Also shown on the same figure is the result of a calculation taking account of the viscous interaction of the gas with the tube wall. On a shock tube wall, as with steady flow situations, the no slip condition leads to the formation of a viscous shear layer or boundary layer. In a shock centered reference frame, this boundary layer has a negative displacement thickness so that it acts like a mass sink to the incoming flow, generating rarefactions which propagate forward to attentuate the shock. If the shock tube is long enough, this attenuation proceeds until the rate of mass influx into the shock is balanced by the boundary layer mass flow moving past the

P_1= 1mm Hg ARGON
P_4= 35 psia ARGON
$T_1 = T_4 = 300\,°K$

HEAD OF REFLECTED
RAREFACTION

REAL GAS

IDEAL GAS

τ_M

τ_M

②

③

SHOCK

INITIAL
RAREFACTION

CONTACT
SURFACE

①

④

m sec

⑤ 3

——— IDEAL GAS
——— REAL GAS REF. A1
τ_M = CONSTANT PRESSURE
        TIME

1' 0 1' 2' 3' 4' 5' 6' 7'

DRIVER
SECTION

DRIVEN SECTION
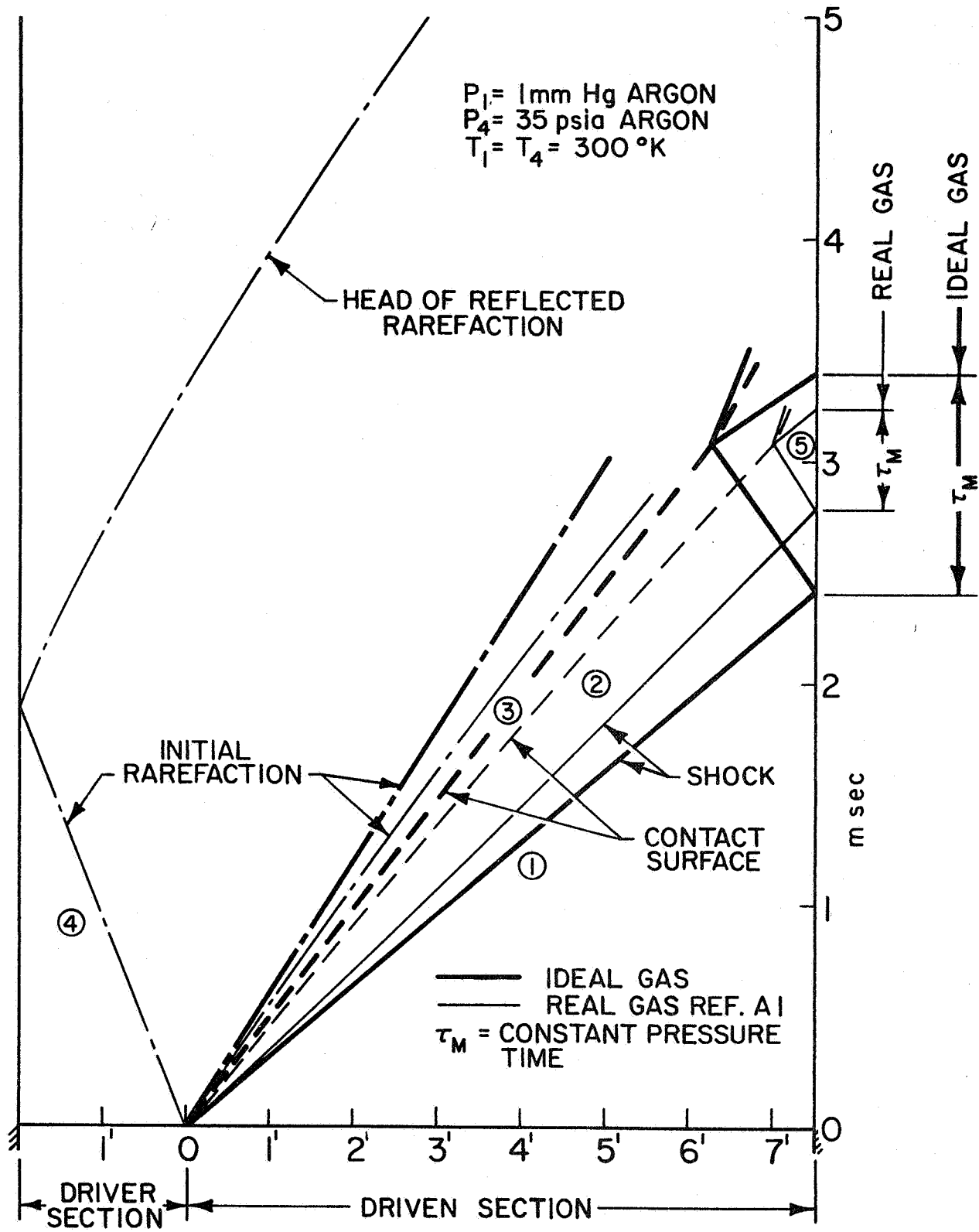
SHOCK TUBE X-T DIAGRAM

FIGURE 14

contact surface, after which time the separation distance
between the shock and contact surface remains constant. The
major effect then is that both the testing time and the re-
servoir pressure are decreased from their ideal values. For
lower initial pressures in the tube, the boundary layer
growth and consequent shock attentuation are increased, an
effect reflected in still lower values of reservoir pressure
and duration. Note that the reflection of the rarefaction
off of the driver end wall does not have a role in determining
the reservoir conditions, due to the large expansion ratio of
the initial rarefaction. Hence, only a very small driver
section is necessary to generate the reservoir conditions
shown.

Figures 15 and 16 show comparisons of ideal gas and
real gas calculations of the reservoir pressure and constant
pressure reservoir time, respectively, as the initial pressure
in the driven section is varied. The calculations were per-
formed with a driver pressure of 35 psia, the experimental
value used throughout all the tests to ensure the most repro-
ducible diaphragm rupture. The experimental points in
Figs. 15 and 16 were derived from an insulated piezoelectric
crystal mounted flush with the end wall of the shock tube.
This probe was similar in construction to other pressure
probes discussed in previous reports[47,48] with the excep-
tions that the diameter of the crystal has been increased
from 5/32" to 1/4" and its thickness increased from 0.010"
to 0.040" for better sensitivity at low pressures. Using
straightforward relations for the output of a piezo crystal,
the analytical calibration factor for the probe and associated
coaxial cable is found to be 2.0 volts/atm. Due to the
external circuitry, the crystal signal has an RC decay con-
stant of 600 μsec, a feature which has been incorporated
in the reduction of the data.

A typical triple overlay of crystal response is shown
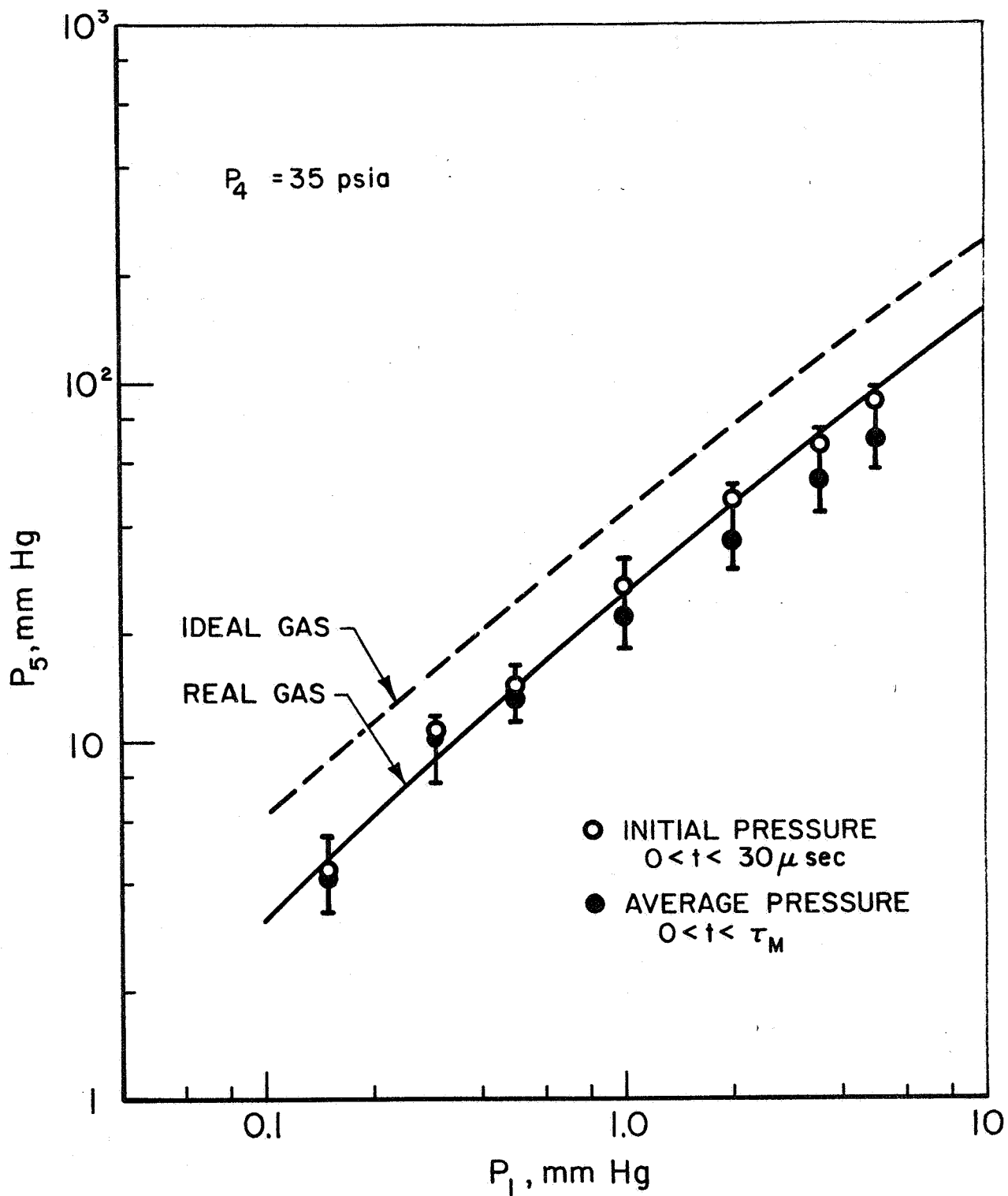
END WALL-PRESSURES IN SHOCK TUBE

FIGURE 15
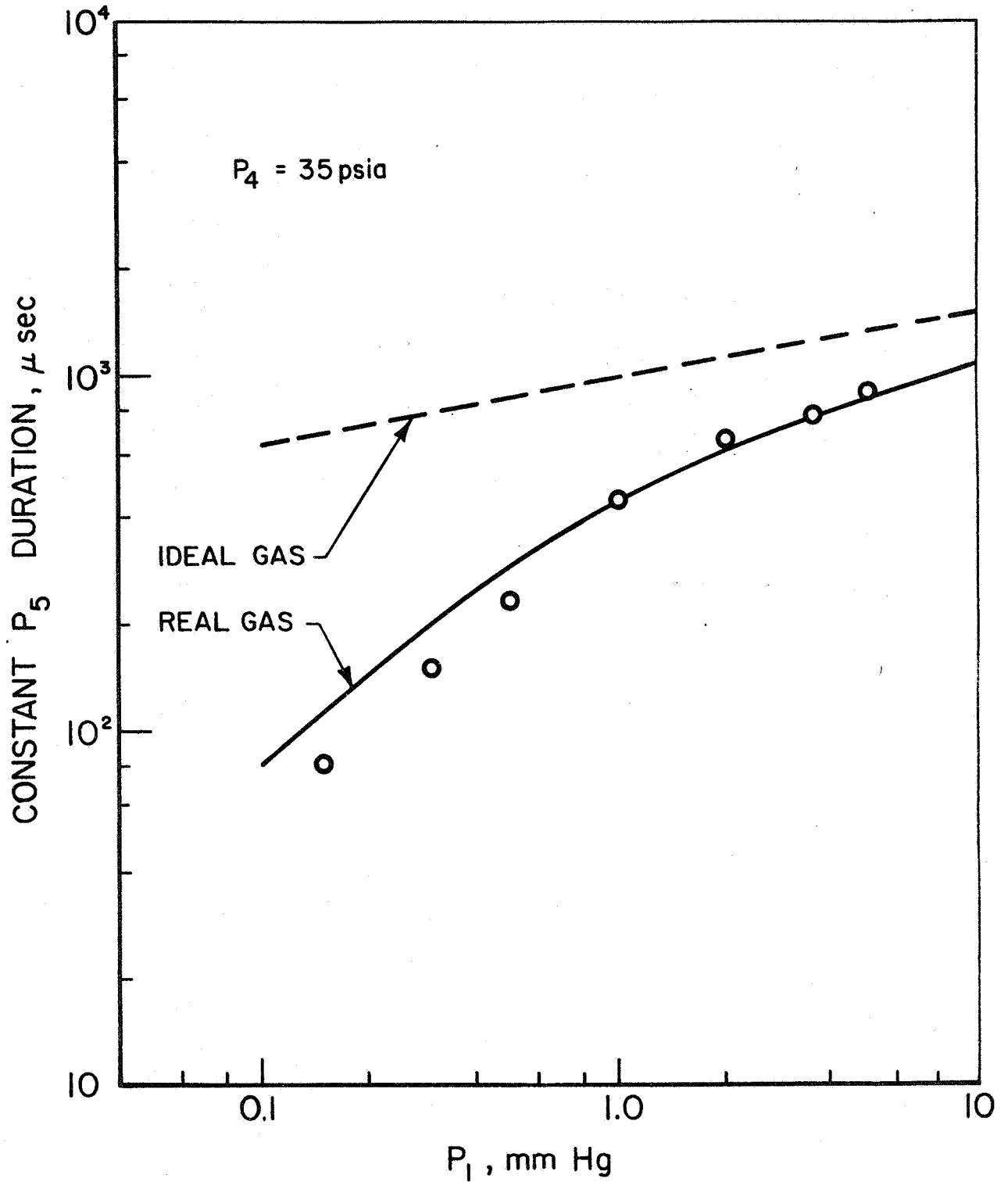
CONSTANT PRESSURE DURATION AT END OF
SHOCK TUBE

FIGURE 16

in Fig. 17. This picture shows a sharp initial signal rise
from the impinging shock, a nearly constant pressure for
approximately 500 µsec, and a subsequent pressure rise due
to the return of the reflected shock after interaction with
the contact surface. This latter feature is not a sharp rise
because the contact surface is actually a diffuse zone due to
the nonideal diaphragm rupture. On the basis of such data
taken on expanded time scales, this shock tube system is
found to act like a valve with an opening time (τ_R) of less
than 2 µsec which is the resolution time of the crystal cir-
cuit. It needs to be noted that only the initial portion of
the piezo response ($\leqslant$ 30 µsec) can be compared to the value
predicted by the modified one-dimensional calculations,
because after that time, a reduction in p_5 due to "drainage"
through the injection ports will be felt by the sensor. This
effect is noted in Fig. 15 by including open data points which
indicate the initial reservoir pressure; i.e., that value which
can be compared to the real gas calculations, and solid data
points which represent the average reservoir pressure over the
time shown in Fig. 16. The error bars in Fig. 15 indicate the
total error due to the irreproducibility of the gasdynamic
process and the assignment of a particular pressure for the
indicated duration. The good agreement between the real gas
calculations and the experimental values lends confidence to
the mass flow values subsequently derived from these data.

Determination of the mass flow rates from the shocked
gas reservoir requires values of discharge coefficient for the
injection holes. At the prevailing low Reynolds numbers, an
assumption of unity for the discharge coefficient is not
warranted. However, by setting an initial pressure in the
shock tube and monitoring the pressure rise in the vacuum
tank with the vacuum pumps shut off, the desired discharge
coefficients can be determined empirically. These values are
shown as circled data points in Fig. 18 plotted against the
Reynolds number based on hole radius and upstream stagnation

211

P_5

$100 \mu \sec / DIV$
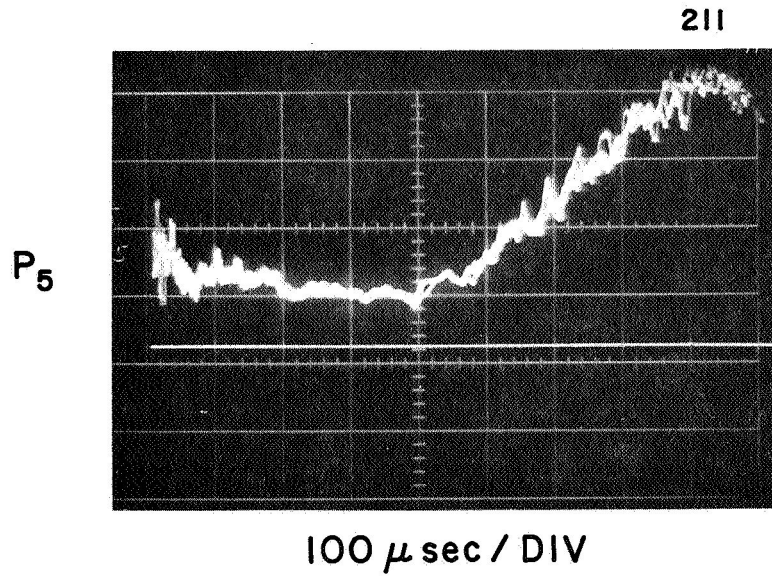
PIEZOELECTRIC PRESSURE RECORD
AT END OF SHOCK TUBE

FIGURE 17

EXPERIMENTAL DATA – REF. A2

O = EXPERIMENTAL DATA – SHOCK TUBE INJECTION

REYNOLDS NUMBER , $\frac{\dot{m}}{\pi r \eta}$

DISCHARGE COEFFICIENT
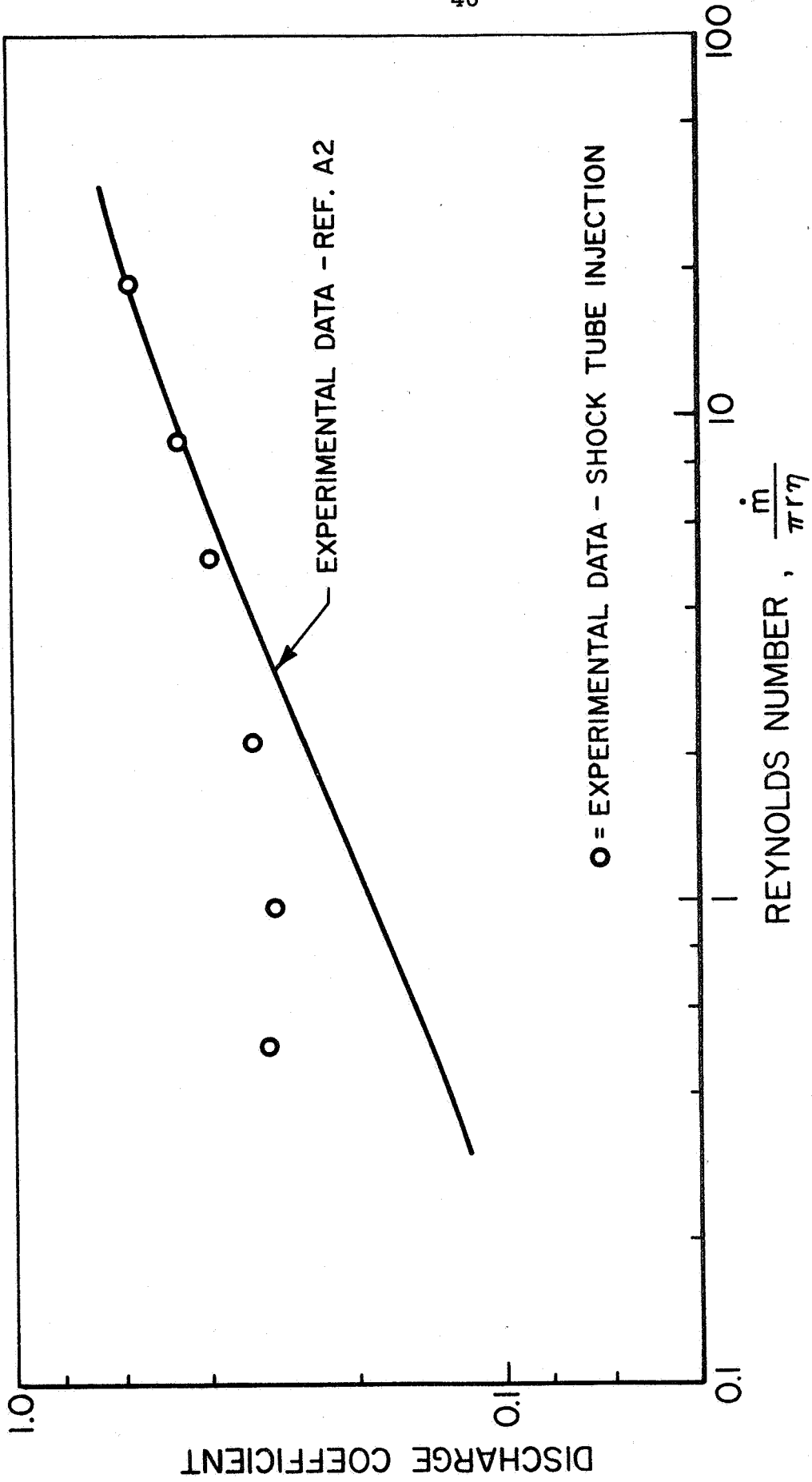
DISCHARGE COEFFICIENT VARIATION WITH REYNOLDS NUMBER

FIGURE 18

viscosity. In addition, the line shown in Fig. 18 represents experimental data for sharp edge orifices discussed in Ref. A-2. The apparent discrepancy at low Reynolds numbers is probably attributable to the different constriction geometries in the two experiments.

From the empirically determined discharge coefficients, the measured time-average reservoir pressures, and corresponding stagnation temperatures (calculated from isentropic expansion of initial p_5 to the time-average value), mass flow rates were calculated. These mass flow rates, steady to the accuracy shown for the duration given in Fig. 16, are shown in Fig. 19 along with the leakage flow rate resulting from maintaining the shock tube driven section at the given p_1 value.

Achievement of steady mass flow through the injection holes into the electrode gap does not necessarily imply steady flow over the entire discharge region. In particular, the desired operating conditions of the capacitor bank self-triggering into a time-steady pressure profile in the electrode region with a sharp gradient in pressure downstream from the orifice, is by no means guaranteed. To investigate the patterns of local pressure development, the fast ionization gauge discussed in the previous report[48] has been inserted in the arc chamber and exhaust regions, both with the leakage flow and the shock driven flow. Although the results are so far incomplete, some preliminary conclusions can be drawn. During the leakage mass flow period, little or no axial pressure gradients are measured for initial pressures in the shock tube of 1 mm or less, and no radial gradients are measured.

Figure 20 shows the gauge response to the dynamic situation, i.e., the injected mass driven by the shock generated reservoir, at the center of the anode plane with an initial shock tube pressure of 1 mm. The upper trace shows the familiar piezo crystal response and is used as a time reference, while the lower trace displays the ion current
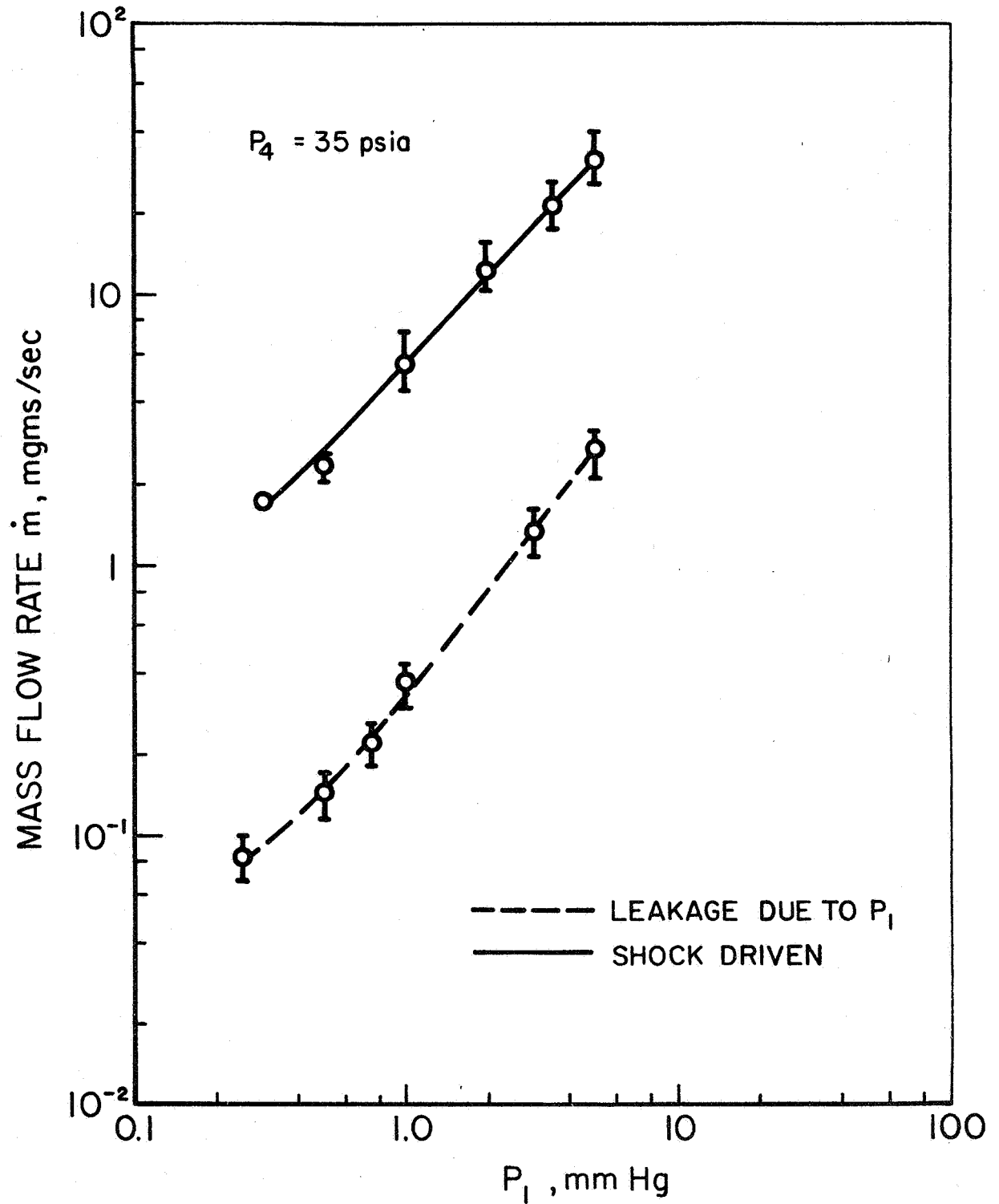
MASS FLOW RATES FOR VARIOUS
INITIAL PRESSURES

FIGURE 19

185

P₅

Iₚ

50 μ sec / DIV
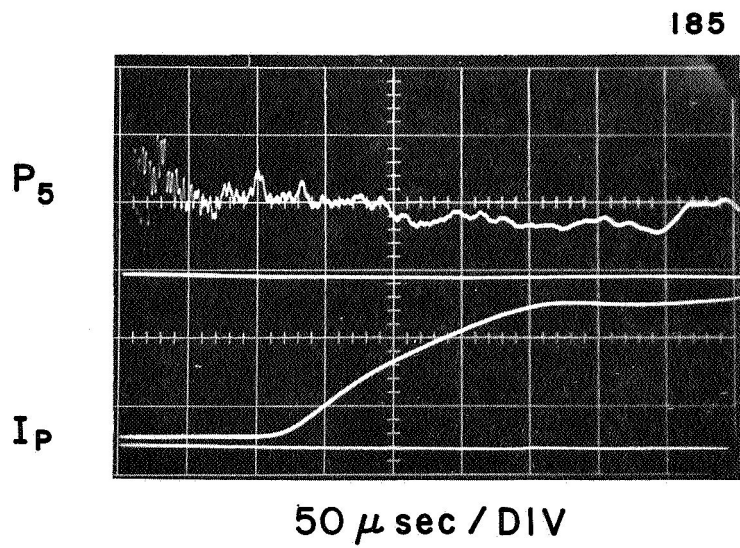
IONIZATION GAUGE RESPONSE AT
CENTER OF ANODE ORIFICE

FIGURE 20

which is directly related to neutral density. Several
interesting characteristic times can be seen in this photo:

    1.   The delay time between shock impinge-
ment on the end wall of the tube and initial
pressure rise at the center of the anode plane
is $\approx$ 100 μsec. During this time, the pressure
measured is that due to the leakage flow only.

    2.   The characteristic time required for
the chamber pressure to stabilize due to a fixed
mass flow rate (τ_A) is about 300 μsec. Referring
to Fig. 16 then indicates that initial pressures
in the shock tube must be greater than $\sim$ 300 μ
in order to achieve a steady pressure in the
electrode region.

    3.   Other data shots show that the pressure
then remains constant in this region until the
subsequent pressure rise in the shock tube can be
communicated, which requires roughly 100 μsec.
Thus, for these conditions, there is a constant
pressure distribution in the electrode region
for about 250 μsec duration.

Figure 21 shows the preliminary pressure profile
development on the centerline of the exhaust for these same
conditions; i.e., it is a cross plot of the average of
several oscillograms like that shown in Fig. 20. It is
seen that for the time period from 300 to 500 μsec after
the piezo crystal response, the pressure in the electrode
region (z = 0 on this figure) is essentially the same,
although the extremities of the profile continue to propa-
gate into the exhaust vessel. Pressures in the electrode
region can be changed by changing p_1 and/or the injection
hole size. The specific conditions used were maintained
throughout this series of pressure measurements and the
later studies of the actual discharge operation in order to

DEVELOPMENT OF PRESSURE
PROFILE ALONG ℄ OF
EXHAUST REGION

P_i = 1 mmHg

P_4 = 35 psia

t_0 = TIME OF FIRST PIEZO
CRYSTAL RESPONSE

INJECTION HOLE DIA.
= 0.030"

$t_0 + 700$

$t_0 + 600$

$t_0 + 500$

$t_0 + 400$

$t_0 + 300$

$t_0 + 200$

$t = t_0, t_0 + 100 \, \mu$ sec

FIGURE 21
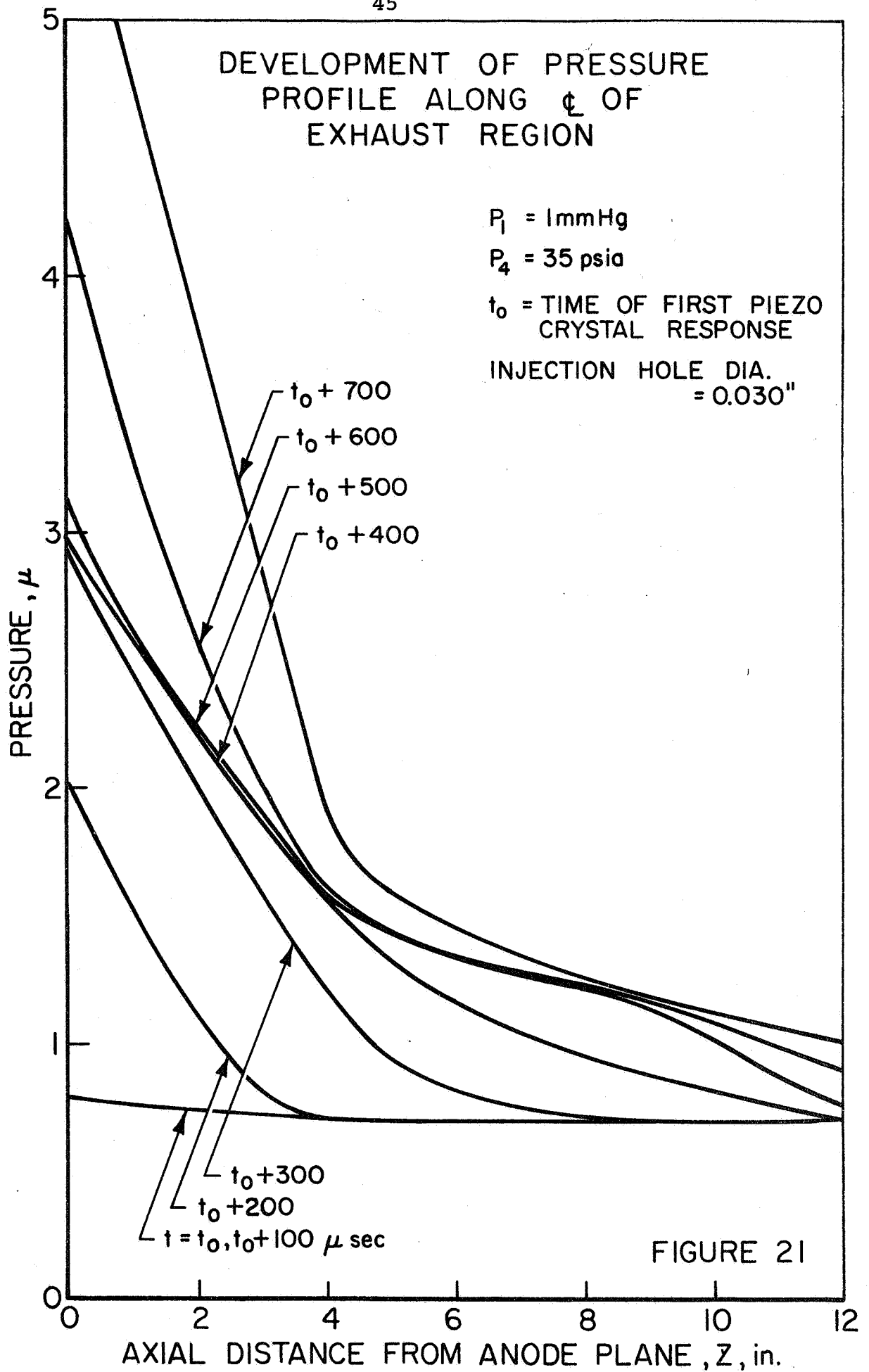
determine the gross operating characteristics of this geometry.

In a first application of the apparatus and technique outlined above, a preliminary survey of the current density distribution in the chamber and exhaust regions during a 140,000 amp x 20 μsec discharge has been made using a magnetic probe rake described previously.[43] For this operation, an initial pressure in the shock tube of 1 mm Hg was used for the reasons cited above. Referring to the Paschen curve for this configuration (Fig. 22) and the local pressure development with time in the electrode region (Fig. 21), it is clear that the spontaneous breakdown of the capacitor bank occurs considerably later than the steady pressure phase in the chamber. However, the mass flow rate change during the 20 μsec pulse duration was slight, and has been ignored for this first survey. Specifically, the piezo crystal output indicates a mass flow rate of about 50 mgm/sec and a local pressure in the electrode chamber of about 25 μ at the time of breakdown.

The primary results from this survey may be summarized as follows:

1. The current pattern clearly stabilizes in the chamber and in the region up to two orifice diameters downstream after approximately 6 μsec. In the outer exhaust region, the current contours slow but do not stop completely on this time scale.

2. The initial breakdown closely follows the insulator surfaces in the back of the chamber, attaching at the lip of the anode orifice and at the rear of the cathode. This is followed by a propagation to the cathode tip of only about 1/3 of the total current, the remaining 2/3
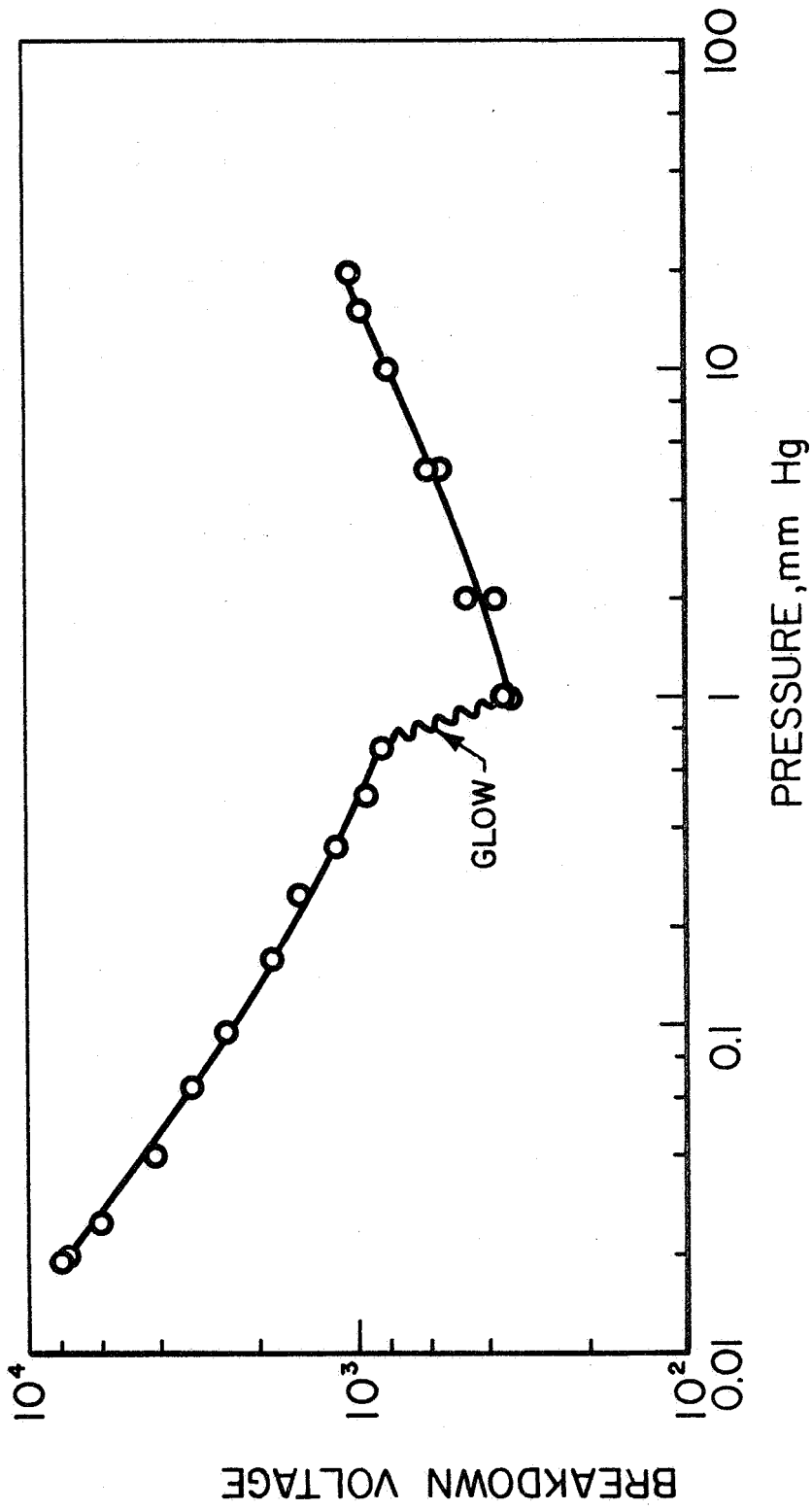
PASCHEN CURVE FOR MPD SIMULATOR IN ARGON

FIGURE 22

choosing to distribute itself nearly uniformly over the cathode and throughout the arc chamber for the duration of the pulse. A typical map of enclosed current contours which displays this distribution in the stabilized configuration is shown in Fig. 23. Note that the portion of current emanating from the cathode tip is essentially the same as that which projects out into the exhaust plume.

3. In the interval from 1 to 4 μsec after breakdown, the anode attachment of that current which enters the cathode tip is observed to spread rapidly over the entire downstream surface of the anode, i.e., out to the vacuum vessel wall 17 inches from the centerline.

In the early portion of this study, a conical aluminum cathode was used, but this was found to erode seriously, to the point of severe deformation after only a few shots (see Fig. 24). This was then replaced by a similar molybdenum cathode, which although clearly pitted by the discharge, did not seriously change its shape. Despite the complications of cathode erosion on operation of the accelerator, it offers unimpeachable evidence that the cathode surface is readily capable of thermionic emission on the time scale of this transient experiment, and thereby simulates MPD operation in this regard.

At present, surveys of this type are being extended into lower current-longer pulse domains where both the current distribution and the gas flow pattern will achieve a quasi-steady level, and the typical MPD operating range will be better simulated. Also, in addition to the MPD simulation, the implication of the results to pulsed thruster operation in quasi-steady modes is under more serious consideration.

I = 140,000 AMPS

t = 12 μsec

10 × 10³ AMPS

20

40

40

120 100 80 60

GAS INJECTION PORT
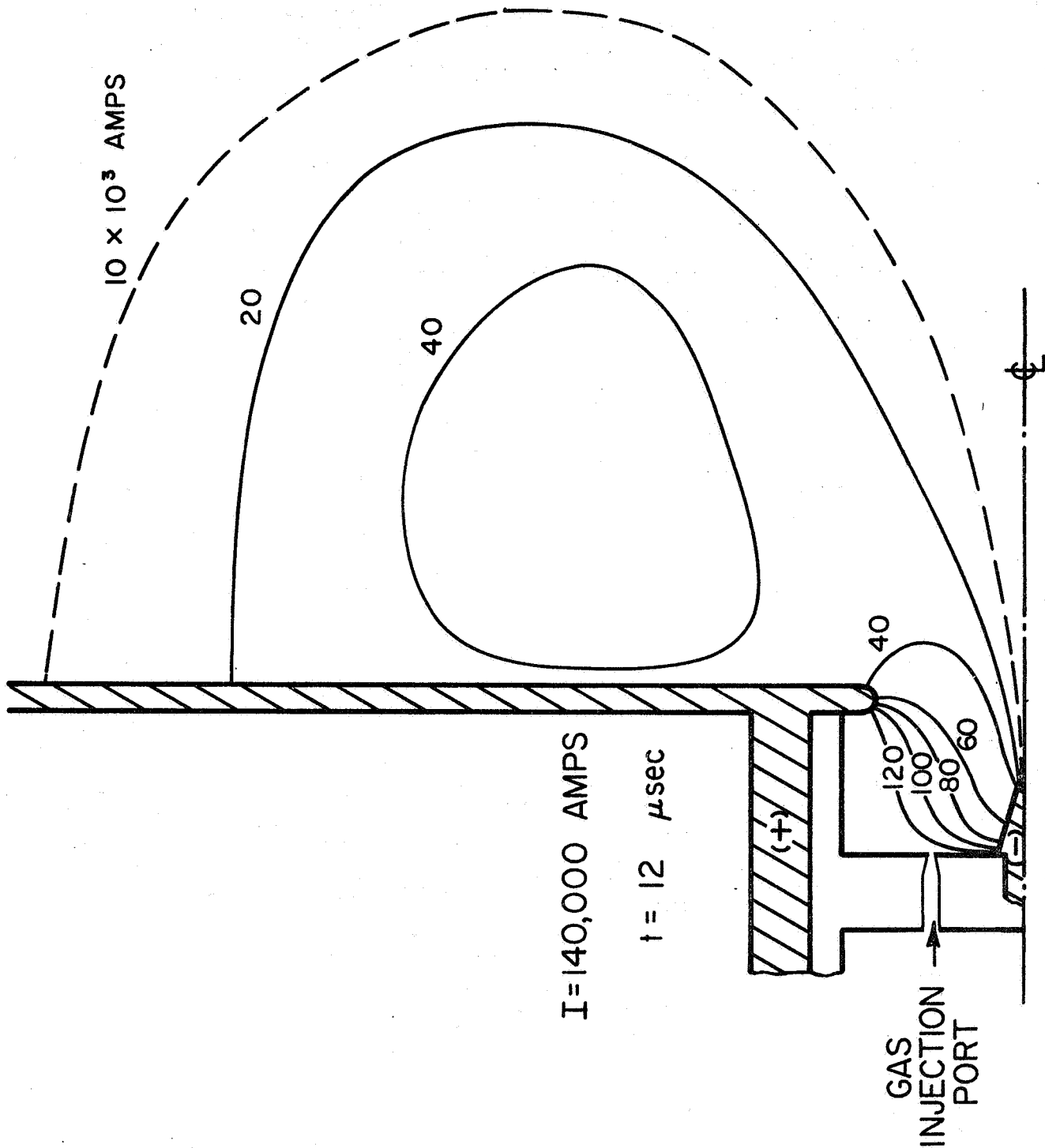
MAP OF ENCLOSED CURRENT CONTOURS FOR MPD SIMULATOR

FIGURE 23
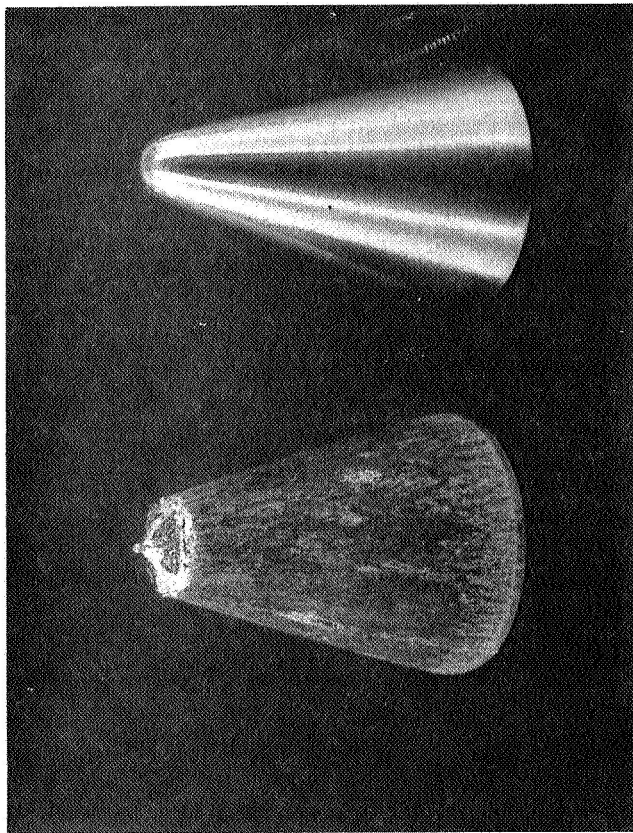
NEW AND USED (50 DISCHARGES) ALUMINUM
CATHODES

FIGURE 24

IV.   OPTIMUM ENERGY TRANSFER FROM LOW IMPEDANCE
PULSE NETWORKS TO ACCELERATING PLASMAS
(Wilbur)

This effort is intended to give a better under-
standing of the conditions under which a high energy power
supply, such as a capacitor bank or transmission line, will
transfer its energy to an accelerating plasma with optimum
efficiency. The work consists of four related studies:
1) design and development of low inductance capacitors suit-
able for simple assembly into pulse line configurations;
2) experimental determination of the detailed capacitor
characteristics; 3) experimental investigation of the con-
ditions for optimum transfer of energy; and 4) development
of analytical techniques to support the experimental studies.

The first phase of the capacitor design and develop-
ment program has been completed with delivery of the last of
12 capacitor units from the manufacturer (Corson Electric
Manufacturing Corp.). All of these units have been tested
and shown to behave like sections of low impedance trans-
mission line; i.e., they deliver a rectangular current wave-
form to a suitably matched load. A variable resistor capable
of withstanding the currents and voltages produced by these
units has been developed to permit determination of the
inductance and capacitance of the units under high voltage,
high frequency conditions. For example, if pulse lines com-
posed of a series of four units are discharged through the
calibration resistor adjusted to yield the matched conditions
for various initial voltages, the ratio of voltage across the
resistor to current through it measured over the flattopped
region of the current and voltage traces falls into the
range of 30 to 34 milliohms. The actual variation is shown
in Fig. 25 as the curve labeled "high current measurements."
If the values of the matching resistances are later measured
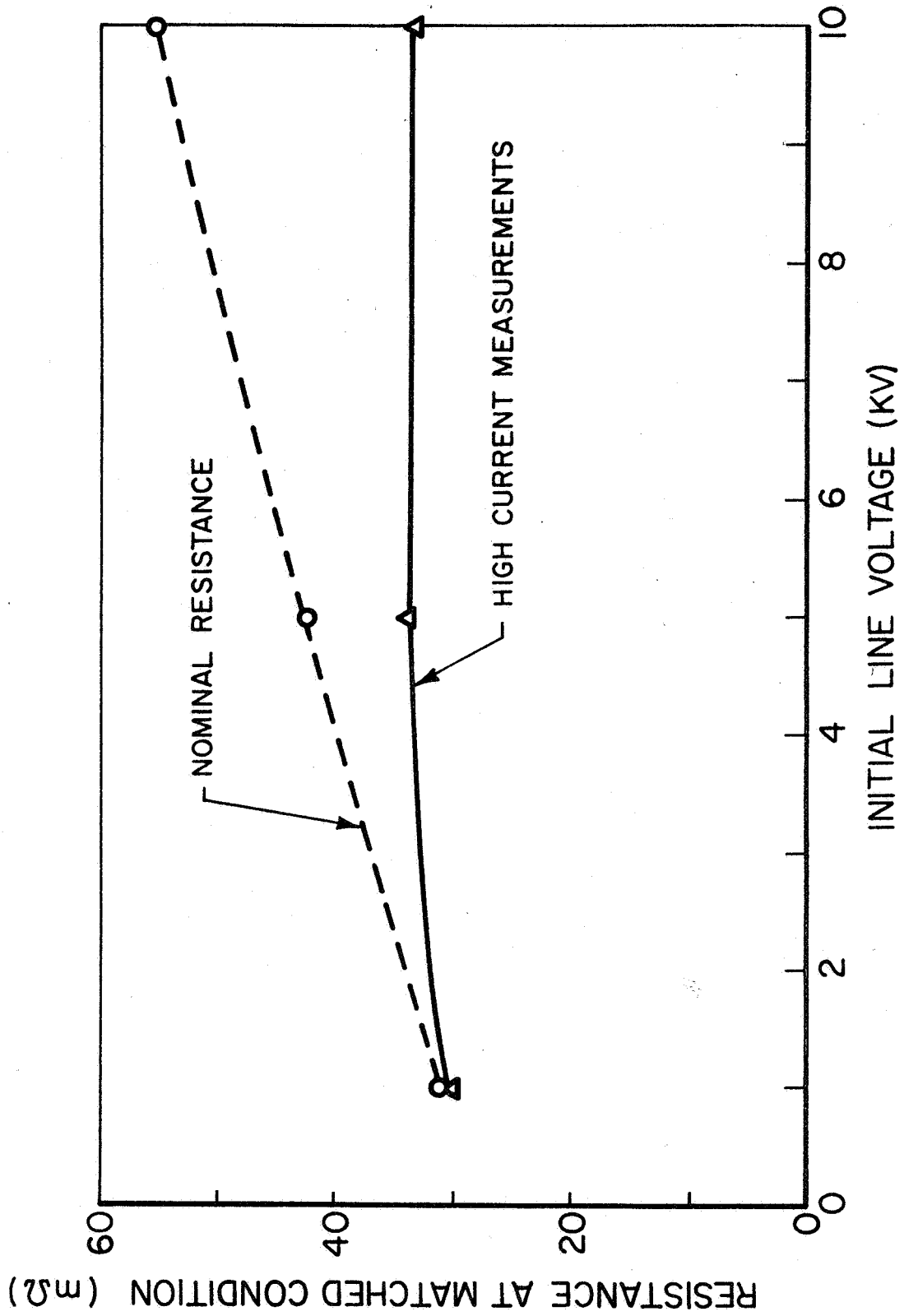
FIGURE 25

VARIATION OF MATCHING RESISTANCE WITH INITIAL LINE VOLTAGE

directly by a Kelvin bridge, a different curve, labeled "nominal resistance" is obtained. The discrepancy between these two curves simply reflects the change in the resistance of the load resistor as a function of current. Although additional tests at intermediate initial voltages are required to confirm these preliminary results, it appears the characteristic impedance at the conditions which exist during typical pulse line operation is near 33 milliohms. Using this 33 milliohm impedance and the observed single unit two-way transmission time of 0.45 microsecond, one obtains a capacitance of about 6.5 microfarads and an inductance of about 7.0 nanohenries for the average unit.

In previous work it has been commonly assumed that substitution of an accelerating current sheet for the resistive load usually employed in transmission line analysis would cause no essential difference in the behavior of the line-load system. In particular, this assumption implied that 1) optimum energy transfer from a transmission line to the current sheet would occur when the impedance of the line was equal to that of the current sheet, 2) no negative current would be observed when the dynamic impedance of the current sheet was equal to or greater than that of the line, and 3) the current would decay to zero over several two-way transmission times of the line when the current sheet impedance was greater than that of the line. The first evidence that this assumption might be invalid was given in the previous semi-annual report[48] in the form of oscillograms showing negative currents under conditions where the average pinch impedance was calculated to be greater than that of the driving line. Subsequently, the capacitor units have been connected in a three-line configuration having a characteristic impedance of 11 milliohms, and nominal pulse length of 2 μsec, to the parallel plate accelerator described in Section II, which as a nominal impedance of about 20 milliohms (compared to 10 milliohms for

the pinch machine). Magnetic field probe records confirm a current sheet velocity corresponding to a 20 milliohm load impedance and yet a sizable negative current is still observed on the second half cycle as shown in Fig. 26a. Note also on this oscillogram the tendency of the current pulse to be elongated and to decay slowly; indeed, the "2 μsec pulse line" has here produced a pulse that remains positive for about 6 μsec. To provide insight into this current pulse behavior, the computer program combining snowplow plasma dynamics with the transmission line wave equation (described in detail in Ref. 48) was modified to reflect parallel plate accelerator geometry and the current and voltage waveforms were computed. The results, shown in Fig. 26b, closely confirm the experimental observation. Further examination of the analytical calculations now suggest that it is the relatively large inductance associated with the current sheet configuration that causes the current reversal in those cases of load impedance equal to or greater than that of the line. This inductance, which would not appear in a simple resistive load, here adds sufficient inertia to the circuit that the current lags behind the transmission line voltage decay and, thereby the transmission line achieves a negative voltage before the zero current condition is reached. This negative voltage then produces the negative current observed on the second half cycle. Expressed another way, in the "near-match" regime, the requisite inductance growth rates will quickly generate inductance levels capable of seriously distorting the voltage waveform whenever current magnitude is attempting to change. This effect is observed over the entire interesting range of line and load impedance, and seems to impose a basic loss mechanism which may reduce the efficiency of energy transfer to the current sheet motion.

Another output of the computer study is the energy balance plot shown in Fig. 27. This shows the energy distribution in the parallel plate accelerator filled with 100 μ

A 708

240 KA —

I

V

5 KV/DIV

a)

300

200

I
(KA)

100

0

- 5

0

V
(KV)

5

10

b)

t, I μsec /DIV
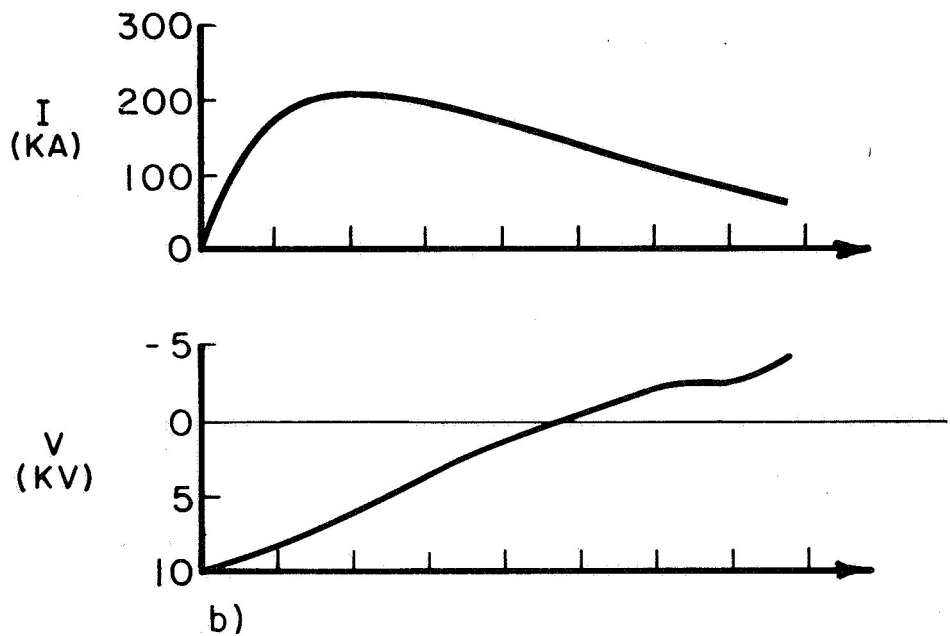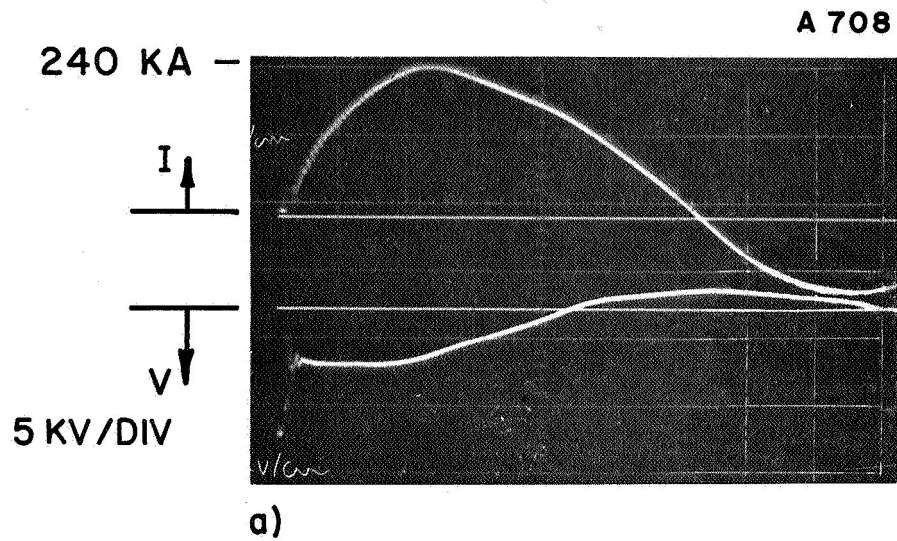
100 μ ARGON

OBSERVED AND COMPUTED CURRENT
AND VOLTAGE SIGNATURES

FIGURE 26

DRIVEN BY 3 LINES OF 4 UNITS EACH
0.008 OHM × 1.3 μ sec ; 100 μ ARGON

TRANSMISSION LINE ENERGY

ACCELERATOR FIELD ENERGY

THERMAL ENERGY IN GAS

ENERGY IN DIRECTED MOTION

SWITCH FIELD ENERGY

ENERGY RATIO

1.2
1.0
.8
.6
.4
.2
0

TIME (μ sec)

0   1.0   2.0   3.0   4.0   5.0   6.0   7.0   8.0
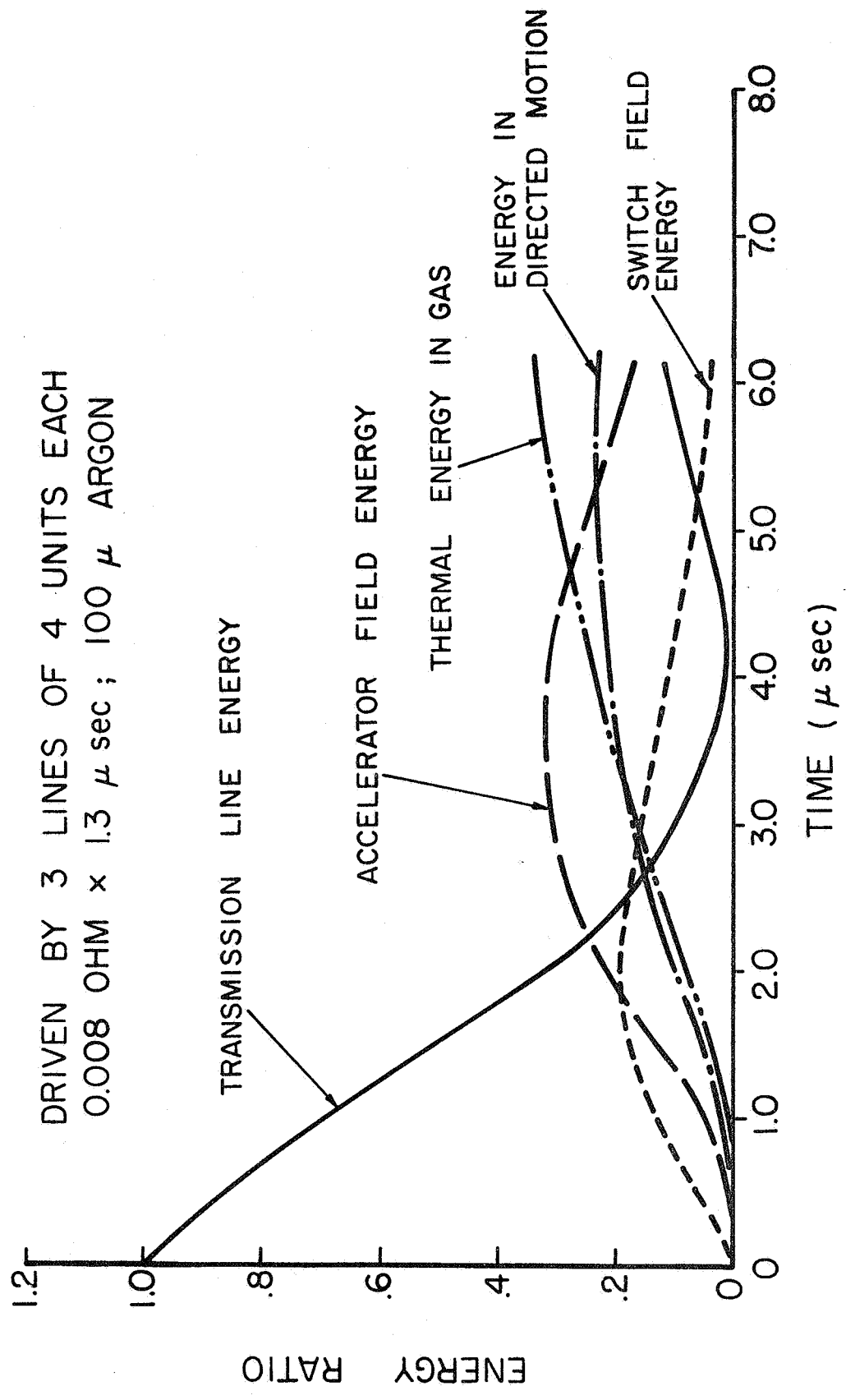
PARTITION OF ENERGY IN PARALLEL PLATE ACCELERATOR

FIGURE 27

argon and in a 0.011 ohm x 1.8 μsec transmission line driving it (3 lines of 4 capacitors each) as a function of time. Energy contained initially in the transmission line is transferred into the magnetic fields and into the current sheet in the form of thermal and directed motion of the snowplowed gas as the acceleration process proceeds. The current sheet inductance effect described above can be seen in this plot as the transfer of energy from the magnetic fields back into the transmission line after about 4 microseconds.

A computer analysis is also being carried out for the pinch discharge geometry. As shown in Fig. 28 the essential elements of the energy balance are the same as they were for the parallel plate accelerator with one essential difference. Namely, the time available for transferring energy into the accelerating current sheet is now limited by the pinch time, and the pulse length for optimum energy transfer to the sheet is therefore closely coupled to the pinch time. Figure 28a is based on five lines of two capacitors each (0.007 ohm x 0.9 μsec) driving the 8-inch pinch with 100 μ argon through a one nanonhenry switch. Figure 28b shows how this energy distribution plot is modified when the same pinch is driven by six lines of two units (0.005 ohm x 0.9 μsec). Note that although the impedance mismatch is greater when six lines are driving the pinch as evidenced by the relative minimum energies in the transmission line (occurring at about 1 microsecond), the energy transfer to the gas at pinch time is greater with six lines because in this case there is less transfer of energy back into the line from the magnetic fields. It can be seen, therefore, that both pulse line length and impedance are important in determining the point of optimum energy transfer to the current sheet, and it appears that this optimum will not necessarily occur when the average impedance of the pinch is exactly equal to the line impedance.

Another computer study is currently being conducted

a) 5 LINES OF 2 UNITS EA.

TRANSMISSION LINE ENERGY

PINCH FIELD ENERGY

DIRECTED MOTION OF GAS

THERMAL ENERGY IN GAS

SWITCH FIELD ENERGY

ENERGY RATIO

1.2 1.0 .8 .6 .4 .2 0

TIME (μ sec)

0 1.0 2.0

b) 6 LINES OF 2 UNITS EA.

TRANSMISSION LINE ENERGY

PINCH FIELD ENERGY

DIRECTED MOTION OF GAS

THERMAL ENERGY IN GAS

SWITCH FIELD ENERGY

ENERGY RATIO

1.2 1.0 .8 .6 .4 .2 0

TIME (μ sec)

0 1.0 2.0

58
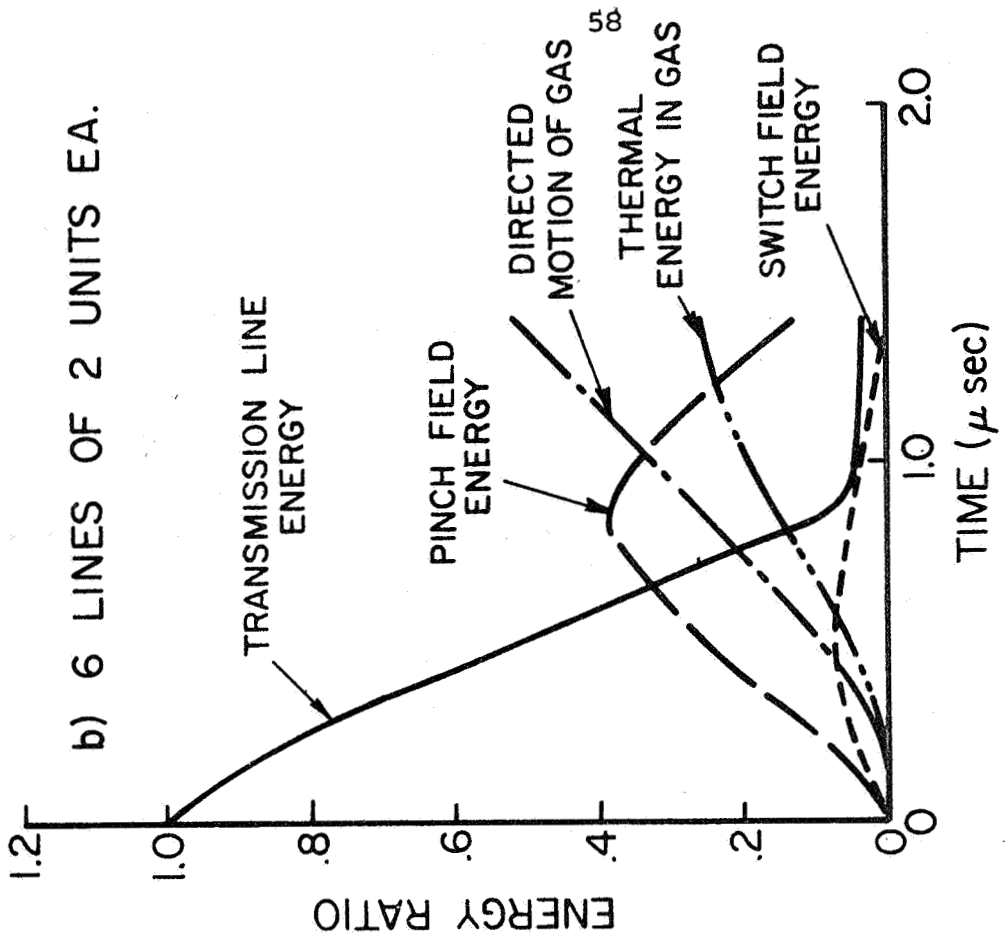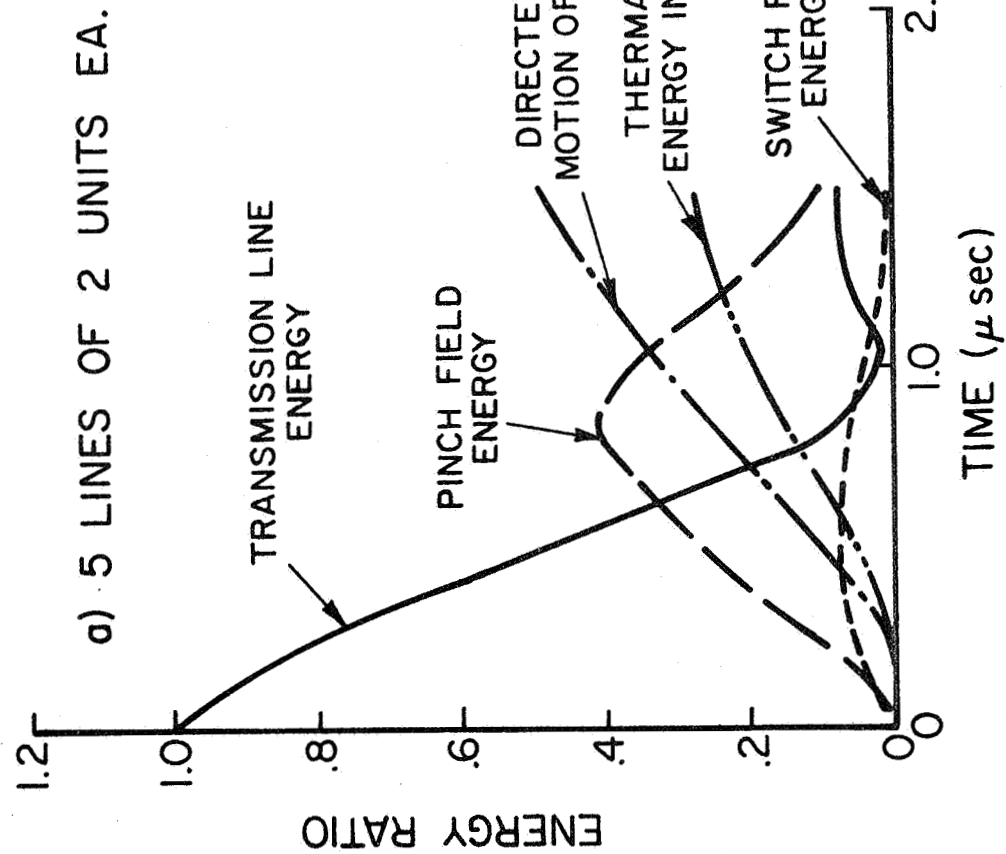
PARTITION OF ENERGY IN 8" DIA. PINCH DISCHARGE

FIGURE 28

to determine under what line configurations the maximum fraction of the initial line energy is transferred into directed motion of the gas. Figure 29 shows this optimization for the case of 100 μ argon in the 8-inch pinch chamber, with an assumed switch inductance of 1 nanohenry. It is hoped that a broad survey of this type will identify the conditions under which the optimum energy transfer can be most easily investigated experimentally.

Reference 48 reported our concern that the switch inductance might be sufficiently large to restrain the rising current throughout the entire nominal pulse time for the short pulse configurations. In order to insure this would not be the case, considerable effort has been spent on development of a new low inductance switch. The concept of the switch is illustrated in Fig. 30. Unfortunately, this geometric configuration exhibits a tendency to spoke and the low inductance calculated for the device is not realized for most arrangements of the capacitors. It does seem to work adequately for the case of six lines of two units and can be used under these conditions if such runs are needed in the future.

Other investigations conducted during the report period include a study of the effects of pinch chamber height, type of gas used in the chamber, and gas pressure on the efficiency of energy transfer. Additional effort will be required to complete this investigation in light of the inductance effect outlined in the beginning of the report. In particular, current sheet velocity and continuity must be investigated in each case, since the amount of negative current observed on the second half cycle is now known to be an adequate indication of efficiency.
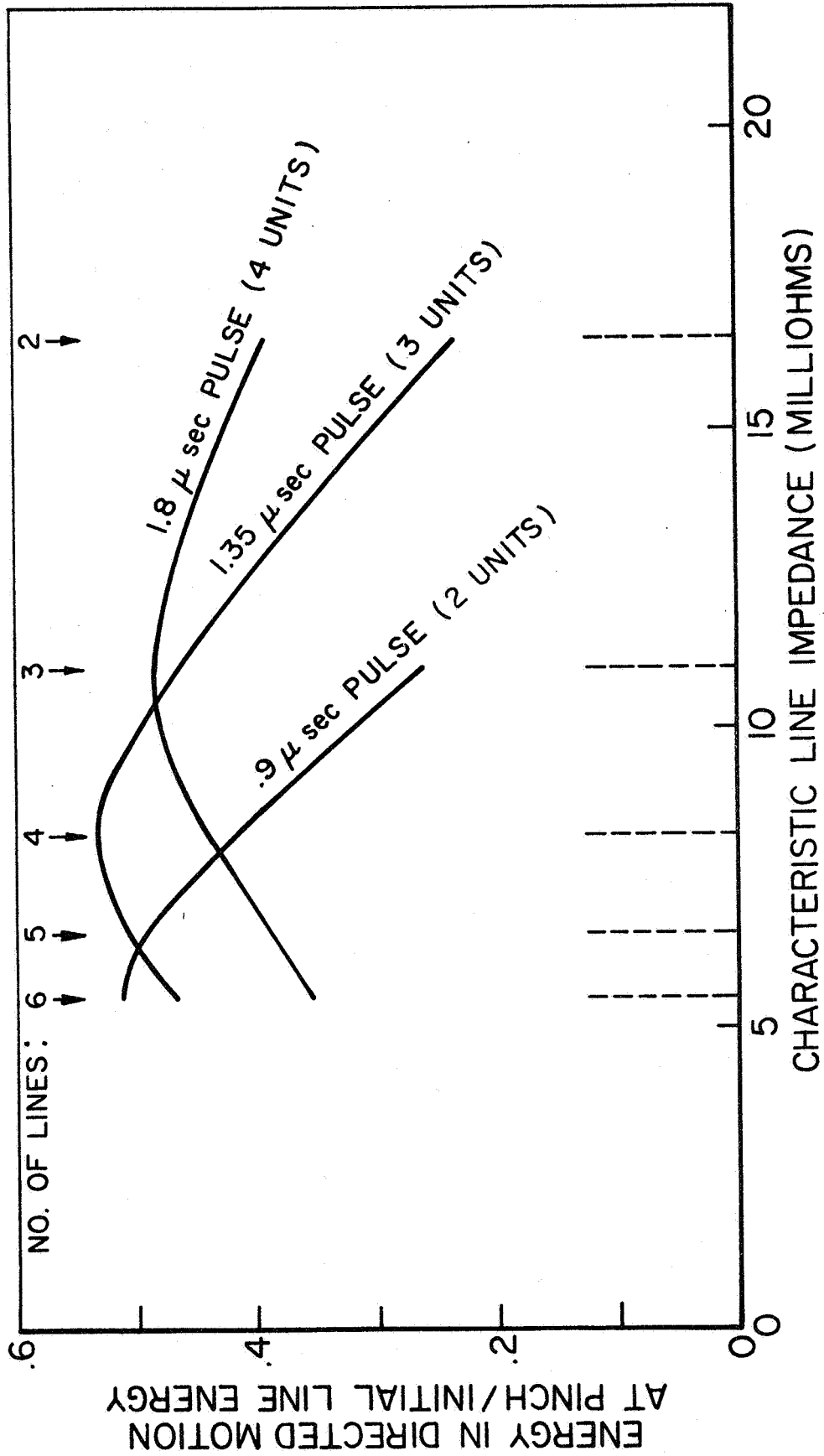
ENERGY TRANSFER vs CHARACTERISTIC IMPEDANCE

FIGURE 29
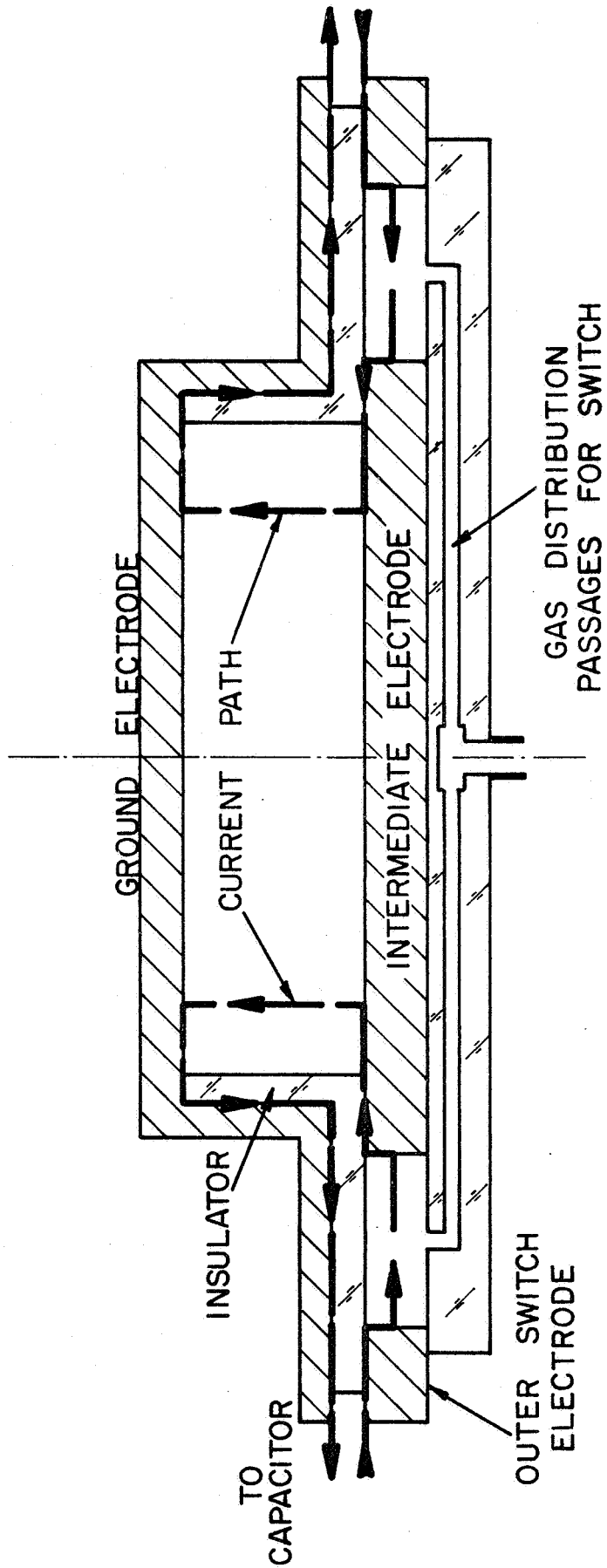
PINCH APPARATUS AND LOW INDUCTANCE SWITCH

FIGURE 30

V. PRESSURE MEASUREMENTS IN CLOSED CHAMBER DISCHARGES
(York)

Previous work on the problem of mapping the gas
pressure profile through a propagating current sheet has
dealt almost exclusively with improvement of the piezo-
electric probe response.[47,48] With a satisfactory unit
finally in hand, it has been possible during the present
reporting period to proceed to complementary tasks necessary
to relate probe output to plasma properties. Specifically,
a method of probe calibration has been developed; the geom-
etry of the discharge pattern driven by the pulse-forming
network and the interference of the probe with the discharge
have been examined experimentally using Kerr cell photography,
and various analytical methods of interpretation have been
considered.

The pressure probe calibration has been carried out
using a simple, single-diaphragm, constant area shock tube.
This method was chosen because it is highly reproducible,
it provides an impulse on the desired submicrosecond time
scale, and it permits calibration over a reasonable operating
range. In particular, it was desired to calibrate the probes
over a range of initial pressures near the ambient discharge
value of 100 μ and over as large as possible a dynamic pres-
sure increment, by subjecting them to the head-on reflection
of the shock from the tube end wall. However, it is well
known that low density shock tube behavior diverges from
classical inviscid behavior because of boundary layer
effects.[A-3] Rather than embark on a lengthy shock tube
calibration program, it was decided to rely on experimental
data published by Duff[A-4] and to construct a shock tube
with exactly the same internal dimensions. Accordingly, the
shock tube was assembled with a 1-1/8" i.d., a 3' driver and
7' driven section; the diaphragm was manually burst. Using

Duff's data on shock Mach number for given initial pressure and diaphragm pressure ratio, reflected shock data was taken over an ambient pressure range from 500 μ to 1.0 atm of argon with corresponding pressure jumps across the reflected shock of from 0.01 to 5.3 atm. Results indicated a linear response within experimental limits over the range tested, typically 0.20 volts/atm for PZT-S crystal 0.010" thick (Fig. 30).

Before attempting to interpret probe output in the pinch discharge environment, a series of radial-view Kerr cell photographs were taken of the discharge. This was accomplished by removing a section of the outer return conductor, allowing radial access to the interior of the chamber through the glass insulator as had been done previously.[29] A typical photograph of the imploding current sheet driven by the illustrated current waveform is shown in Fig. 31. Several familiar disturbances are evident on this and sequential photographs: 1) the anode "foot" phenomenon has enveloped a significant percentage of the interelectrode gap (see Section VI); 2) the main portion of the sheet is slightly concave inward; and 3) there is a small cathode foot. Nevertheless, it may be concluded from such studies that between radii of 3- and 1-inch and midway between the electrodes the sheet is relatively free of electrode effects and accordingly this will be the region of primary interest for the pressure probe diagnostics.

To pursue the problem of probe interference with the current sheet, several "dummy" models of probing shapes were inserted through the chamber walls and the luminosity patterns photographed again. The first shape to be examined represented a radial probe; Fig. 32a shows the probe interaction shortly after arrival of the sheet; Figs. 32b and c show a 4.5 x magnification of the area near the (sensing) end of the probe body taken at later times. From these photographs it is evident that at this probing position (r = 2") the probe is not
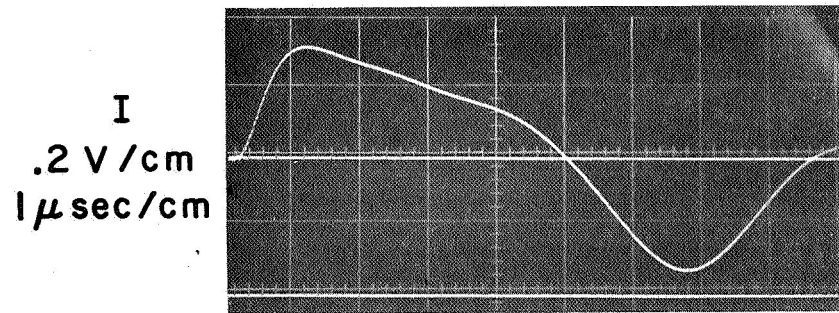
T-3122

ANODE
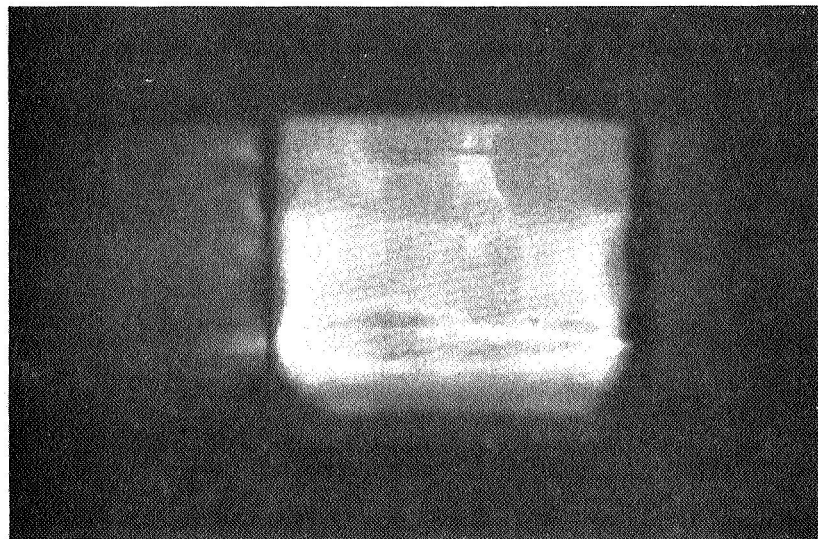
CATHODE

$100\,\mu$ ARGON, $2.5\,\mu$ sec

CURRENT SHEET AT r = 1.75"

RADIAL VIEW OF DISHARGE DRIVEN BY
PULSE FORMING NETWORK

FIGURE 31

ANODE

T-3128

CATHODE

a)   2.0 μ sec
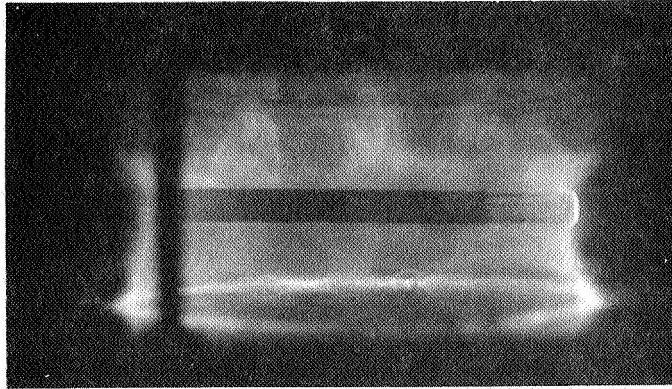
T-3133

b) 2.2 μ sec (MAGNIFIED 4.5 ×)

T-3135
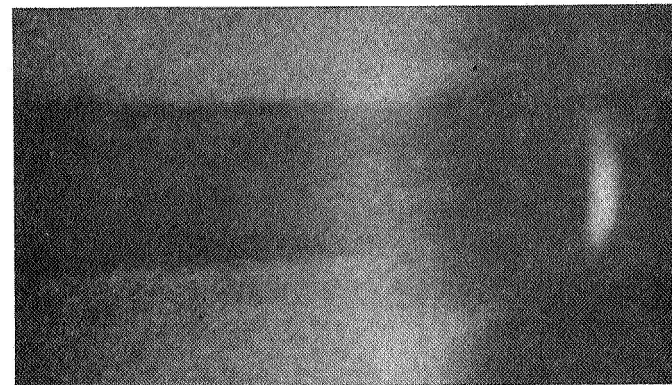
c) 2.4 μ sec (MAGNIFIED 4.5 ×)

LUMINOSITY PATTERNS ABOUT RADIAL PROBE
100 μ ARGON

FIGURE 32

immersed in the anode foot. However, the stagnation region of the probe is intensely luminous, and there is a typical contour of luminosity being shed from the stagnation region.

A similar sequence of photographs was taken of a dummy axial probe; Figs. 33a,b,c show luminosity patterns when the sheet first reaches the probe and at later times. Note that the flow again stagnates on the side (non-sensing) surface of the probe and this stagnated flow then diffracts over the end (sensing) surface. To examine possible means for reducing this disturbance to the sensing surface an annular flow isolator was slipped around the sensing end of the axial probe. Several luminosity photographs of this arrangement are displayed in Fig. 34. Figure 34a shows the shape shortly after arrival of the current sheet; this same picture is shown in 4x5 x magnification in Fig. 34b and at a later time in Fig. 34c. Clearly, the isolator substantially reduces leakage of the hot, stagnated gas over the sensing surface, but a weak bow wave is still evident from the leading edge of the isolator. Other configurations of isolator are presently being studied to minimize the distortion of the flow over the sensing surface from that prevailing in a virgin current sheet.

When the probe configuration has been optimized, simultaneous data on pressure, magnetic and electric fields, and luminosity profiles will be compiled, and combined with other measurements from earlier work, for the purpose of constructing a more detailed description of conditions within the sweeping current sheet.

T-3141

ANODE

CATHODE

a) 2.0 μ sec

T-3143

b) 2.2 μ sec
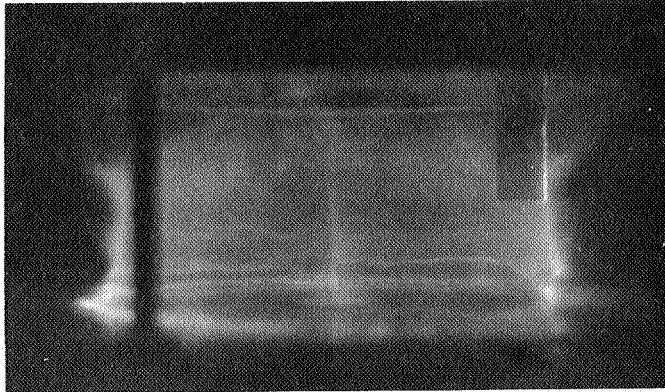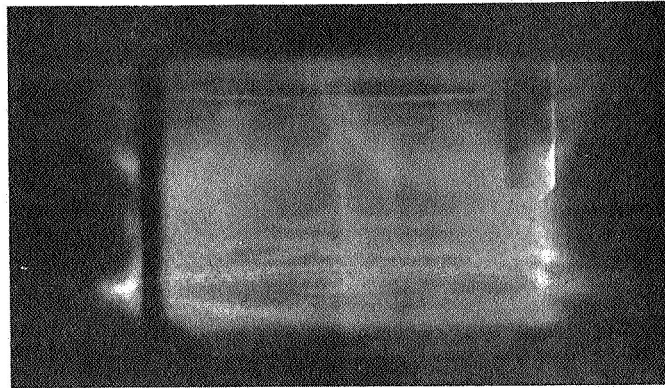
T-3144
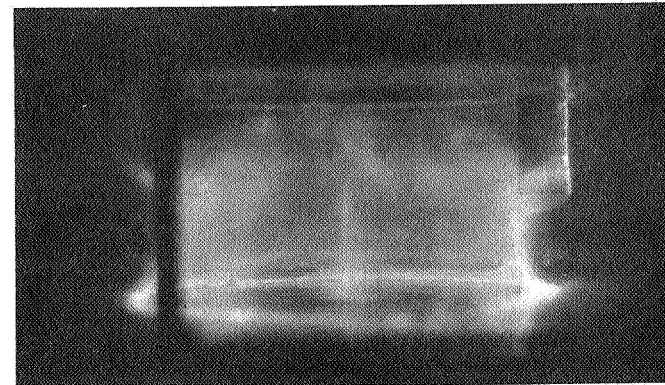
c) 2.4 μ sec

LUMINOSITY PATTERNS ABOUT AXIAL PROBE
100 μ ARGON
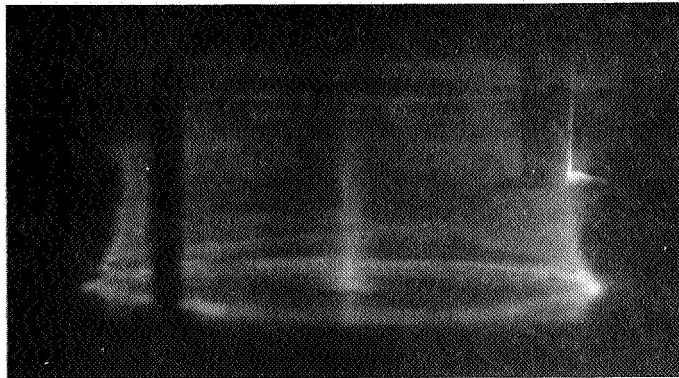
FIGURE 33

ANODE

CATHODE

T-3150

a)   1.6 μ sec

T-3150
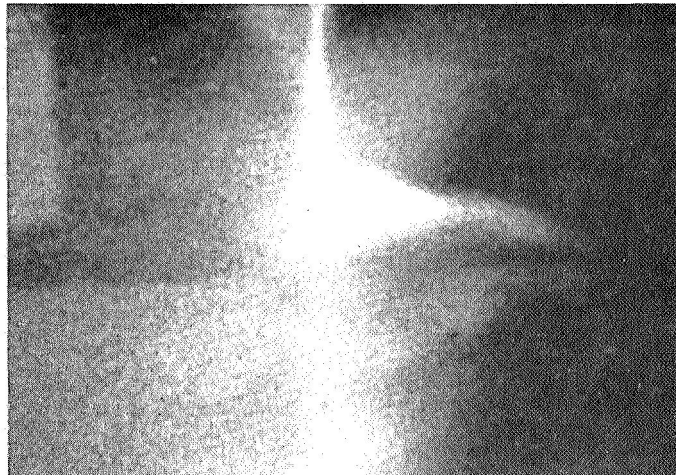
b)   1.6 μ sec (MAGNIFIED 4.5×)

T-3152

c)   1.7 μ sec (MAGNIFIED 4.5×)

LUMINOSITY PATTERNS ABOUT AXIAL PROBE
WITH FLOW ISOLATOR
100 μ ARGON

FIGURE 34

VI. CURRENT SHEET BEHAVIOR NEAR THE ANODE
(Oberth)

Previous reports have related certain observations of anomalous behavior of pinch current sheets near the anode surface.[47,48] Magnetic probe data indicate that under certain conditions the cylindrical current sheet will bifurcate near the anode, and attach itself to it in two more or less concentric rings. The position of bifurcation is found to regress from the surface as the current sheet advances radially, as shown schematically in Fig. 35. This "anode foot" structure has been found to occur in argon at various chamber pressures and with various flattop or double-peaked driving current pulses of magnitudes from 230,000 to 400,000 amperes.

Following these initial observations of this unusual current sheet behavior, attempts have been made to map the radial and axial electric fields in the "foot" region, but this has been precluded by an inordinate scatter in this data, a significant result in itself for these otherwise highly reproducible closed-chamber discharges. An example of the kind of irreproducibility encountered is shown in Fig. 36 which displays $\frac{\partial B_\theta}{\partial t}$, E_r, E_z oscilloscope traces of a "bifurcating" current sheet, taken at the chamber midplane.

The unusual irreproducibility of these measurements is interpreted to indicate that the discharge current experiences considerable difficulty in establishing a viable conduction mechanism near and into the anode surface, and thus is vulnerable to unspecified instabilities and turbulence in this region. Because of the possible importance of the anode sheath processes to the overall plasma acceleration problem, both in the pulsed and steady flow implementations, it has been decided to pursue this anode process further, despite
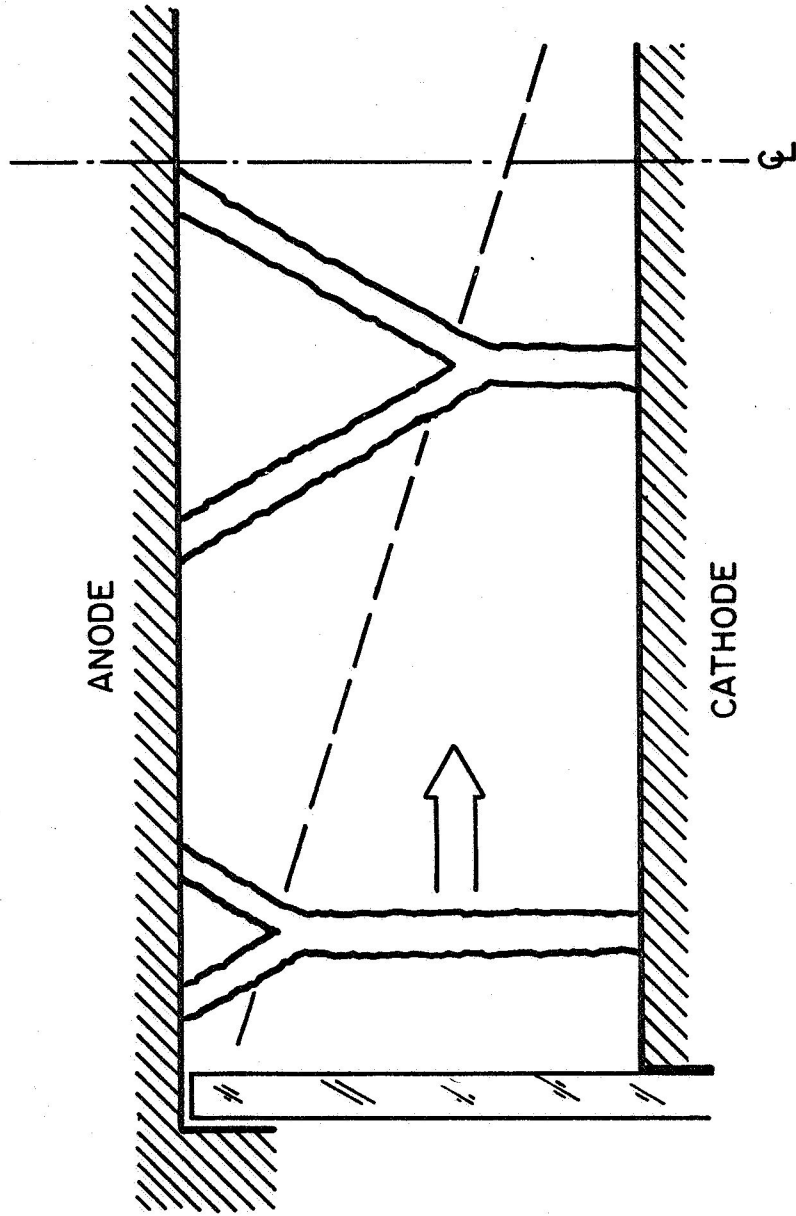
SCHEMATIC REPRESENTATION OF
ANODE FOOT DEVELOPMENT DURING PINCH

FIGURE 35

T-3229

E_r

$\frac{dB}{dt}$

2V / DIV

10 V / DIV

a)

T-3083

E_z

$\frac{dB}{dt}$

5 V / DIV

10 V / DIV
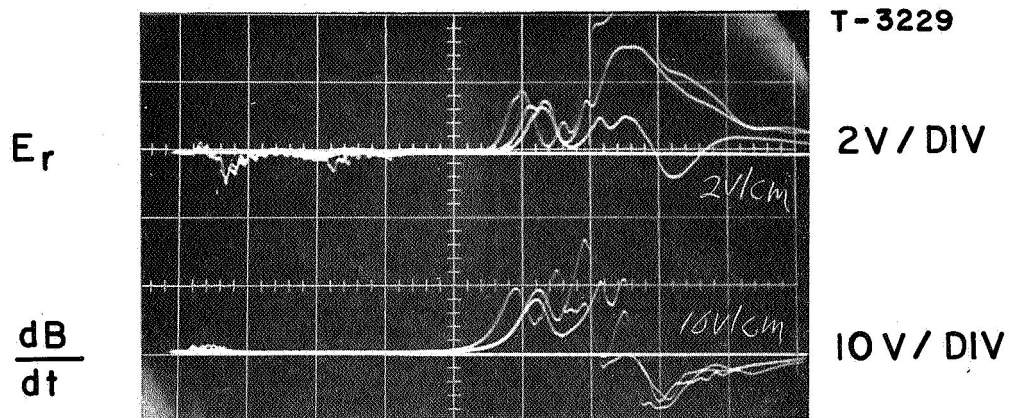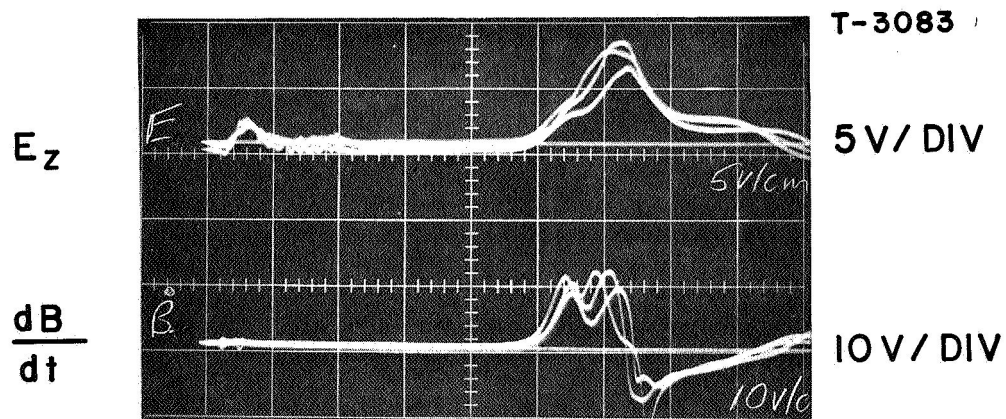
b)

$E_r, E_z, \frac{dB_\theta}{dt}$ SIGNATURES OF BIFURCATING
CURRENT SHEET IN 100 μ ARGON

FIGURE 36

its complexity, in the hope of acquiring at least some qualitative insight into the difficulty, and possibly of identifying a means of remedy.

In deference to the above mentioned irregularity of the process, a systematic photographic study has been undertaken to catalog the visual aspects of the domain before attempting further accumulation of electrical data. For this purpose, the same radial view Kerr cell photographic system described in the previous section was applied to this experiment (Fig. 37). All of the displayed photographs were taken in a 100 μ argon discharge in an 8-inch diameter chamber, driven by a 5.5 μsec x 230,000 amp current pulse. A magnetic probe visible in the photographs was also inserted axially into the chamber to provide $\partial B_\theta / \partial t$ records along with the Kerr cell photographs.

The first series of photographs displayed in Fig. 38 shows the progress of the pinching current sheet from 1.4 μsec to 3.8 μsec after initiation of the discharge. These pictures again show that the luminous front does divide and diffuse near the anode and that this disturbance grows towards the cathode as the current sheet propagates inward.

Correlation of such Kerr cell photographs with corresponding magnetic probe records allows one to relate the luminosity front to the current conduction regions of the sheet. Figure 39 compares photographs with the appropriate magnetic probe records for three different positions of the probe. In Figure 39a both the luminosity pattern and magnetic probe data indicate a single current conduction zone at the midplane. In Fig. 39b the magnetic probe has been positioned 1/2" from the anode. The photograph shows the probe standing between the two "legs" of the bifurcated current sheet. The corresponding probe trace shows that one current conduction region has swept over the probe prior to 1.8 μsec and that a second current zone is about to pass the probe. Apparently,
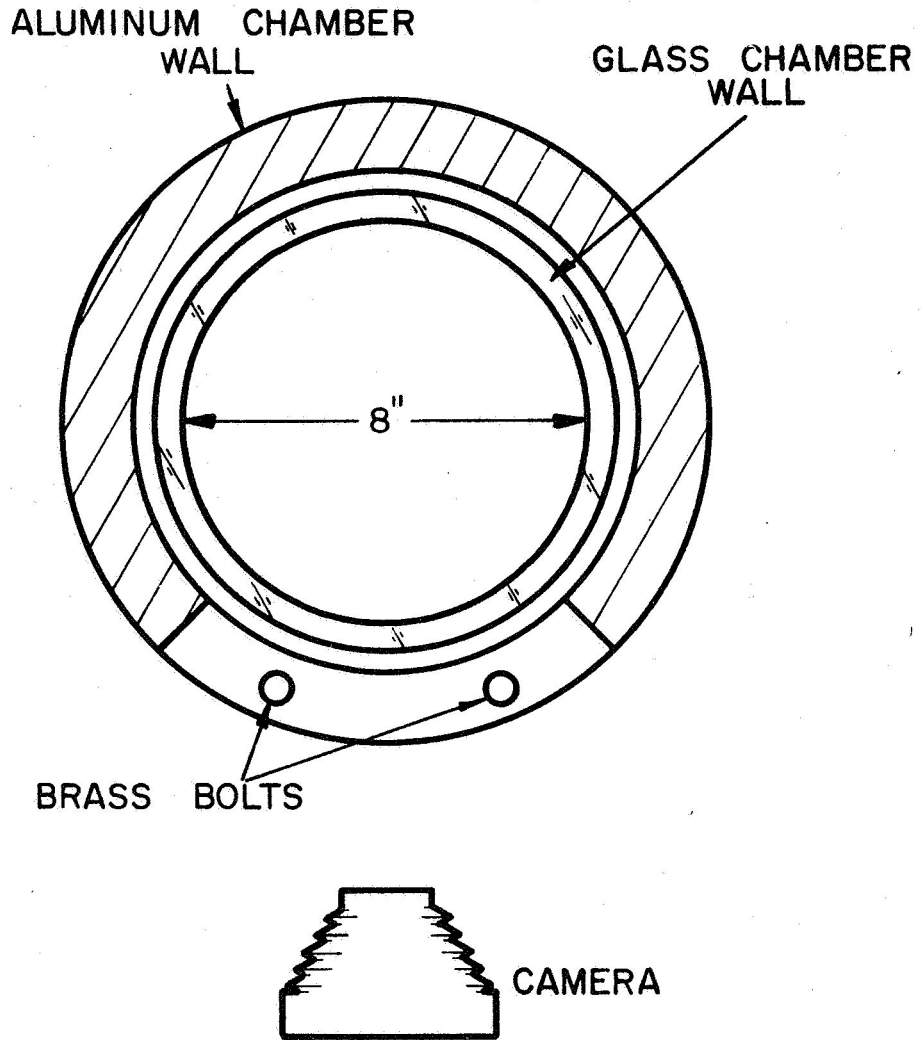
KERR CELL CAMERA ARRANGEMENT
FOR FOLLOWING PHOTOGRAPHS

FIGURE 37

a) T-3317 1.4 μsec — CATHODE / ANODE
b) T-3321 1.8 μsec
c) T-3326 2.2 μsec
d) T-3328 2.6 μsec
e) T-3332 3.0 μsec
f) T-3334 3.4 μsec
g) T-3335 3.8 μsec

74
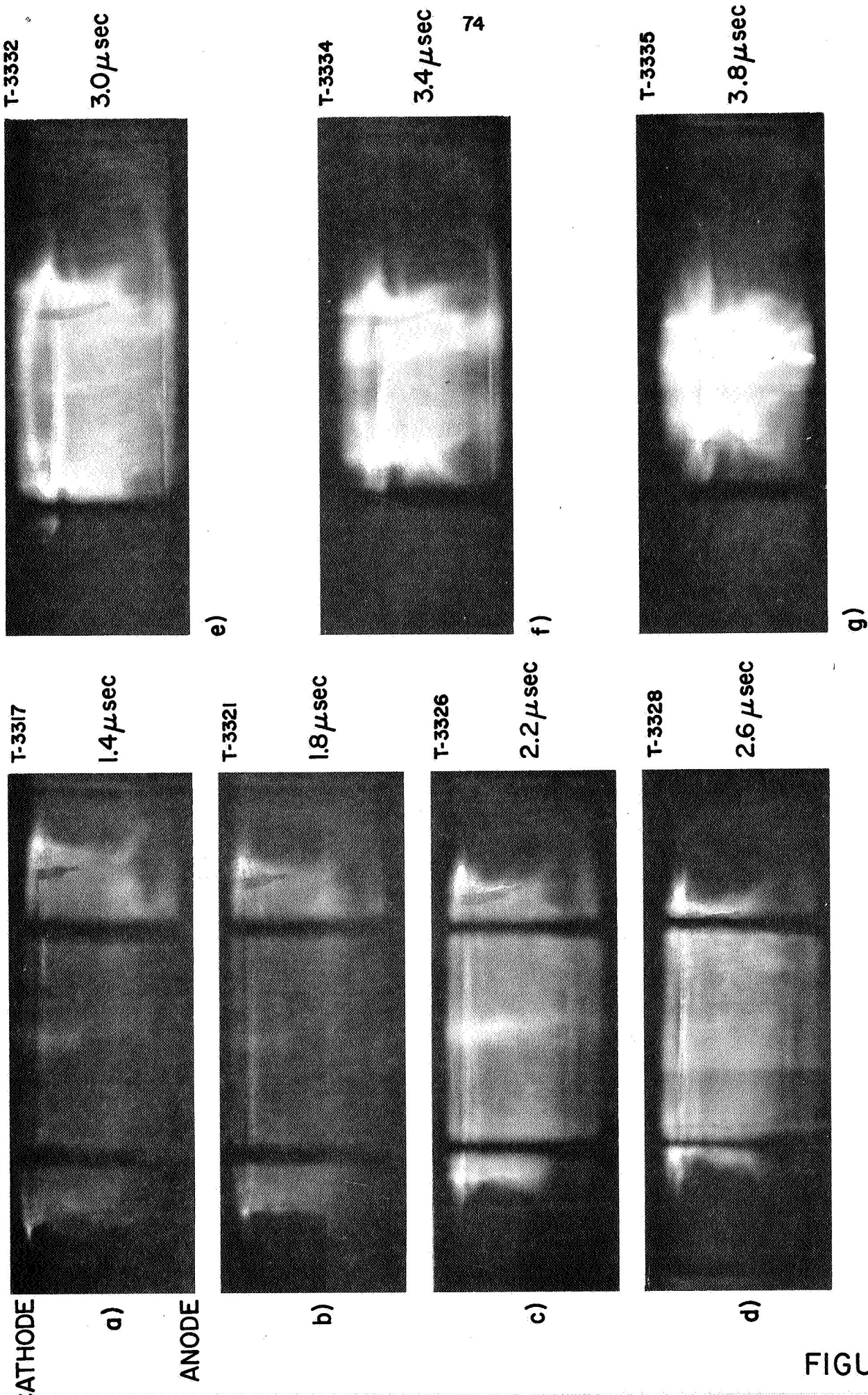
PROGRESS OF BIFURCATING CURRENT SHEET IN 100 μ ARGON
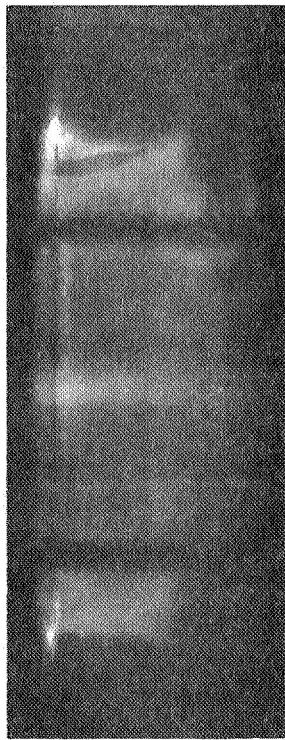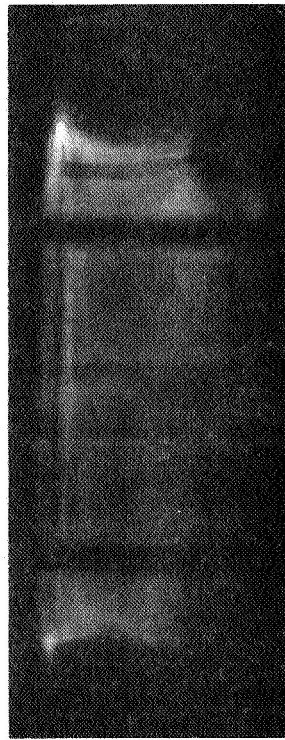
FIGURE 38

MIDPLANE

1/2" FROM
ANODE

1/4" FROM
ANODE

I

$\dfrac{dB}{dt}$

I

$\dfrac{dB}{dt}$

I

$\dfrac{dB}{dt}$

T 3322

ANODE

1.8 μ sec

a)

T 3323

ANODE

1.8 μ sec

b)

T 3324

ANODE

1.8 μ sec

c)
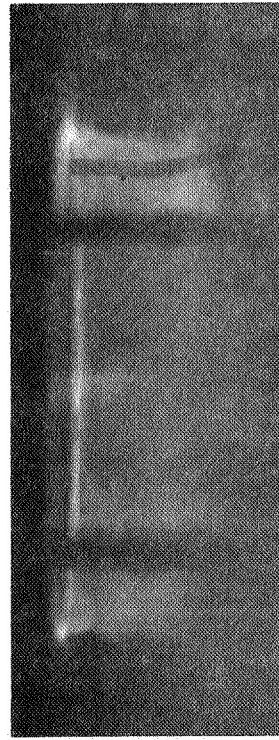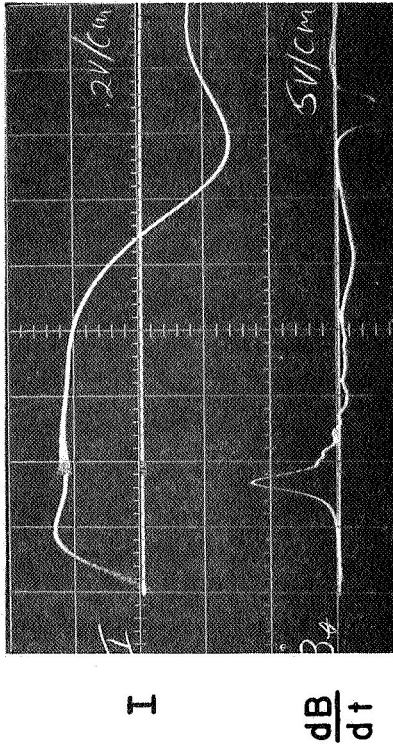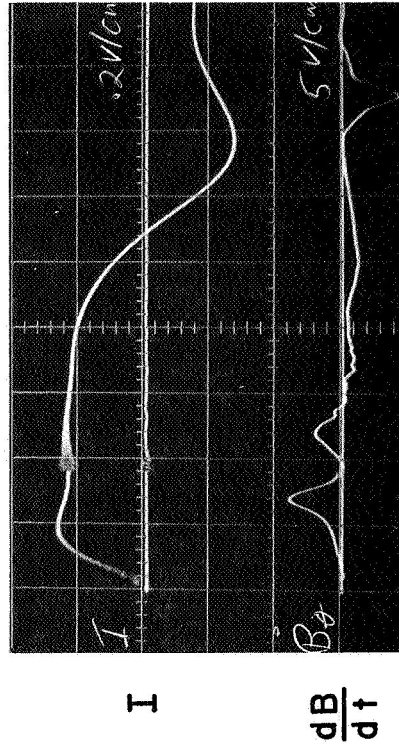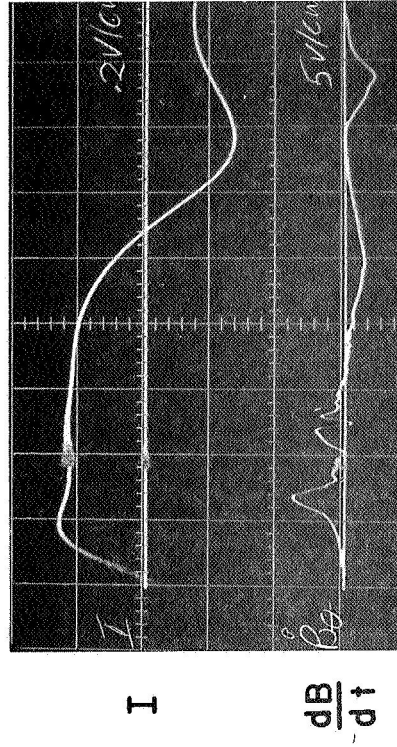
SIMULTANEOUS   KERR   CELL   PHOTOGRAPHS   AND   MAGNETIC   PROBE   RECORDS

FIGURE 39

then, each part of the bifurcated luminosity front has a current conduction region associated with it. Figure 39c with the magnetic probe at a position 1/4" from the anode further supports this conclusion.

Under certain conditions another aspect of the anode process has been observed photographically. When a highly polished aluminum electrode is employed, a distinct filamentary "spoking" is found to occur at a random spot on the anode. Figure 40 illustrates the situation: at the early times we see the familiar bifurcated anode attachment, but later, at about 2.6 μsec, a luminous "spot" is seen to form on the anode surface. This luminous spot intensifies as the current sheet propagates inward. From many photographs of this type, we conclude that the "spoke" does not form at any one particular point on the anode, but seems to attach at a different point for each discharge. Little is presently known about the current densities associated with this "anode spoke," but such information will be sought in future investigations. It seems reasonable, however, that such instabilities give rise to the irreproducible electric probe data displayed earlier.

In the course of this qualitative photographic survey, it seems reasonable to try to establish the pressure dependence of the anode foot processes. Figure 41 shows photographs of current sheets propagating into ambient argon at pressures of 50 μ, 100 μ, and 200 μ at approximately the same radial positions. In each case the driving current is constant at about 200,000 amperes for the times indicated. Each photograph shows the familiar current sheet bifurcation near the anode, with little drastic change in scale over the range tested. In fact, the degree of similarity among the three figures would seem to indicate that chamber pressure is not a critical factor in determining the current sheet behavior near the anode.
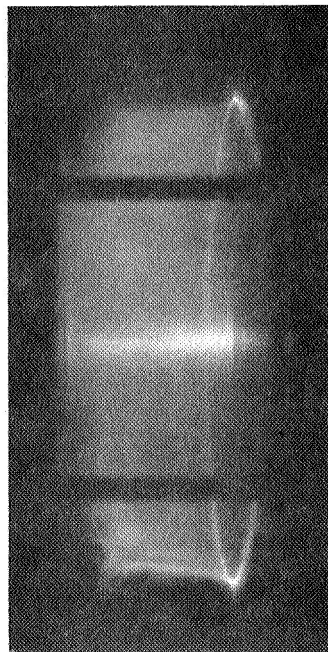
T-3361
2.8 μ sec

d)

T-3359
3.0 μ sec

e)

T-3360
3.4 μ sec

f)

T-3355
1.8 μ sec

a)

T-3357
2.6 μ sec

b)

T-3358
2.8 μ sec

c)
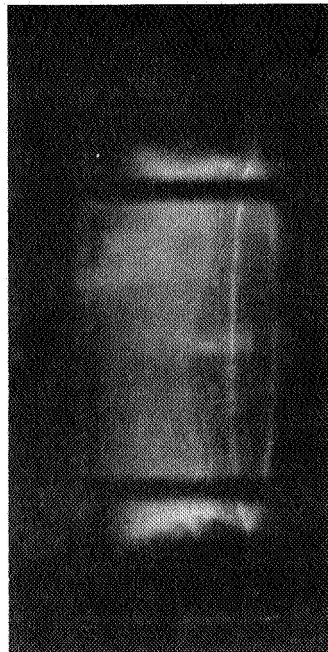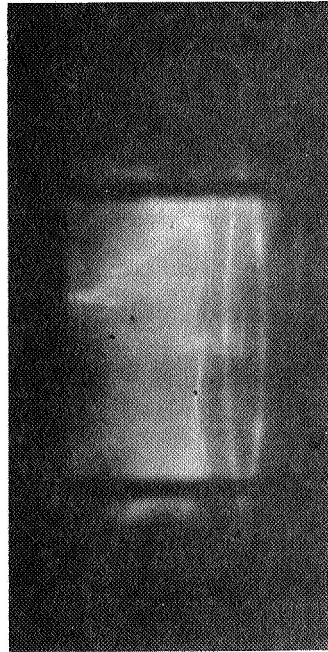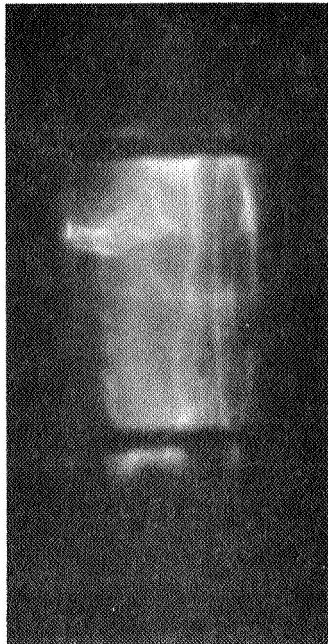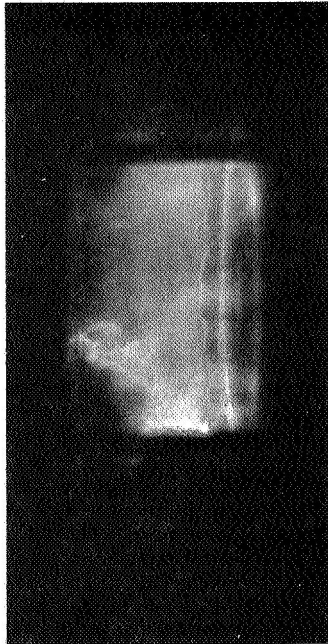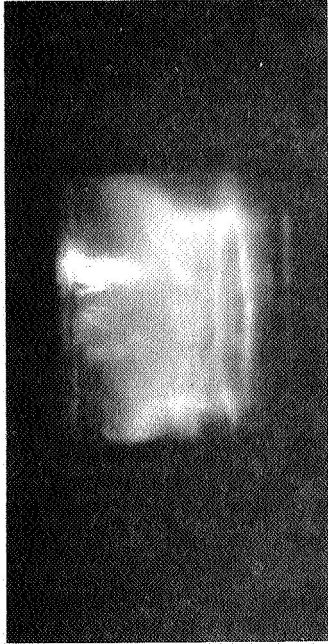
ANODE

CATHODE

FORMATION OF ANODE SPOKE

FIGURE 40

ANODE

CATHODE

T-3363

1.8 μ sec

a)   50 μ ARGON

T-3352

2.6 μ sec

b)   100 μ ARGON

T-3374

3.4 μ sec
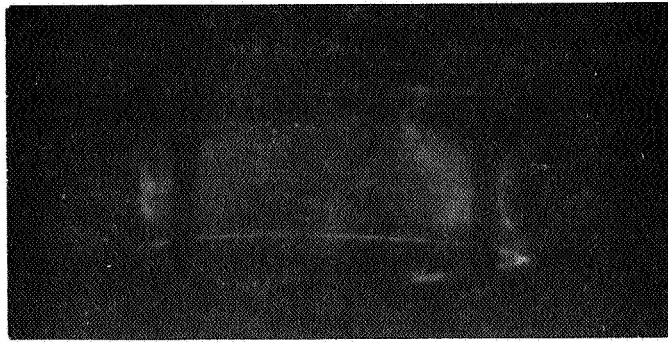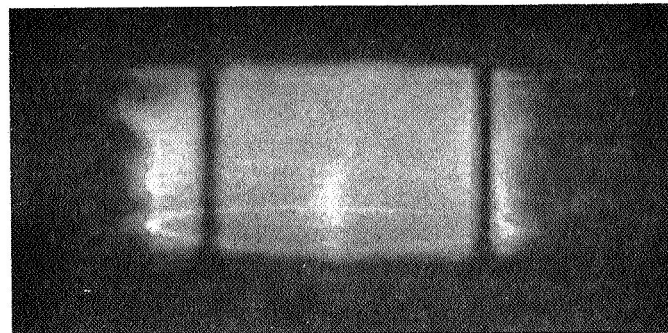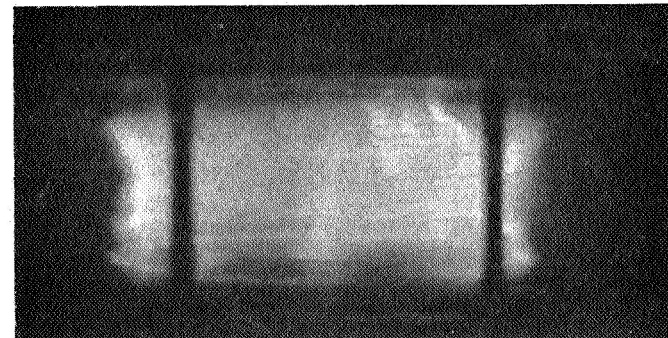
c)   200 μ ARGON

PRESSURE DEPENDENCE OF ANODE FOOT

FIGURE 41

Clearly, similar surveys of the effect of discharge current amplitude, pulse shape, gas type, electrode type and surface condition, and chamber geometry will be needed to localize the physical cause of the anode foot, prior to its more detailed examination.

VII. GAS LASER INTERFEROMETRY
OF CLOSED CHAMBER DISCHARGES
(Bruckner)

Among the various optical techniques available for
the investigation of electron and ion densities in ionized
gases, interferometry offers the best compromise between
experimental simplicity and ease of interpretation of data.
Of particular significance to interferometry has been the
advent of the laser and the development of new interfero-
metric methods which are based upon self-modulation of the
laser cavity by its own reflected light.[A-5,A-6,A-7] A
schematic diagram of one possible technique of this type
is sketched in Fig. 42. The output from the laser is sent
through the plasma, and reflected back onto itself by the
planar mirror M_3. The amplitude of the laser output depends
upon the phase of the signal which returns into the laser
cavity from the mirror system M_2 - M_3 , which in effect con-
stitutes a high Q cavity whose resonant frequencies depend
upon the refractive index of the plasma.[A-8] If the plasma
density changes with time, a sequence of resonances at the
laser frequency will be excited in the cavity. Since the
phase of the signal returning to the laser depends on the
proximity to resonance, the laser output will vary, attaining
an extreme value each time the external cavity, M_2 - M_3 is
swept through a resonance. Each complete cycle of light
intensity is called an interferometric fringe.

A number of preliminary experiments with devices of
this type have been reported previously.[43,47] These in-
cluded a determination of the frequency response of the inter-
ferometer, and a measurement of the refractive index of
neutral argon to check that a changing index did indeed pro-
duce fringing. A few feasibility studies of probing the pinch
discharge itself were also attempted, and while these showed

LASER INTERFEROMETER

FIGURE 42
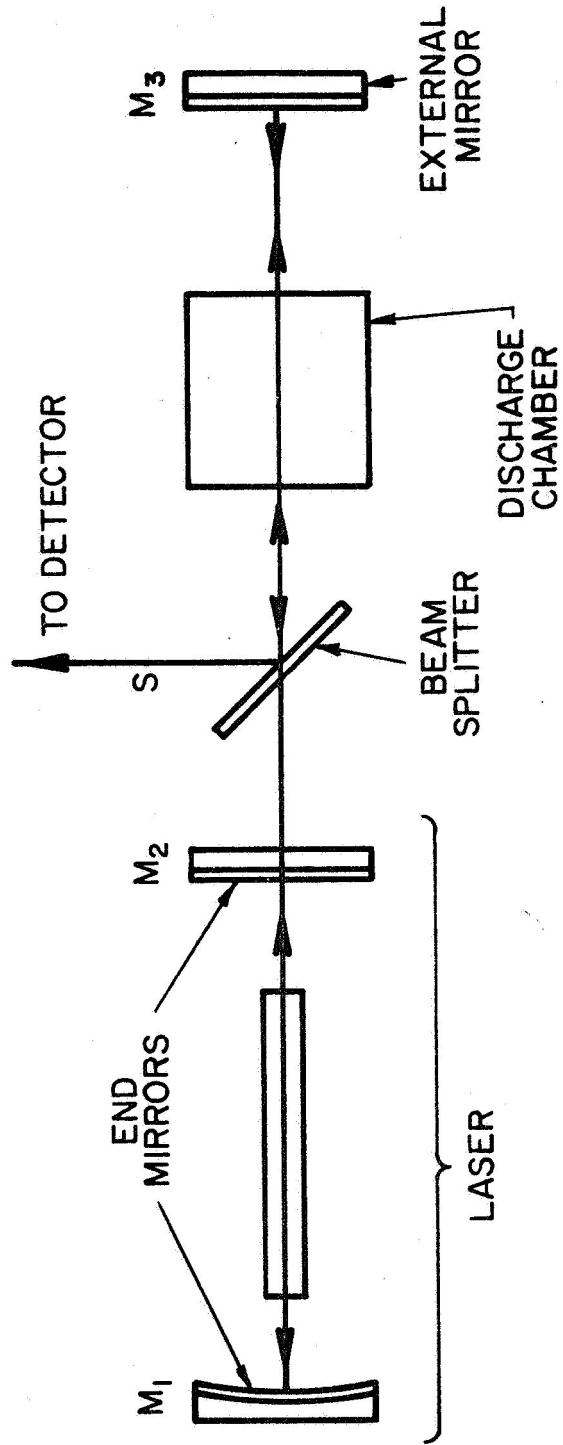
promising results, they also indicated a need for more sophisticated experimental facilities.

In this direction, an improved optical bench has been constructed, and applied to an 8-inch diameter pinch discharge chamber as shown in Fig. 43. A front-surface mirror, M_4 , deflects the laser beam through a 6-inch slot in the optical bench into the chamber via a 6-inch diameter glass insert in the upper electrode. The mount supporting M_4 also holds the beam splitter and one of the two Corning CS-2-62 #2418 red cutoff filters. The other filter is interposed between the iris diaphragm (stopped down to $\sim$ 1.5 mm) and the photomultiplier tube (RCA 1P28). To the top of the chamber, where the laser beam enters, is affixed a mask also with a 1.5 mm orifice. The purpose of these red filters and diaphragms is to exclude a large portion of the plasma radiation from the photomultiplier.

During pinch diagnostics the external resonating cavity, bent at a right angle by M_4 , is formed by laser mirror M_2 and mirror M_3 , a small, thin, second surface mirror attached to the bottom electrode of the pinch chamber. By interposing another mirror, M_5 , shown in dotted lines, the external cavity can be bent again such that it is bounded by the six-sided rotating mirror of an AVCO Type MC 300 streak camera. By causing the beam to fall on this mirror off the axis of rotation, the length of the external cavity, and hence the laser output, can be modulated at will through a wide range of fringing frequencies by simply varying the speed of rotation of the mirror. In this manner the frequency response of the laser (i.e., variation of depth of modulation with fringing frequency) may be obtained. This particular property of the laser is of prime concern because it is expected that the electron density gradients encountered in the propagating current sheets will predicate fringing rates as high as 100 MHz (Ref. 7).
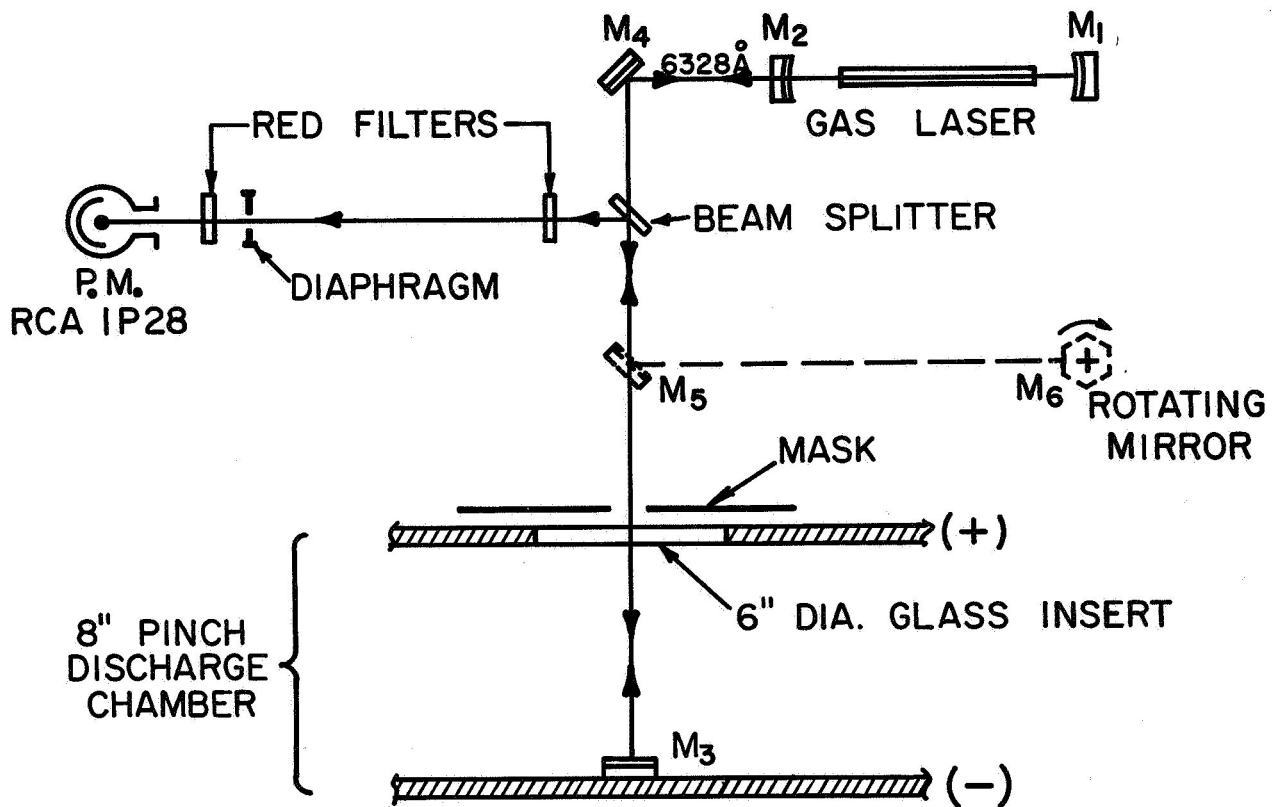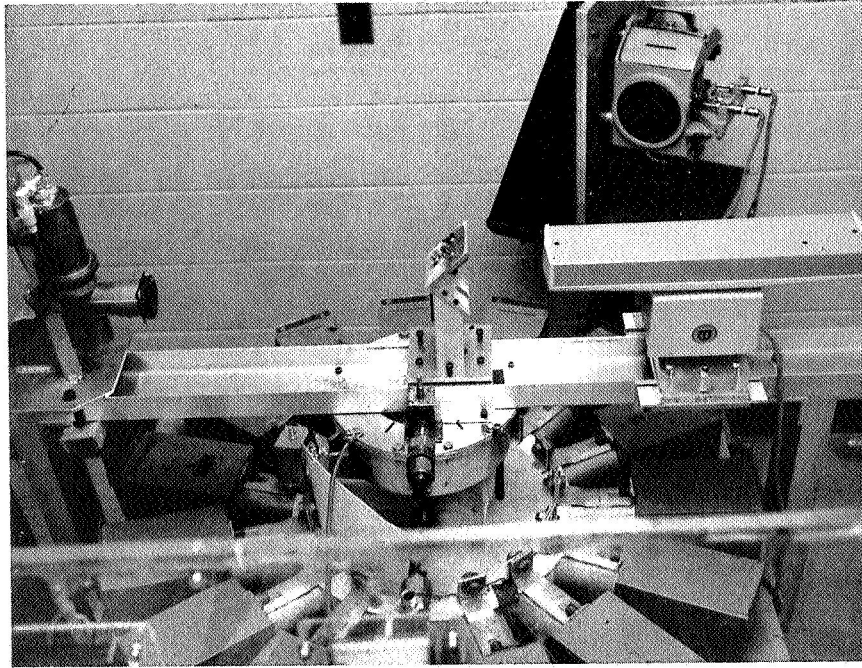
INTERFEROMETER INSTALLATION
ON PINCH CHAMBER

FIGURE 43

By spinning the rotating mirror with a regulated nitrogen gas supply, the interferometer has been modulated at frequencies from about 250 KHz to over 40 MHz. No higher frequencies were attempted because of the falloff in the oscilloscope (Tektronix 547) response above 50 MHz. The results are plotted in Fig. 44, along with results of a previous frequency calibration of another laser interferometer. It is seen that the interferometer in present use seems quite capable of following the high frequency fringing expected from the electron density changes in the pinch, and indeed may be superior to the earlier device at very high frequencies. This is indicative of the difference between the Q of the earlier and present external cavity configurations.

As a first application of the equipment described above, the pinch discharge has been probed at three radial positions (2.06 cm, 2.86 cm, and 5.63 cm) and at various initial argon pressures (50 μ, 100 μ, 150 μ, 200 μ, 300 μ, 500 μ, and 750 μ). At the radius of 5.63 cm, with an initial argon pressure of 150 μ, it was found that of the 13 interferograms taken six exhibited a fair degree of similarity to each other, to the extent of the temporal positions of the fringe peaks relative to each other and to discharge initiation. With reference to Fig. 45, fringing is seen to begin at an average of 3.6 μsec after electrical breakdown and goes through approximately one slow cycle lasting about 1.8 μsec. At 5.4 μsec a very sharp peak occurs corresponding to a very steep electron density gradient. Another sharp peak occurs at 6.7 μsec, the two peaks being separated by one broad cycle lasting 1.3 μsec.

Because of the multiple current sheets produced in this particular pinch device, and because there is the ambiguity that a fringe can be caused by either a positive or negative electron density gradient, the interpretation of the interferograms is difficult and questionable beyond a certain
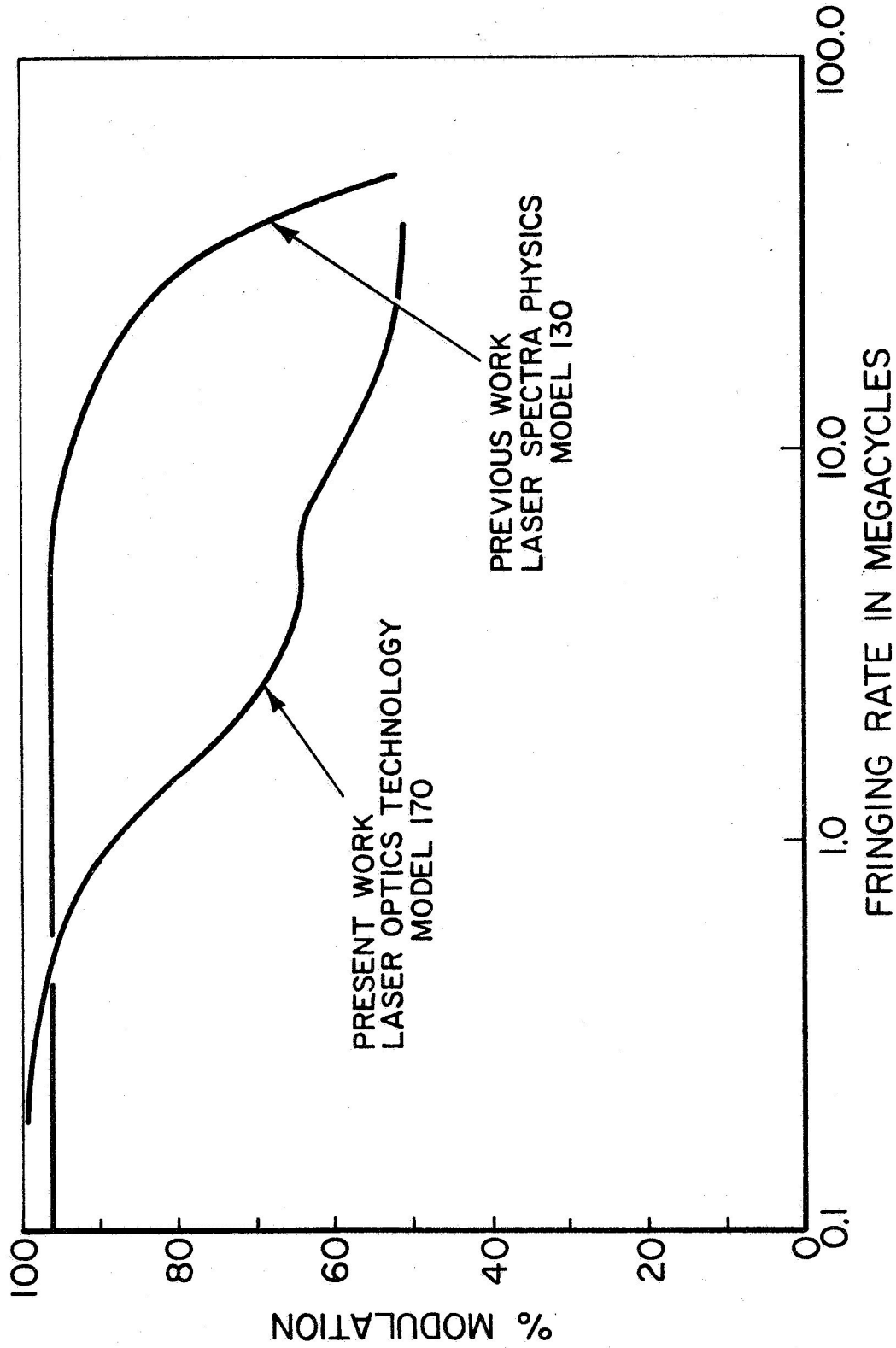
FREQUENCY RESPONSE OF THE LASER INTERFEROMETER

FIGURE 44

I

INTERFERENCE
FRINGES

a)

198
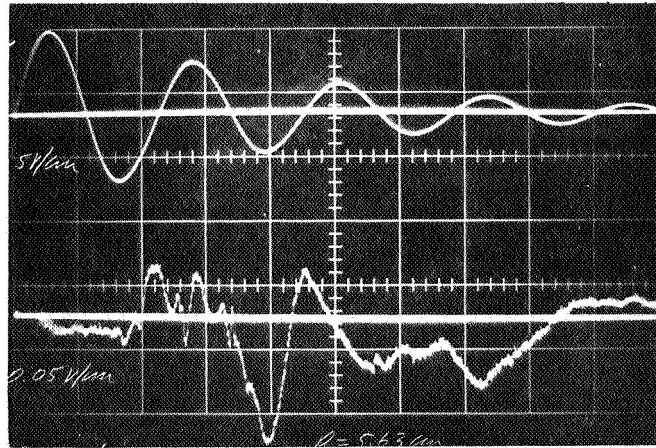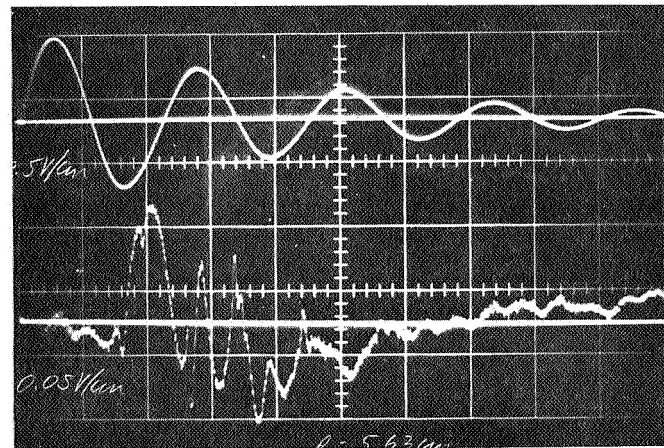
2μ sec / DIV
P = 150 μ ARGON
R = 5.63 cm

b)

208
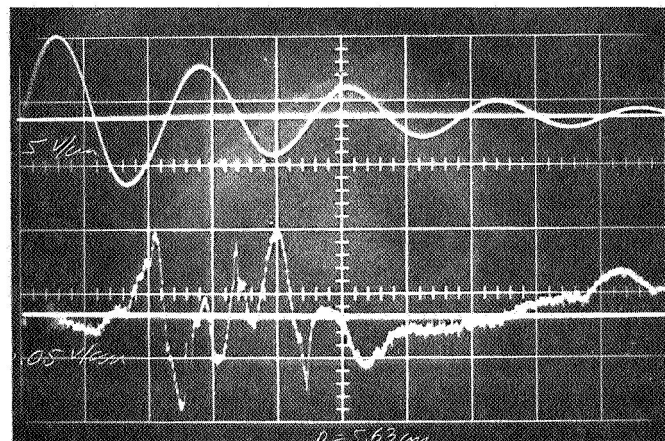
c)

INTERFEROMETER RESPONSE
TO PINCH DISCHARGE

FIGURE 45

point. However, with the help of results from a microwave
interferometer,[50] an attempt has been made to translate
the interference patterns into time dependent electron den-
sities. Up to the first sharp fringe peak, interpretation
is straightforward--the initial slow fringe cycle must clearly
correspond to an increase in electron density associated with
the initial portion of the current sheet. Likewise, the sharp
peak indicates a pronounced steepening in the density profile.
However, interpretation of the fringe cycle separating the two
sharp peaks, and the second sharp peak itself is somewhat am-
biguous. On the basis of results found in Ref. 50, one may
conjecture that these two features represent the attainment
of a peak in the electron density profile followed by a sudden
falloff in density, respectively, in which case the electron
concentration profiles corresponding to each of the oscillo-
grams of Fig. 45 are as shown in Fig. 46.

Unambiguous identification of reversals of laser out-
put intensity now remains the major difficulty. Two tech-
niques may be considered: 1) the use of two wavelengths of
light produced by a laser in which the atomic transitions
giving rise to the distinct wavelengths do not have a common
upper energy level; and 2) the application of mechanically
induced, high frequency modulation of the interferometer with
a rotating mirror or other device.

The two-wavelength technique capitalizes on the fact
that the fringing frequency is proportional to the wavelength
of the laser light. Simultaneous monitoring of the inter-
ference occurring at the two wavelengths would permit unique
assignment of electron density gradient sign, provided the
wavelength difference is great enough to displace the two
corresponding maxima a measureable amount.

The mechanical modulation technique essentially con-
sists in setting up a controlled very high frequency ($>$ 100 MHz)
"carrier" fringe sequence which is then frequency modulated by
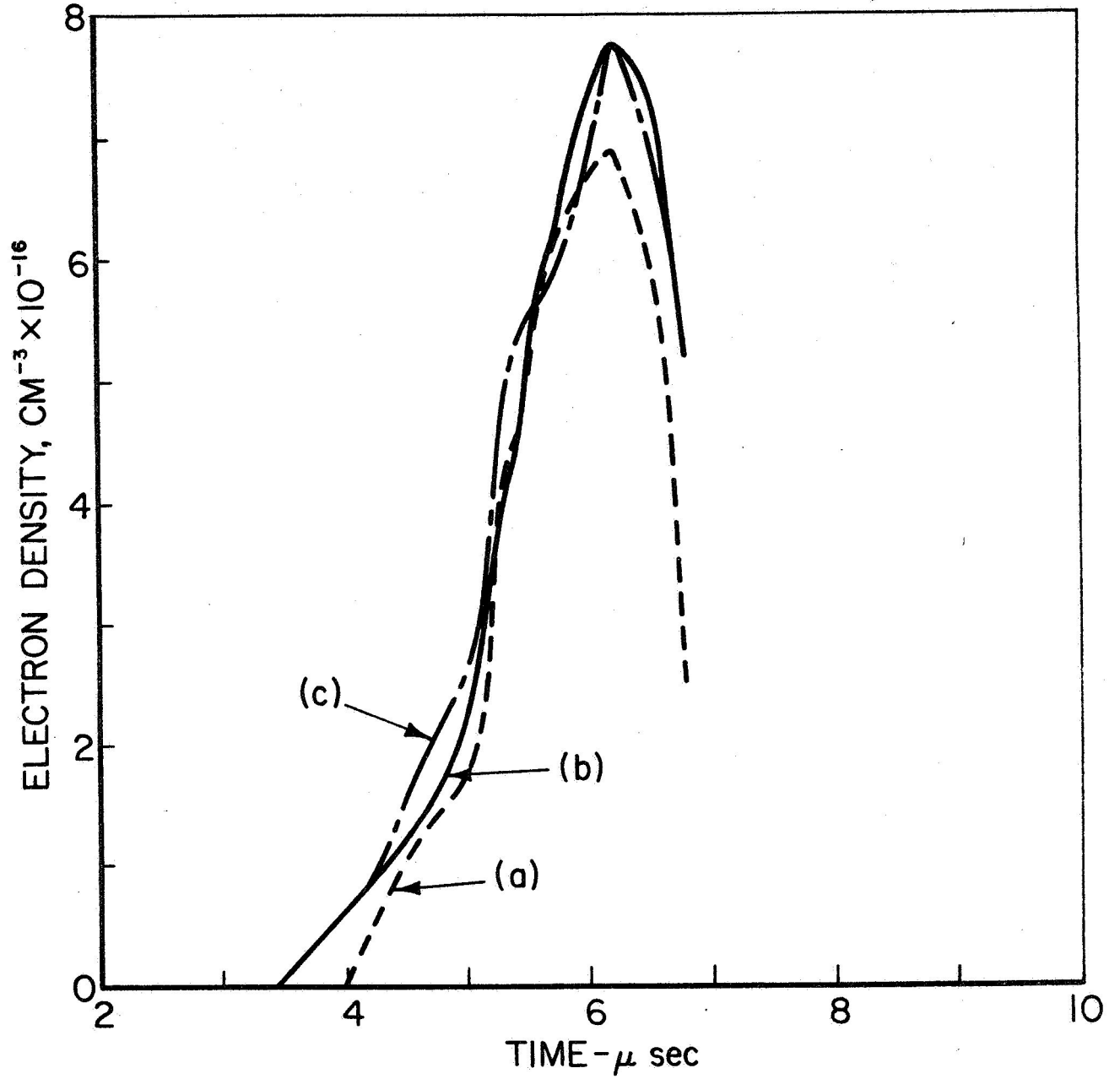
ELECTRON DENSITY PROFILE
THROUGH CURRENT SHEET

FIGURE 46

the changing refractivity of the plasma. Knowing beforehand
in which direction the mechanical modulation is changing the
resonator length, one can determine the sign of the electron
density gradient from the frequency variations it imposes
upon the carrier fringes; i.e., suppose the carrier fringing
is set up by a mechanical rate of increase in cavity length.
Then, a positive electron density gradient, which effectively
amounts to a decrease of optical path length, would lower the
frequency of the carrier. Similarly, a negative density gra-
dient would increase the carrier frequency. In order to deter-
mine the magnitude of the density gradient, one still requires
the fringe pattern set up by it alone. This pattern can be
separated from the frequency modulated carrier fringe signal
by a suitable detector, or may be obtained from another dis-
charge at the same conditions if there is good shot-to-shot
reproducibility.

At present, both of the above methods are being ex-
plored for possible application to the pinch experiment. When
the technique is satisfactorily established, the interfero-
meter will be moved to one or more of the more modern dis-
charge devices where it can contribute more effectively to our
understanding of the propulsion-oriented plasma processes.

VIII. CURRENT–VOLTAGE CHARACTERISTICS
OF HIGH CURRENT DISCHARGES
(Di Capua)

Terminal voltage measurements in pulsed plasma acceleration research here and elsewhere have conventionally been employed to monitor the progression of plasma currents via the associated inductance changes, and to estimate the apportionment of input energy to the kinetic and thermal modes of the plasma. Under typical pulsed plasma operation, inductive potential drops normally dominate the resistive drops and some subtlety needs be exercised in precise determination of the latter. As our work enters the domain of quasi-steady acceleration, however, the inductance time derivative disappears, leaving the plasma resistance and the motional impedance of gas streaming across fixed fields as the only components of the real impedance. For this reason, and because the details of the electrode fall processes are becoming progressively more essential to a better understanding of all plasma accelerators, both pulsed and steady, more precise techniques for determination of the current-voltage characteristics of very high current discharges need to be developed.

One might naively assume that the literature abounds with data of this sort in view of the preoccupation of physicists of an earlier day with electrical discharge phenomena. On closer study, however, such data is found to be sparse and contradictory for discharge currents above 1,000 amperes or so, for the reason that the very same motional effects exploited in plasma propulsion begin to obscure the desired static discharge characteristics at these current levels. Specifically, to make a valid measurement of arc resistance in the $10^3 - 10^6$ ampere range, one must take care to eliminate or to precisely evaluate all voltage contributions associated with plasma motion, gas entrainment, and excessive arc column constriction.

As a first attempt at this class of measurement, a facility has been designed and constructed to drive a quasi-static current of $10^4 - 10^5$ amperes through a suitable discharge chamber. A 5-inch diameter cylindrical pinch geometry is chosen because of its operational reproducibility and accessibility for instrumentation. Also, it is hoped that its terminal plasma configuration, i.e., a single arc column on the axis, will minimize the gas ingestion contribution to the voltage signature, since this gas must stagnate at the column centerline. The power source, patterned after our other tailored-pulse supplies,[35,37] consists of five lines of 10 - 1 μfd elements. Each line, when charged to 10 kv, is capable of delivering about 20,000 amperes for about 10 μsec. These lines may effectively be compounded in any series-parallel combination to produce current pulses of nominally 20, 40, and 100 kiloamperes. Thus, the voltage signatures of progressing current distributions may be studied at various current amplitudes.

Voltage measurements across the discharge chamber are made both externally and through an inner divider. External measurement of chamber voltage, V_C , is obtained by a Tektronix P6013 probe connected to a terminal protruding from the lower electrode of the discharge chamber as shown in Fig. 47. The inner divider measurement, V_I , involves a teflon insulated brass rod placed at the center of the chamber in contact with the lower electrode as also shown in Fig. 47. Figures 48a,b,c shows the response of the external probe V_C for three driving current amplitudes, I. Figures 49a,b,c shows corresponding responses of the inner probe, V_I , which represents only the resistive component of the terminal voltage. Figures 50a,b,c compares the difference of external and internal probe signatures $(V_I - V_C)$ with the time derivative of total current, $\frac{dI}{dt}$. By application of Faraday's law to the dotted contour of Fig. 47, the voltage difference $(V_I - V_C)$ can be assigned to the time derivative of the magnetic flux which is linked by
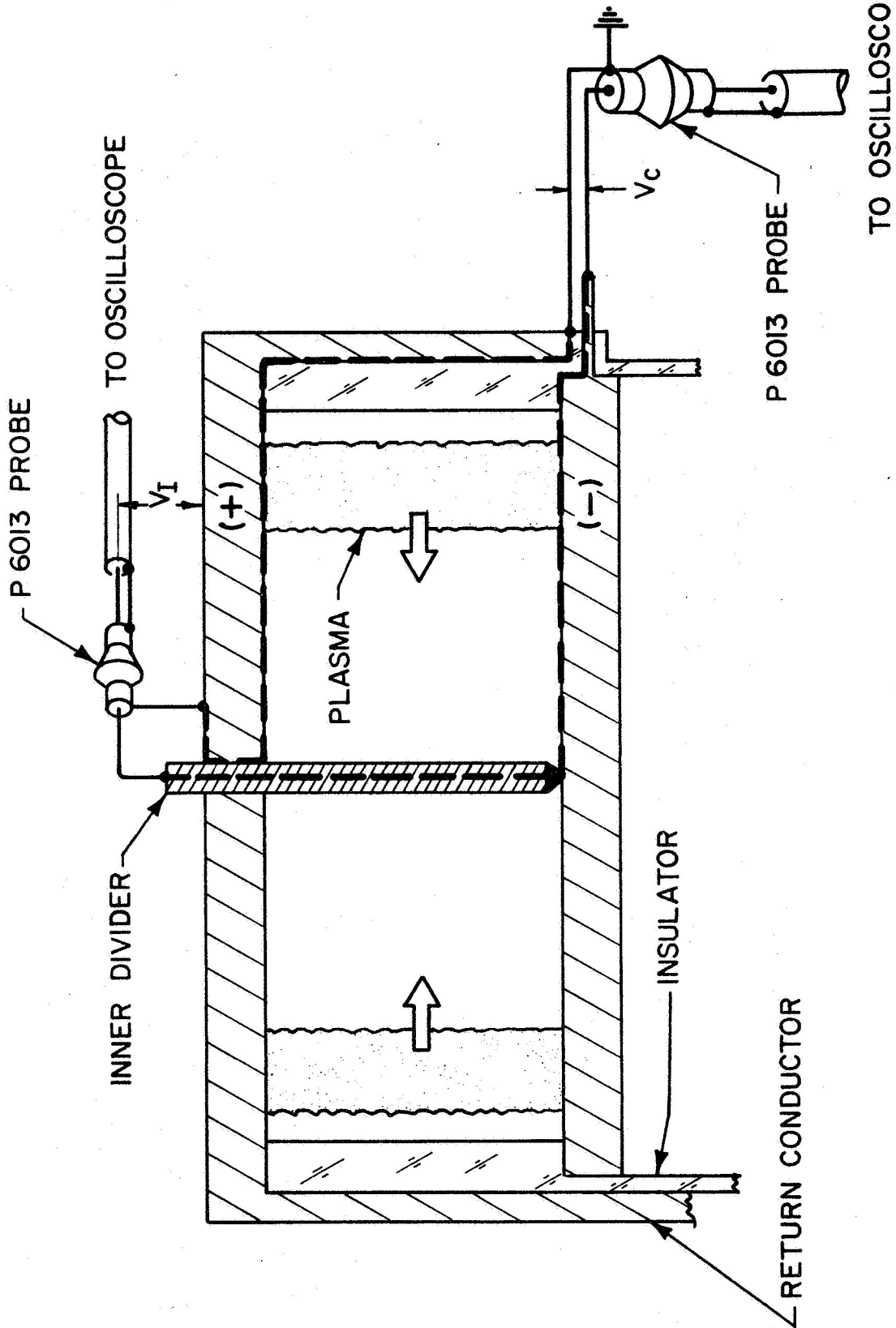
DISCHARGE VOLTAGE MEASUREMENTS

FIGURE 47
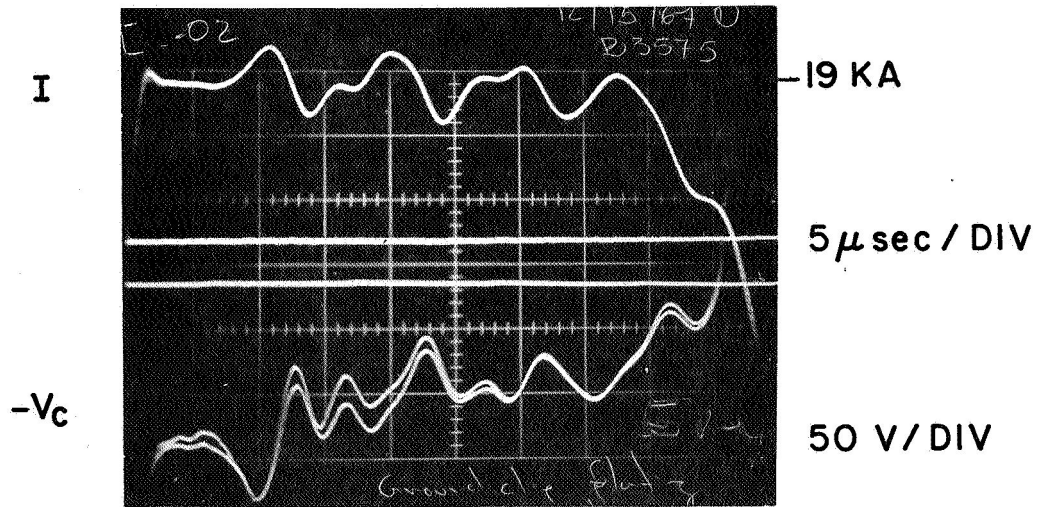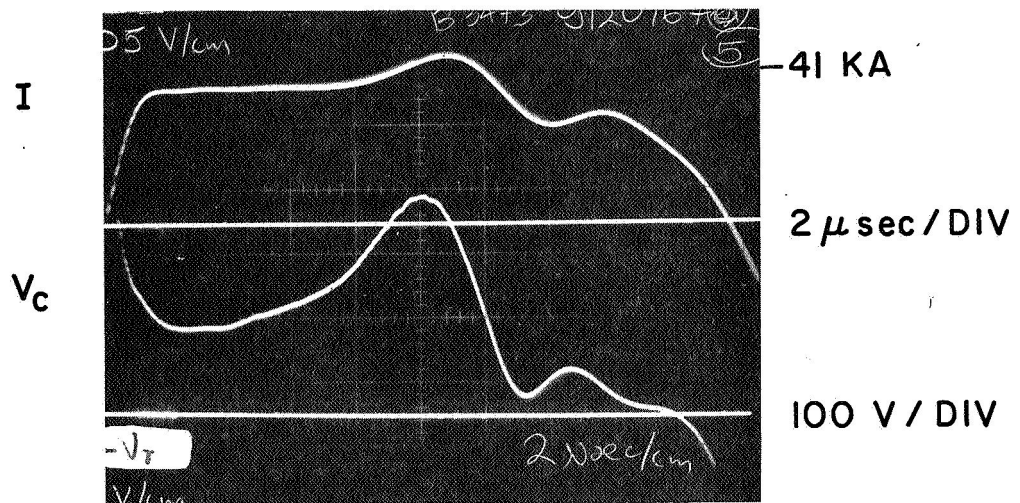
a) 20 KA × 40 μsec PULSE

b) 40 KA × 20 μsec PULSE
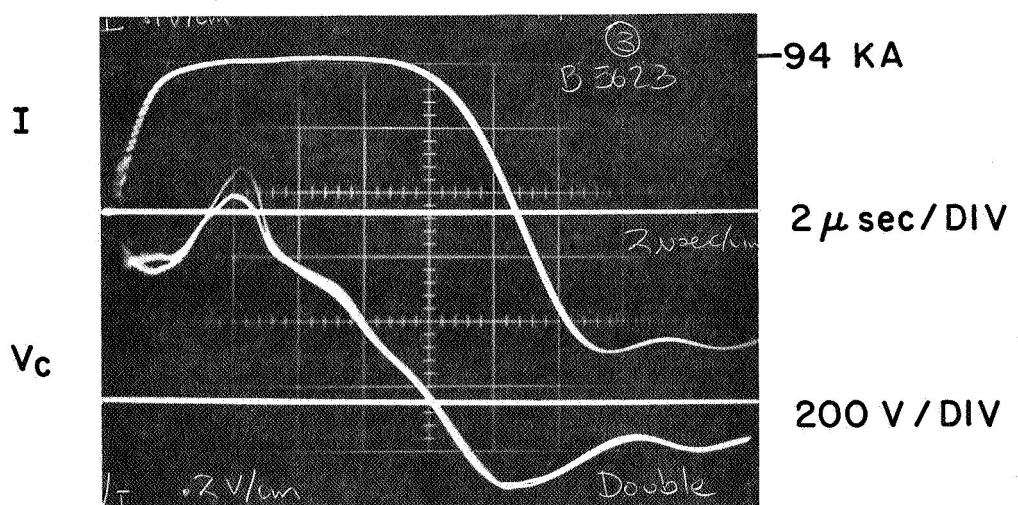
c) 100 KA × 10 μsec PULSE

DISCHARGE CURRENT I AND VOLTAGE V_C
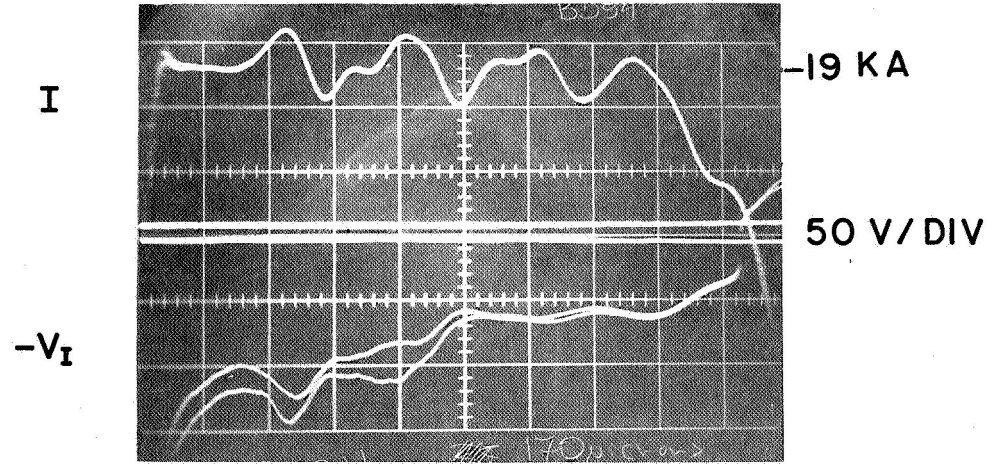
FIGURE 48
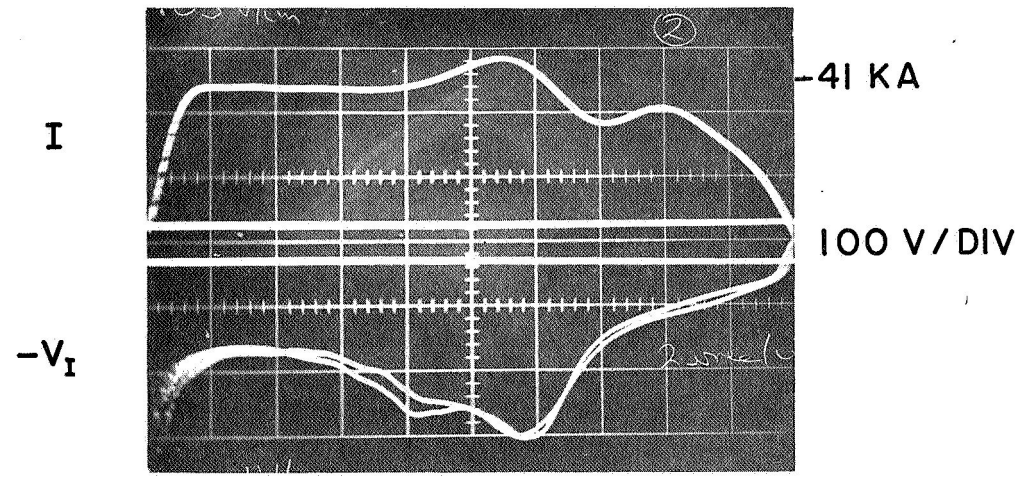
a) 20 KA × 40 μsec PULSE
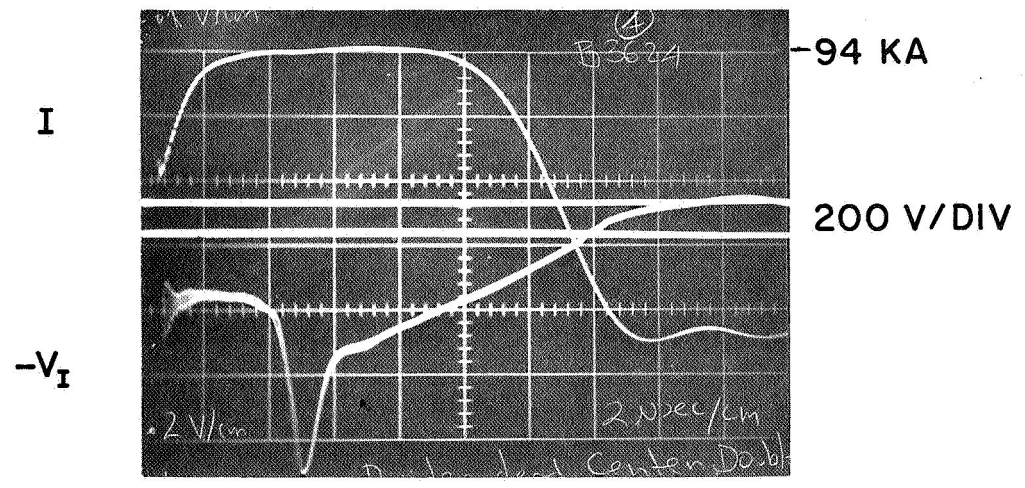
b) 40 KA × 20 μ sec PULSE

c) 100 KA × 10 μ sec PULSE

DISCHARGE CURRENT I AND INNER
DIVIDER VOLTAGE V_I

FIGURE 49

B 3588

İ   5 μ sec/DIV

V_I - V_C   50 V/DIV

a)   20 KA × 40 μ sec PULSE

B 3606

2İ   2 μ sec/DIV

V_I - V_C   100 V/DIV

b)   40 KA × 20 μ sec PULSE

B 3619

5İ   2 μ sec/DIV

V_I - V_C   200 V/DIV
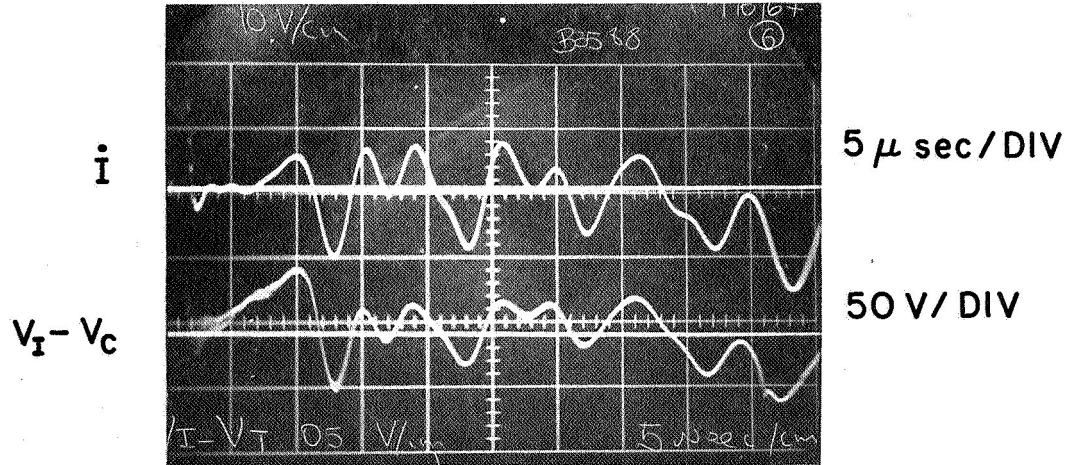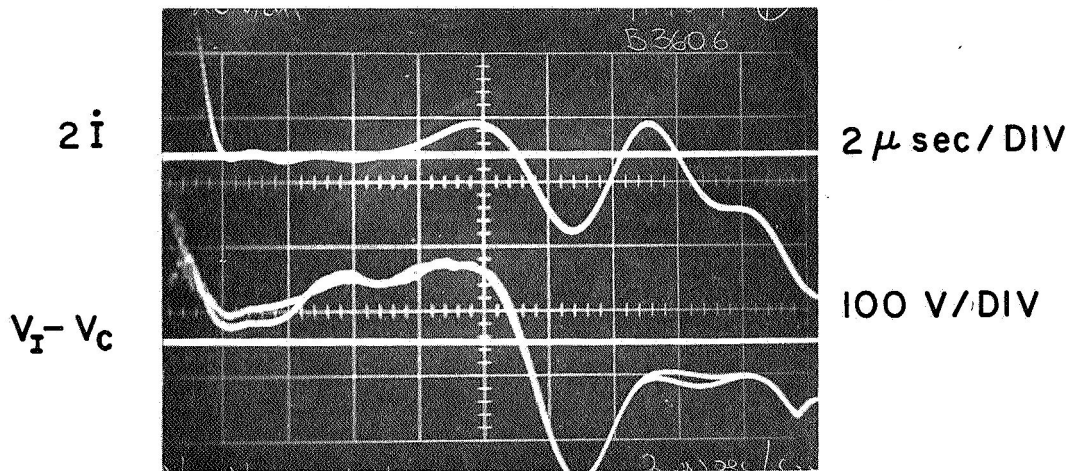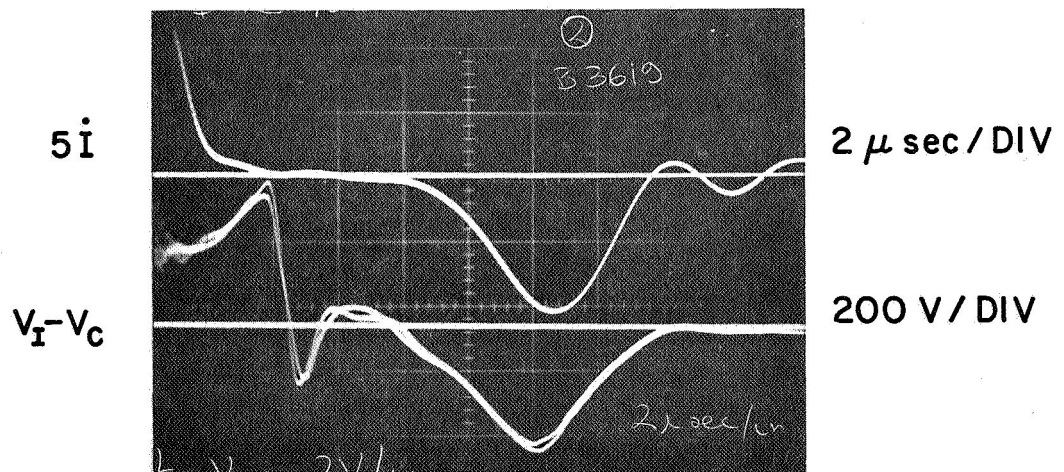
c)   100 KA × 10 μ sec PULSE

$\frac{dI}{dt}$ AND VOLTAGE ($V_I - V_C$)

FIGURE 50

the contour:

$$\oint E\ d\ell = V_C - V_I = -\frac{\partial \phi}{\partial t}$$

where $\frac{d\phi}{\partial t}$ may be provided either by $\frac{dI}{dt}$ or by a progression
of the current distribution within the chamber. In Fig. 50a,
except for the first few microseconds, $(V_I - V_C)$ closely fol-
lows the derivative of the current, $\frac{dI}{dt}$, thus suggesting that
there is little propagation of the current density patterns
within the discharge chamber at this low current value. This
interpretation is confirmed by the enclosed current profiles
reduced from magnetic probe records (Fig. 51) which show that
despite fluctuations of total current, I, in the pulse, the
radial distribution of the current within the chamber remains
essentially unchanged, with 75% of the current flowing between
the outer wall and half radius. In Fig. 50b, for the 40 KA
pulse, the voltage difference $(V_I - V_C)$ shows a steady increase
over the period from 2 to 10 μsec although $\frac{dI}{dt}$ is essentially
zero then. After 10 μsec the voltage $(V_I - V_C)$ follows the
current derivative more closely. This suggests an initial
period of current propagation, which is confirmed by the pro-
files of enclosed current, obtained by magnetic probing
(Fig. 52). These current profiles progressively move inward
until a distribution is reached that remains essentially un-
changed until the end of the pulse despite current fluctuations
in the latter portion of the pulse.

The $(V_I - V_C)$ record of the 100 KA x 10 μsec pulse
(Fig. 50c) increases from 250 volts to about 400 volts during
the period from 1 to 4 μsec, suggesting a rapidly propagating
current zone. This rapid progression is again supported by
the corresponding plot of enclosed current contours, obtained
by magnetic probing (Fig. 53). The rather abrupt drop of
$(V_I - V_C)$ from about 4 to 4.5 μsec could be related to the
deceleration of the current sheet during the terminal phase
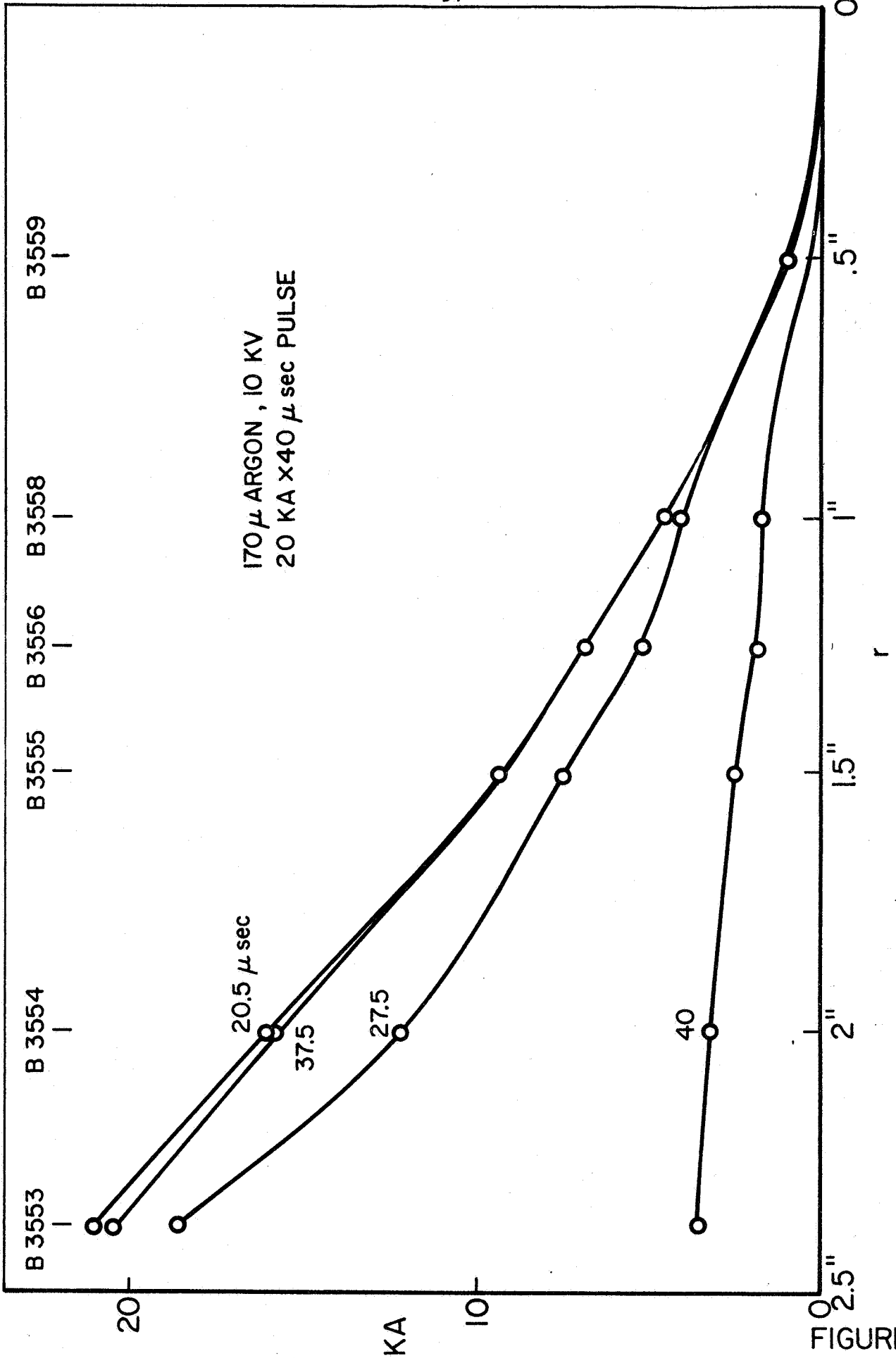
FIGURE 51

RADIAL PROFILES OF ENCLOSED CURRENT

170 μ ARGON , 10 KV
20 KA ×40 μ sec PULSE
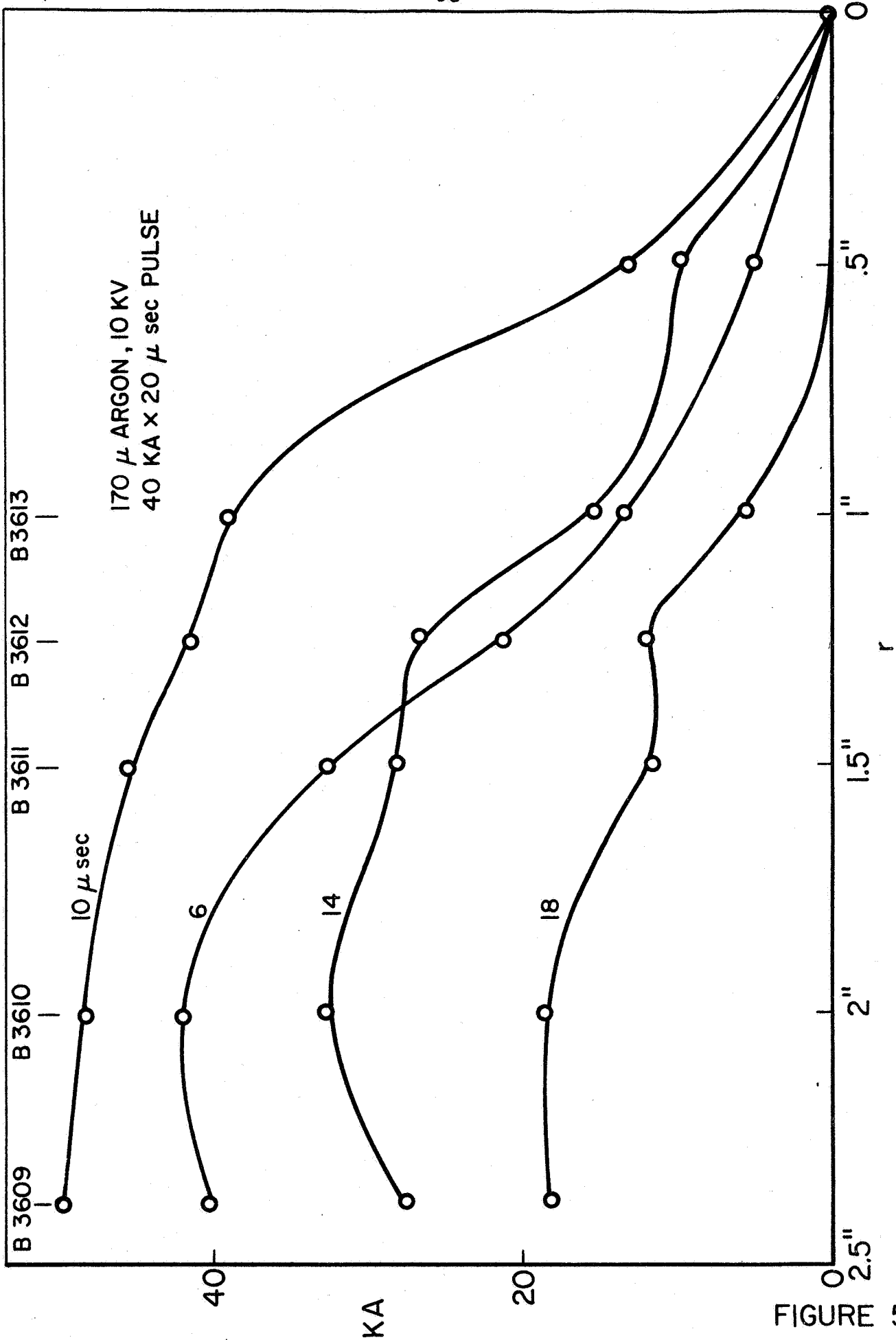
RADIAL PROFILES OF ENCLOSED CURRENT
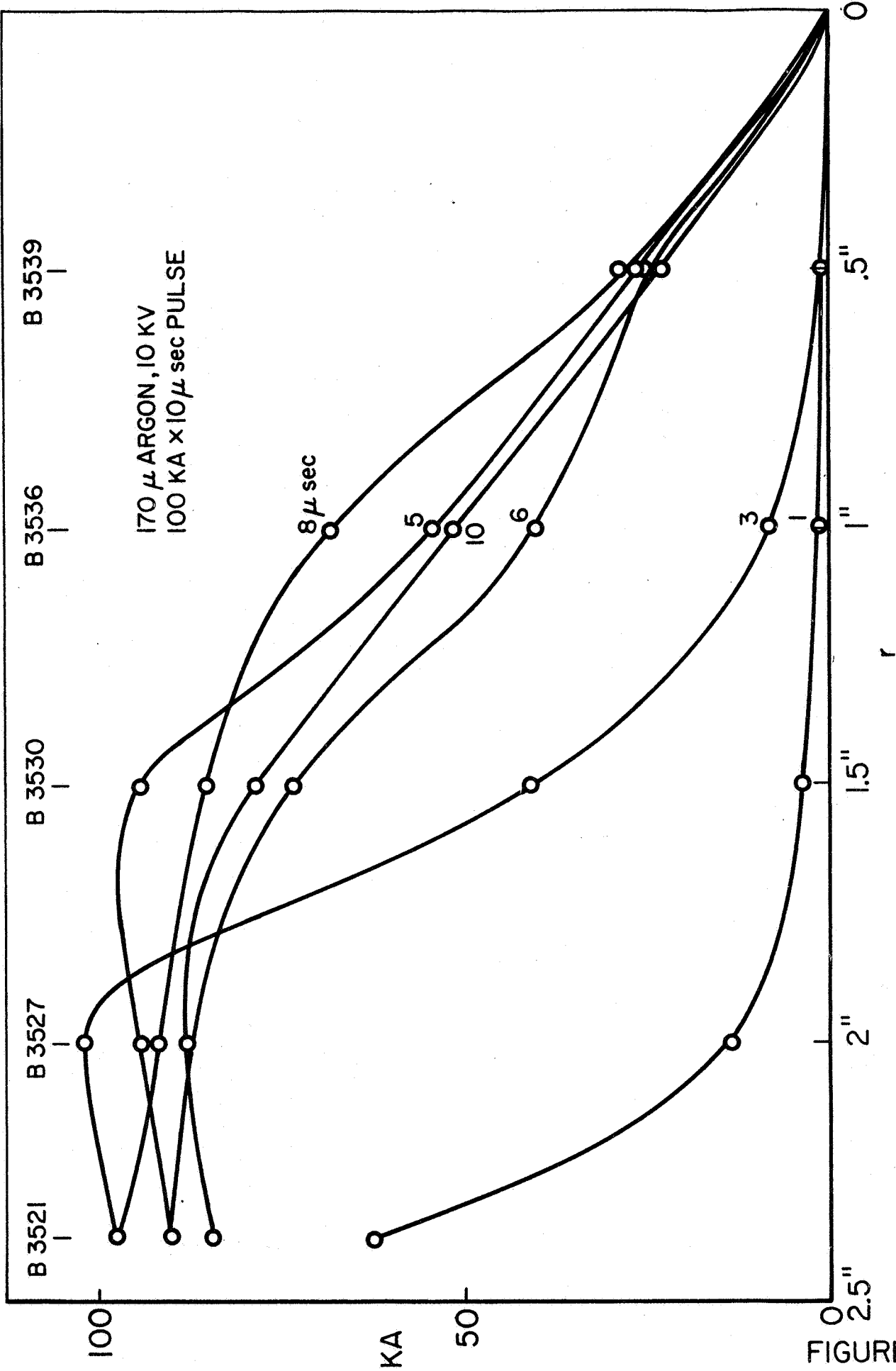
FIGURE 52

RADIAL PROFILES OF ENCLOSED CURRENT

FIGURE 53

of its inward radial motion, as also displayed in the contours of Fig. 53. After 8 μsec $(V_I - V_C)$ follows $\frac{dI}{dt}$ closely, just as it does for the other current pulses. Figure 53 confirms that the current distribution remains stationary during this phase.

APPENDIX I.   ELECTROMAGNETIC STRUCTURE
OF A DYNAMIC PLASMA DISCHARGE
(Turchi)

An experimental investigation of a dynamic current
sheet in a plasma was undertaken to determine its structure
and the physical processes involved in its ability to accel-
erate an ionized gas to high velocity. The experiments con-
ducted were electrical in nature and consisted of simultaneous
measurement of the local magnetic and electric fields present
in the ionized gas as a function of time for various positions.
The measurements were then used to calculate the local current
density and to infer some of the physics involved.

The particular device in which experiments were per-
formed consists of an 8-inch diameter discharge chamber with
a 2-inch interelectrode gap. The chamber was filled initially
with argon at 100 μ pressure and then connected, by a gas-
triggered switch, to a distributed line of capacitors charged
to 10 kilovolts.[37]   The current waveform used in these ex-
periments was a backwards sawtooth pulse, which rose to 415,000
amperes in 0.9 μsec, then linearly decreased for 2 μsec, pass-
ing through zero after about 4 μsec. This provided a signal
from the magnetic probe which was very sharp and intense, and
was reproducible to 50 nanoseconds.

The time rate of change of the magnetic field at each
point was measured with a magnetic probe of the usual design.
These records were then graphically integrated to obtain the
local magnetic field. The probe employed consisted of a 1 mm
diameter, 4-turn coil encased in epoxy and supported in a
3/16-inch diameter nylon tube. The overall tip diameter was
about 3 mm at the coil position. The nylon support was curved
near the coil end so that any disturbance due to the support
would be downstream of the measuring position.

The electric field at each position was obtained

by the use of a coaxial double-tip electric probe.[42] The axial electric field was measured using a probe encased in a 3/16-inch diameter Pyrex tube. The diameter of the outer conductor at the measuring surface was 2.5 mm and the electrode separation was 2 mm. In the case of the radial electric field measurement, the probe was encased in a nylon tube, since the probe extended through the center of the discharge chamber and, if made of Pyrex, would shatter when the plasma pinched at the center. The radial electric probe had an electrode separation of 1.85 mm and the diameter of the outer electrode was 2.5 mm.

The largest error involved in the probe work performed in these experiments results from the design criteria of the radial electric probe. To obtain fine spatial resolution, we would want the electrode separation to be as small as possible. However, to insure that the signal level would be reasonably above that of the electromagnetic noise, the electrode separation and electrode surface areas must be large enough to draw a current from the plasma sufficient to drive the probe circuit. When these constraints were resolved along with fabrication problems, the resulting probe allowed a spatial (or temporal) uncertainty of about 25%.

The electric and magnetic fields at the midplane of the discharge chamber were measured as functions of time for radial positions from r = 3-1/2" to r = 1-1/2". Plots of $\dot{B}$, radial electric field, E_r , and axial electric field, E_z , as functions of time at a typical radial position (r = 2-1/2") are shown in Fig. 54a,b,c. These plots represent measurements taken in several experimental runs. The reproducibility of the measurements was quite good, with less than 5% deviation between records (after adjustments were made in the time scales to take account of the 50 nanosecond scatter in the arrival times of essential identical profiles).

We obtained the velocity of the current sheet profile
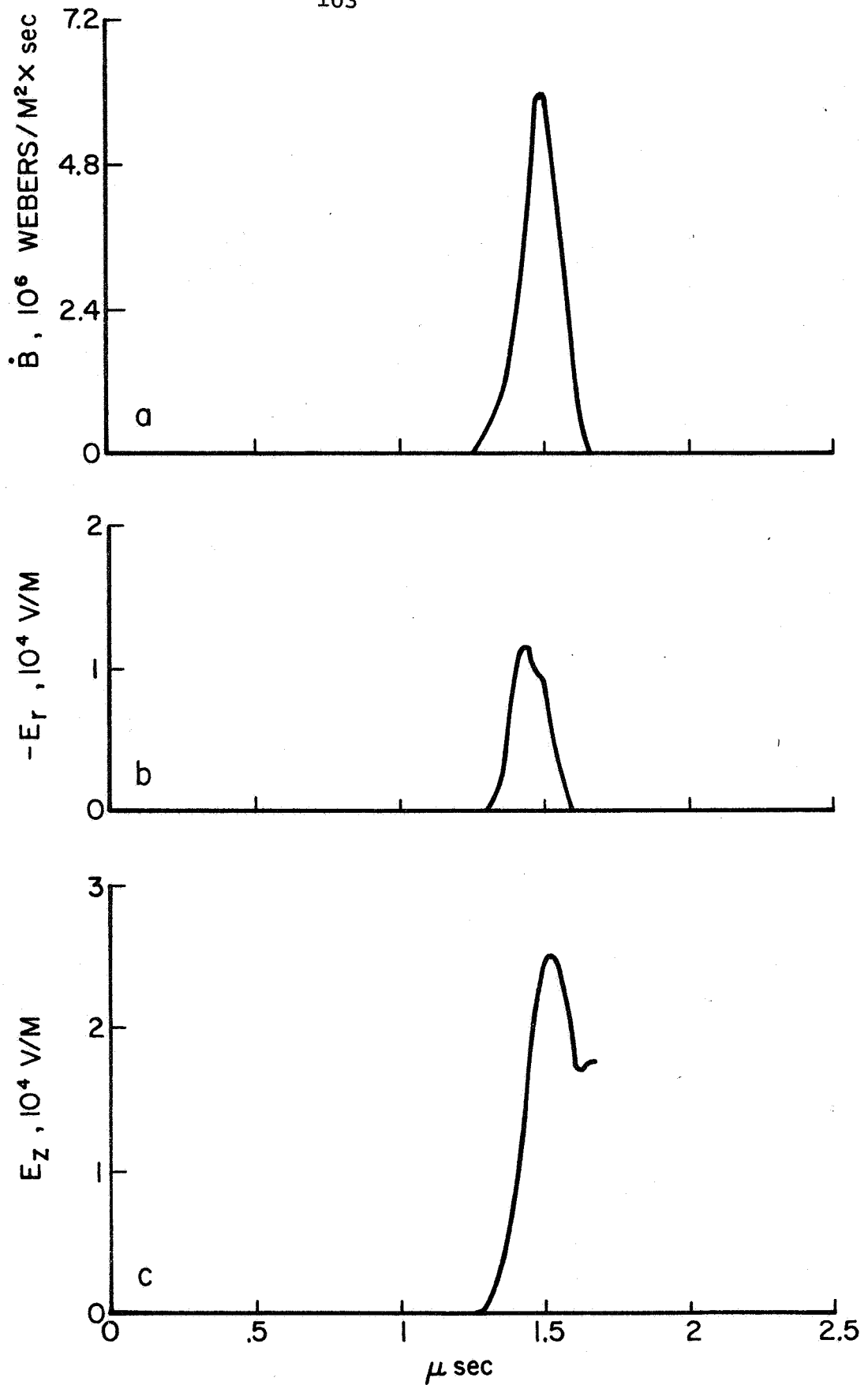
TYPICAL FIELD DATA AT r = 2.5"

FIGURE 54

from the arrival times of the peak of the $\dot{B}$ profile at various
radial positions by successive linear approximations. The
sheet velocity was about 36,000 meters/second and was constant
to with 20% over the range of interest (its variation, however,
was considered in our calculations). It has been assumed that
the velocity obtained from the trajectory of the $\dot{B}$ peak is
representative of the velocity of the other profiles that prop-
agate inward with the $\dot{B}$ peak, and that this phase velocity is
approximately constant throughout a profile (this is true to
within about 7%). We were then able to transform from our
plots of electrical measurements as functions of time for var-
ious positions, to plots of these quantities as functions of
radial position at various times (see Figs. 55a,b).

The magnetic field, obtained from the $\dot{B}$ vs. t plots,
is shown for various times in Fig. 56a. With our knowledge
of the magnetic field at a point, we may compute the fraction
of the total current through the discharge which passes in-
terior to that point. Then, by assuming that the rate of
change of enclosed current is proportional to the enclosed
current, (a first order approximation to the small correction
term required) we may calculate that part of the $\dot{B}$ signal
which is due to changes in the total current level. Sub-
tracting this from the measured $\dot{B}$ signal, we obtain the con-
tribution to $\dot{B}$ by the convection of a current density profile
past the point of measurement. From this, we determine the
axial current density, j_z , at that point. Plots of j_z versus
radial position for various times are shown in Fig. 56b.

Before launching into a detailed discussion of the
implications of our measurements, we should consider the
theoretical bases for such development. There are essentially
two approaches to the problem at hand: 1) orbit theory, and
2) magnetogasdynamics (MGD) coupled with the Boltzmann equation.
The first of these is inapplicable to our situation for two
reasons: a) the electron cyclotron radius is much larger than
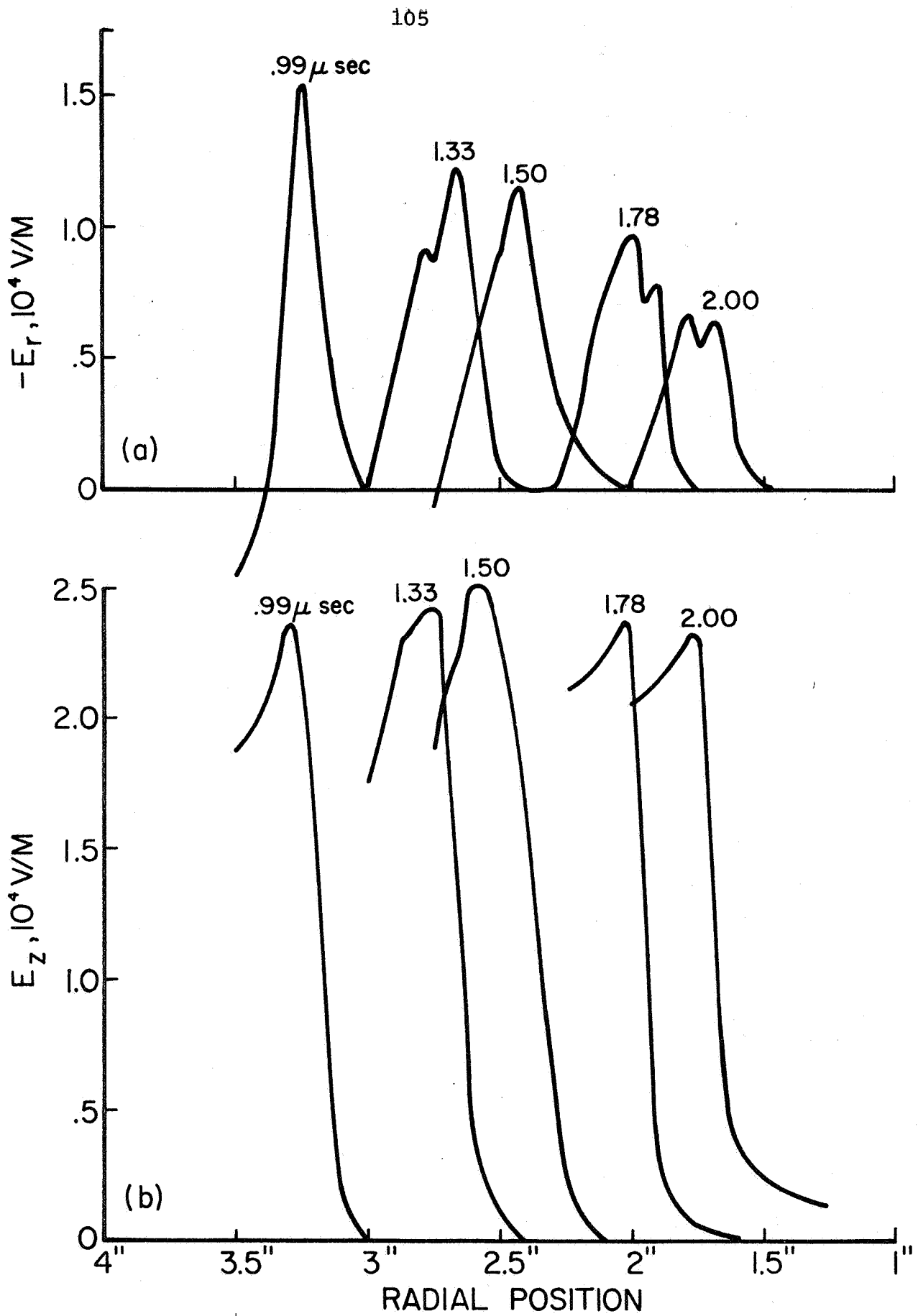
ELECTRIC FIELD PROFILES

T2295- T2399

FIGURE 55
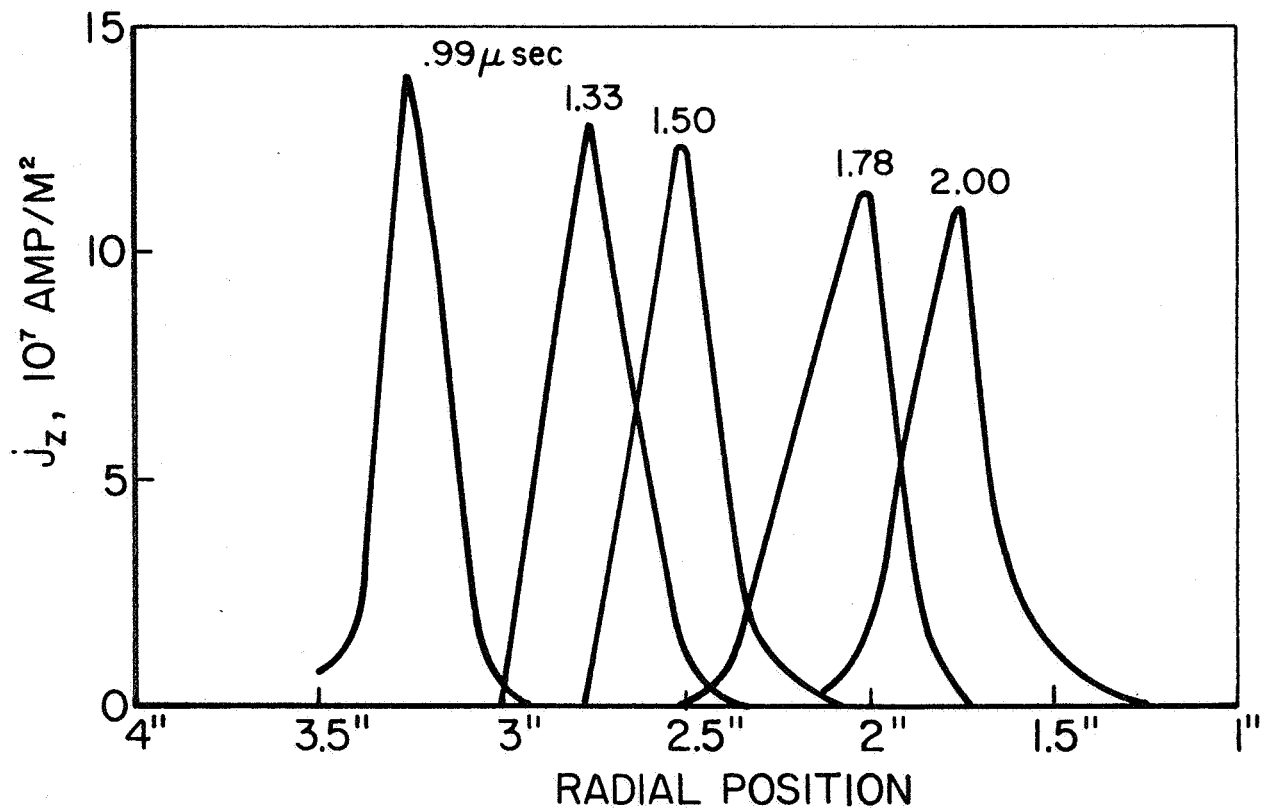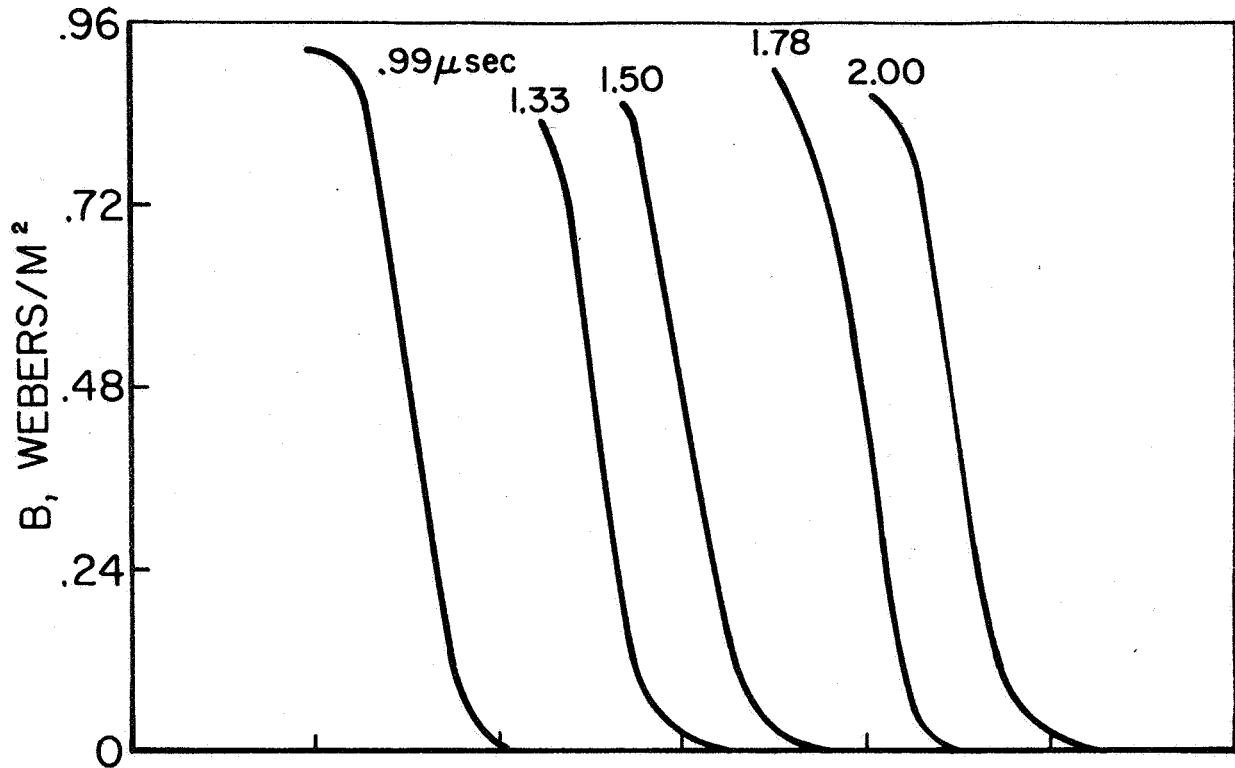
PROFILES OF MAGNETIC FIELD
AND AXIAL CURRENT DENSITY

T2295-T2399

FIGURE 56

the Debye length; therefore, the electrons are collisionally
coupled to the electron fluid throughout their "orbit" and
it is best to avoid the naive picture of electrons constrained
by the magnetic field lines. b) The ion gyroradius is com-
patible to the dimensions of the current sheet and therefore
the magnetic field changes significantly over the gyroradius.

Magnetogasdynamics suffers from a somewhat subtler
problem in our situation. Although the electron fluid is
well-described, the ion fluid is subject to anisotropies in
velocity distribution since the magnetic field may change
significantly over a mean free path. This results in an in-
correct description of the force on the ion fluid. (For in-
stance, if the magnetic field gradient is high enough, the
ions can develop a drift velocity, even if the mean velocity
and thus the Lorentz force density is initially zero.)

Both of the above theoretical limitations in our work
are essentially due to the fact that the ion gyroradius is
comparable to current sheet dimensions. Indeed, it may well
be that the dimensions of the current sheet and, thus, the
current conduction process are determined by the nonlinear
ion trajectory in the electromagnetic fields. If this is the
case, the approximations accepted when utilizing the above
theories preclude a proper description of the physics of the
current sheet.

In order to proceed toward some understanding of the
physical processes involved in the dynamic plasma discharge,
we shall use the magnetogasdynamic formulation, accepting all
its implicit assumptions (of particular significance, is the
assumption of an isotropic ion velocity distribution over the
dimensions of the current sheet). We start with a generalized
Ohm's law for the plasma: [A-9]

$$\vec{j} = \sigma_o \left\{ \vec{E}^* + \frac{\vec{\nabla} P_e}{N_e e} - \frac{\vec{j} \times \vec{B}}{N_e e} \right\} \tag{1}$$

where $\sigma_O = \dfrac{N_e e^2}{m_e \nu_{ei}}$ = scalar conductivity (2)

ν_{ei} = electron-ion collision frequency (for momentum transport)

$\vec{E}^*$ = electric field measured by an observer moving with the mass-averaged velocity of the flow = $\vec{E} + \vec{q} \times \vec{B}$

$\vec{E}$ = electric field measured in the lab

$\vec{q}$ = mass-averaged velocity of the flow relative to the lab

P_e = electron pressure

N_e = electron number density

We have further assumed that the ionization level is sufficiently high that coulomb collisions dominate over all other types. We may solve this equation for the components of the current density: $(\vec{j} = j_r \hat{r} + j_z \hat{k})$

$$j_r = \frac{\sigma_O}{1 + \Omega^2} \left[(E_r^* + \Omega E_z^*) + \frac{1}{N_e e} \left(\frac{\partial P_e}{\partial r} + \Omega \frac{\partial P_e}{\partial z} \right) \right] \quad (3)$$

$$j_z = \frac{\sigma_O}{1 + \Omega^2} \left[(E_z^* - \Omega E_r^*) + \frac{1}{N_e e} \left(\frac{\partial P_e}{\partial z} - \Omega \frac{\partial P_e}{\partial r} \right) \right] \quad (4)$$

where $\Omega = \dfrac{\omega}{\nu_{ei}} = \dfrac{eB}{m_e \nu_{ei}}$ = Hall parameter for electrons. We further simplify these equations by neglecting the electron pressure gradient terms (it can be shown that if the "magnetic pressure" is much greater than the electron pressure, the radial gradient term may be neglected. We drop the axial pressure gradient term in that we expect it to be of importance only near the electrodes).

From experiment, we have that, in the midplane, j_r is much smaller than j_z. Then, to within experimental accuracy, we may set j_r equal to zero. This is a very important step

in that it prescribes a particular structure for the current sheet, and allows us to simplify our equations considerably. We have now:

$$\Omega = -\frac{E_r^*}{E_z^*} \tag{5}$$

$$j_z = \sigma_o E_z^* \tag{6}$$

and

$$N_e = -\frac{j_z B}{eE_r^*} \tag{7}$$

Thus, if we can relate the electric fields seen in the moving coordinate system to those measured in the laboratory, we may learn a great deal about the current sheet. Unfortunately, this cannot be done by any straightforward procedure (using only electromagnetic measurements). The problem is that the electric fields seen by the moving plasma depend on the mass-averaged velocity of the plasma which in turn depends on the electric fields seen in the moving system. This situation reflects the inherent nonlinearity of the physical phenomena under study. We shall attempt by way of various assumptions to determine limiting situations such as minimum axial ion velocity, minimum electron Hall parameter, etc.

We may manipulate equations (5) to (7) to obtain the very interesting result that:

$$v_e = \frac{E_r}{B} \tag{8}$$

that is, the electrons travel with an axial velocity equal to the so-called "drift velocity" in crossed electric and magnetic fields. We note that this result is independent of the axial ion velocity as long as a very high degree of single ionization prevails ($q_z \approx v_i$ and $z_i \approx 1$). From our profiles of E_r , we see that this implies that the electron contribution to the axial current density drops off sharply near the current density maximum.

Consider now the situation in which a collisionless ion is accelerated by the axial electric field, but constrained to zero radial motion. It may be shown then that, if the sheet velocity is less than the "drift velocity" E_z/B, the axial velocity achieved by the ion will be less than if we allowed it to move inward with the current sheet. Thus, the minimum axial velocity of a collisionless ion is:

$$v_{imin} = \frac{e}{m_i} \int E_z \, dt \qquad (9)$$

A plot of v_{imin} vs. t is shown in Fig. 57a for a typical radial position (r = 2-1/2"). We may now obtain the relative ion and electron (axial) current densities, by further manipulation of our equations:

$$\frac{j_i}{j_e} = \frac{v_i}{v_e} = \frac{v_i B}{E_r} \qquad (10)$$

The minimum value of j_i/j_e occurs for $v_i = v_{imin}$, so

$$\left.\frac{j_i}{j_e}\right)_{min} = \frac{\frac{eB}{m_i} \int_o^t E_z \, dt}{E_r(t)} \qquad (11)$$

This is shown as a function of time in Fig. 57b, again for r = 2-1/2". Note that just after the current density maximum the <u>minimum</u> ion current density becomes comparable to the electron current density. Unfortunately, an attempt to find the maximum axial ion velocity, in a similarly simple way, fails because the nonlinearity of the problem returns. This situation results when we allow the ion to move radially inward with a velocity comparable to that of the current sheet. (It should again be noted that the term 'minimum' used here assumes ion-neutral collisions are negligible.)

From the same formulation, we may obtain the minimum

TOTAL AXIAL CURRENT DENSITY PEAKS AT $t = 1.5 \ \mu$ sec, $r = 2.5''$
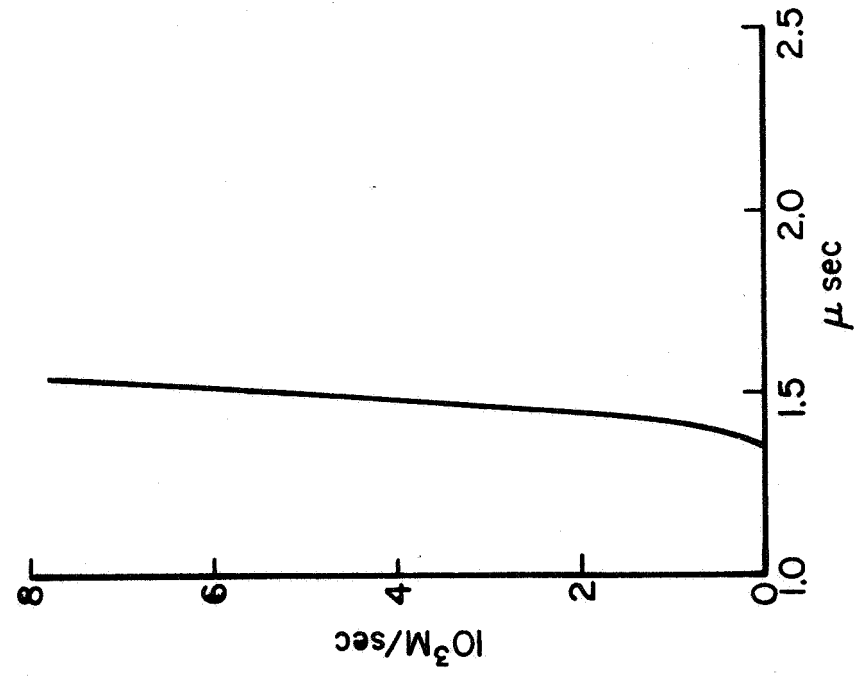
a) MINIMUM ION VELOCITY
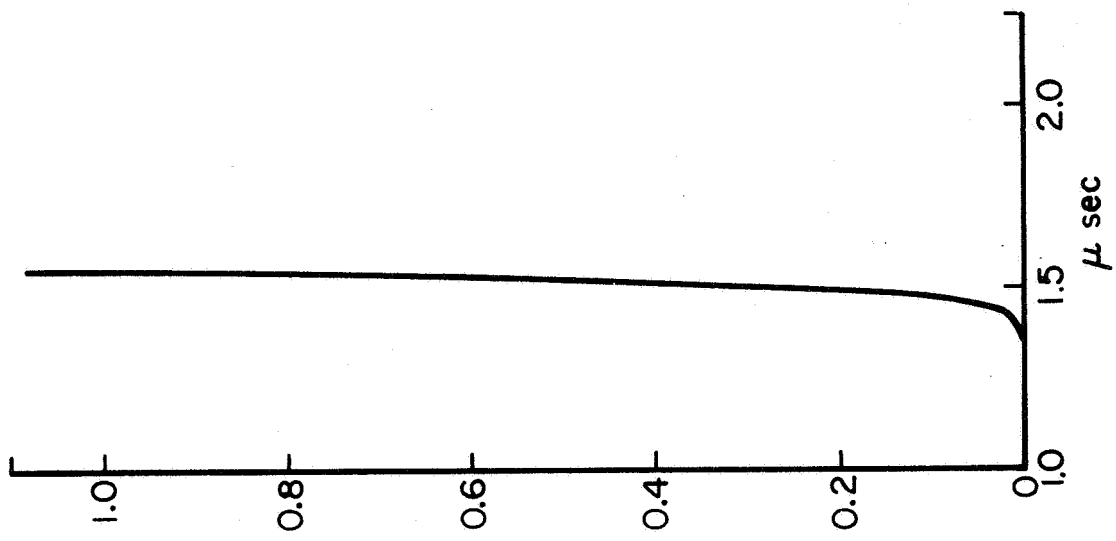
b) MINIMUM RATIO OF ION AND ELECTRON AXIAL CURRENT DENSITIES
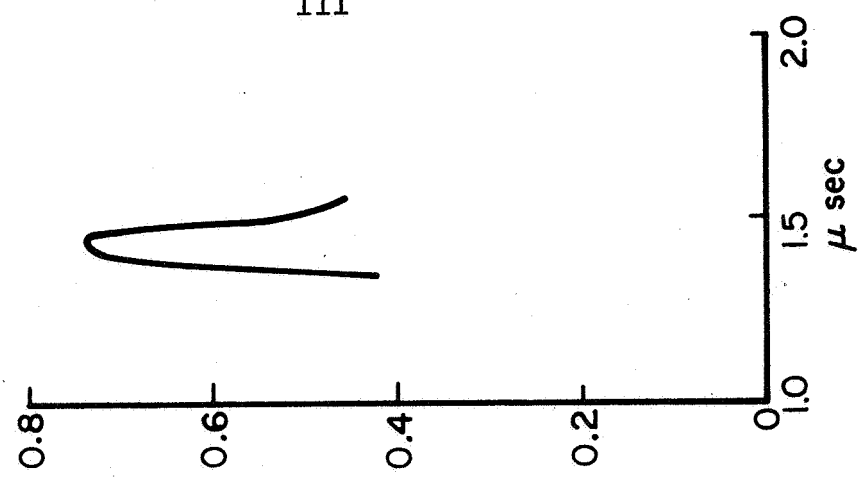
c) MINIMUM ELECTRON HALL PARAMETER

FIGURE 57

electron Hall parameter, shown as a function of time in Fig. 57c (r = 2-1/2"). It should be noted that even if the electron Hall parameter is not greater than unity, the electrons will still travel axially with the "drift velocity," E_r/B. This results from the inherent structure implied by j_r = 0. Observe that the axial electron velocity obtained is independent of the ion motion. (In fact, the axial electron velocity, as seen from a coordinate system moving with the ions, is formally the same, E_r*/B.)

Let us now attempt to calculate the radial ion velocity. Consider, first, a collisionless ion constrained to zero axial motion. We may obtain its radial velocity simply from the radial electric field measured in the laboratory. We note that this will be the minimum radial velocity of a collisionless ion, since axial motion in the expected direction would interact with the magnetic field also to provide inward velocity (again, this is a linear approach in that we do not allow the ion to turn appreciably in the magnetic field). A plot of the radial velocity of such an ion is shown as a function of radial position in the current sheet for a typical time (t = 1.50 µsec, corresponding to r = 2-1/2") in Fig. 58a. Note that the final velocity achieved by the ion is about half the sheet velocity.

From our previous calculation of the minimum axial ion velocity, we may compute the effective radial electric field due to motion in the magnetic field, $v_{imin}B$; this is plotted, along with E_r , in Fig. 58b. Note that in the latter portion of the current sheet, the contribution to the radial ion acceleration by the Lorentz force becomes comparable to that due to the radial electric field. A further substantiation of significant axial ion motion may be obtained, from equation (7), observing that, as the radial electric field measured in the laboratory drops off after the current density maximum, the induced field v_iB must be important in order to maintain a

b) RADIAL ELECTRIC FIELDS

MINIMUM INDUCED FIELD ———
MEASURED RADIAL FIELD - - - -

10^3 V/M

μ sec

CURRENT DENSITY PEAKS AT t = 1.5 μ sec, r = 2.5"
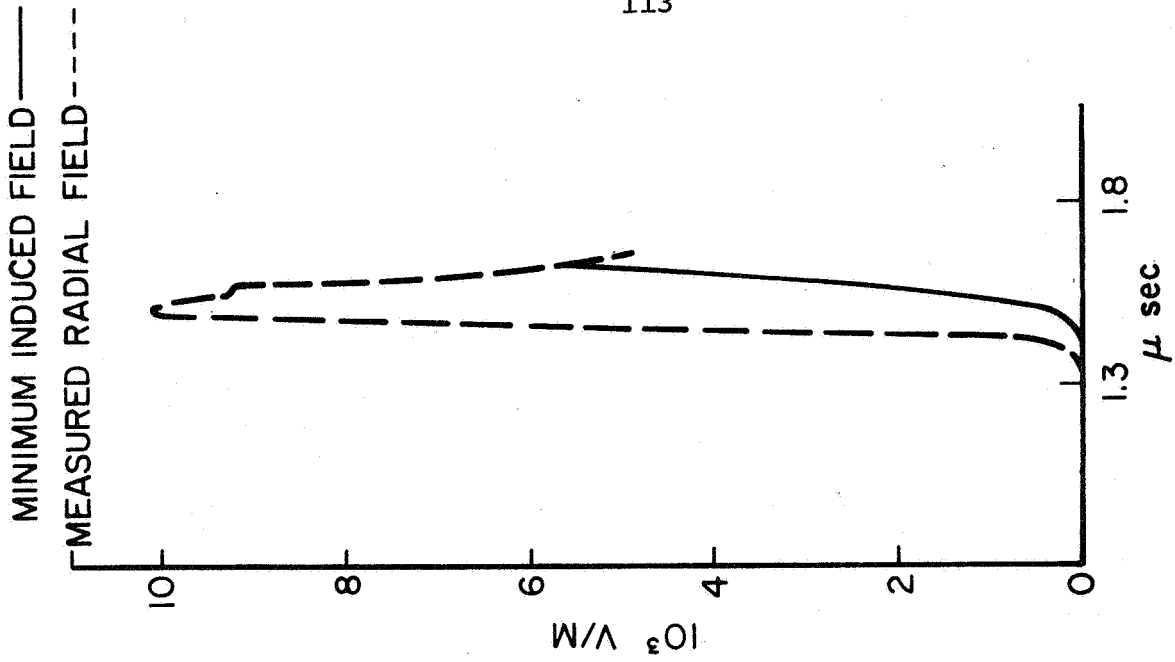
a) RADIAL ION VELOCITY

RADIAL POSITION

10^4 M/sec

FIGURE 58
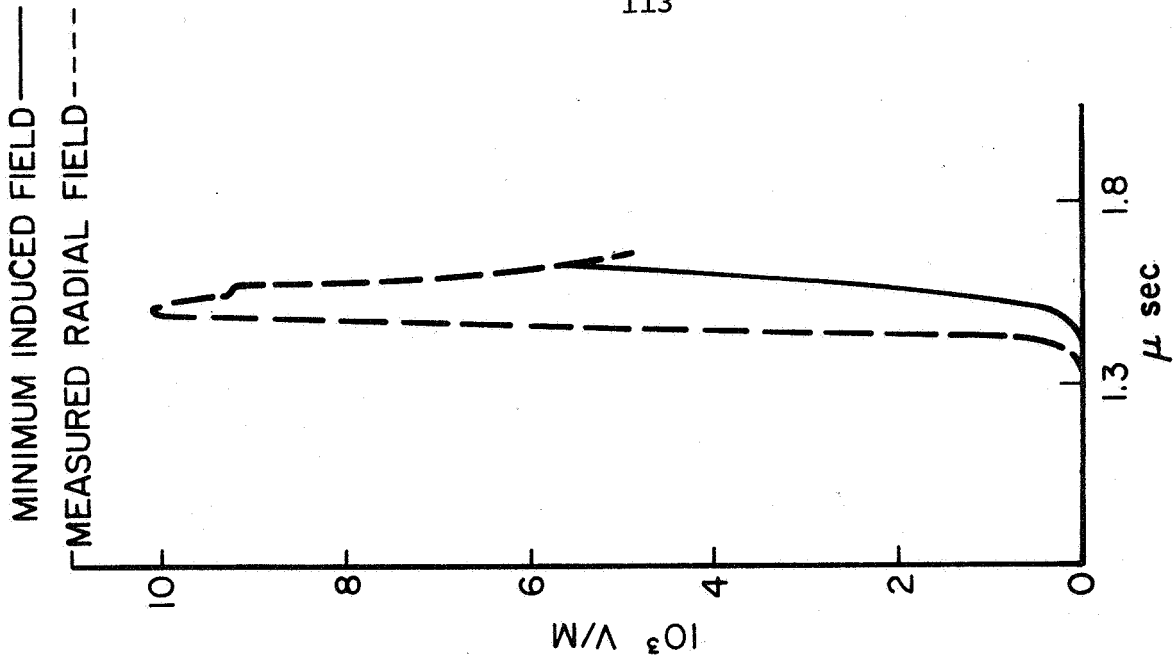
finite electron density (the axial ion velocity needed, however, is only on the order of 15% of the sheet velocity).

We shall now approach the problem through calculation of the radial ion velocity required to provide a significant induced electric field in the axial direction. We have from equation (6) that:

$$\sigma_o = \frac{j_z}{E_z^*} = \frac{j_z}{E_z + u_i B}$$

where we have assumed that $q_r \approx u_i$. Then, using Spitzer's formula for the resistivity of a fully ionized gas[A-10] (thereby continuing our assumption of a high-degree of ionization and further assuming that the plasma density and temperature allow such a formulation of the resistivity to be useful, $\ln \Lambda >> 1$, which is not really true in our case). We have:

$$\sigma_o = (2.55 \times 10^{-1}) \ T_e^{3/2} \ [\Omega - m]^{-1} \tag{12}$$

$$\text{with} \quad \ln \Lambda = 6$$

then

$$u_i = \frac{j_z}{\sigma_o B} - \frac{E_z}{B} \tag{13}$$

$$= \frac{(3.92 \times 10') j_z}{T_e^{3/2} B} - \frac{E_z}{B}$$

We may now calculate the radial ion velocity in the current sheet for various values of the electron temperature. From previous experience in these regimes,[2,50] we expect the electron temperature to range from about one to six electron volts. In performing our calculations, we find the discouraging result that, even for an electron temperature as low as 1 ev, in the early portions of the discharge, the ion velocity

(even worse, the mass-averaged velocity of the ionized gas) in the radial direction is greater than the current sheet velocity! Over the range of electron temperatures mentioned, the radial ion velocity profile is seen to approximate closely the radial drift velocity, $-E_z/B$, see Fig. 59. It is only in the latter portion of the discharge that we regain some confidence in the usefulness of our calculation. This region at best begins when the computed ion velocity equals the sheet velocity (t = $\sim$ 1.5 μsec). In previous portions of the discharge, we may attribute the failure of this formulation to a lower scalar conductivity, due perhaps to the transition from a neutral to a fully ionized gas. If we assume that the electron temperature rises to the range of a few electron volts by about t = 1.5 μsec, then we see that the mass-averaged radial flow velocity peaks at the sheet velocity midway through the current sheet and then drops off to about half the sheet velocity in the latter portion of the discharge.

In summary, then, we have inferred the following physical structure from our electromagnetic measurements:

    a)   The electron contribution to the current density is most significant in the early part of the current sheet.

    b)   In the latter part of the current sheet, the current density may be carried predominantly by the ions.

    c)   The ion radial acceleration is primarily due to the radial electric field, although, in the latter part of the discharge, Lorentz forces are significant.

    d)   The early portion of the discharge, is seen to be a region of transition from a weakly ionized gas to a fully ionized plasma.

CURRENT DENSITY PEAKS AT $t = 1.5\ \mu sec$, $r = 2.5"$

RADIAL DRIFT VELOCITY $-\dfrac{E_z}{B}$

MASS AVERAGED VELOCITY FOR $T_e = 1\ ev$

SHEET VELOCITY

VELOCITY OF A COLLISIONLESS ION DUE TO RADIAL ELECTRIC FIELD

μ sec
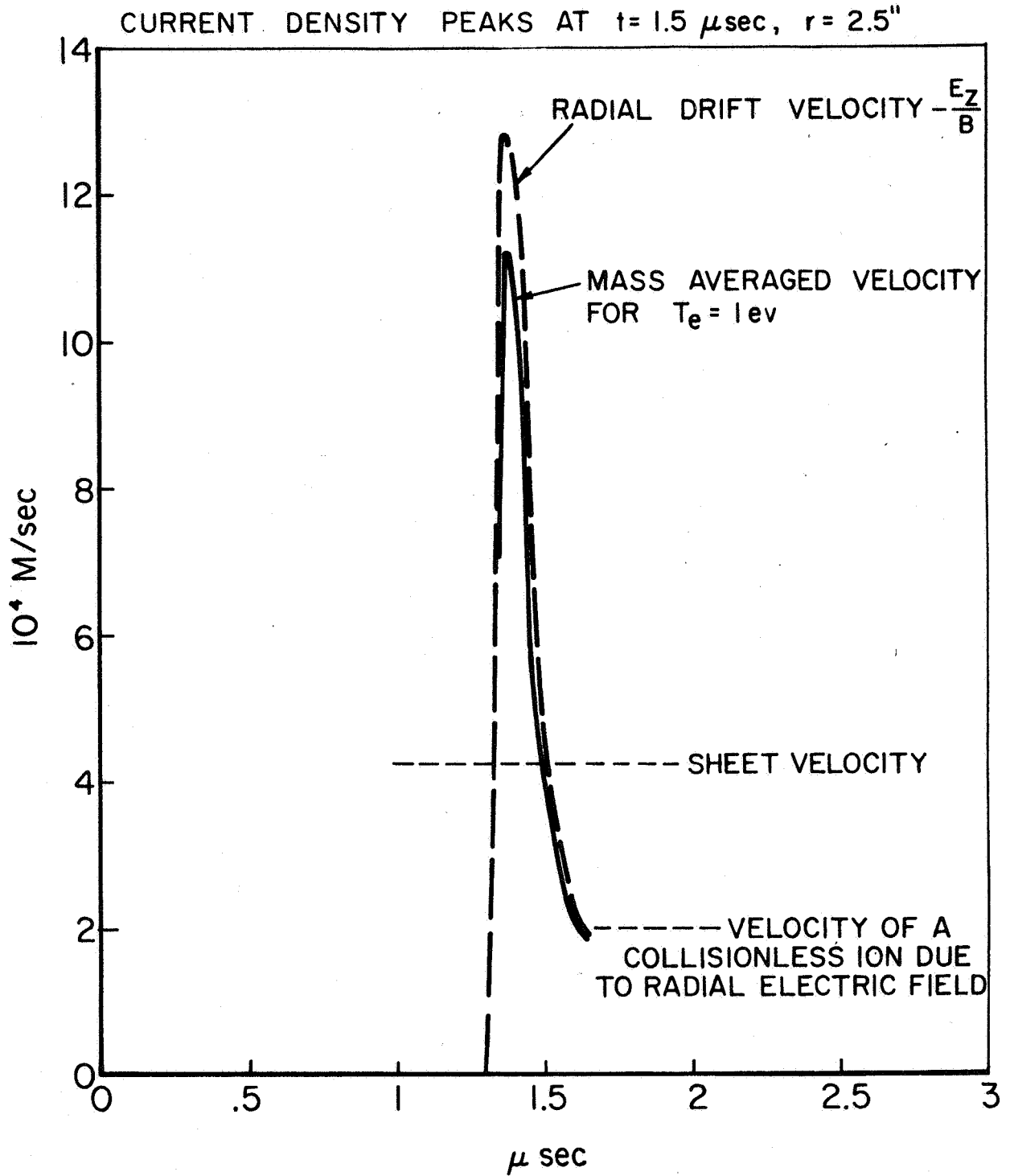
COMPARISON OF VARIOUS RADIAL VELOCITIES

FIGURE 59

e) The mass-averaged radial flow ve-
locity peaks at about the sheet velocity mid-
way through the current sheet and then falls
off to about half the sheet velocity in later
portions of the discharge.

Our physical picture of the dynamic plasma discharge,
thus, has two aspects. The first is that of an ionizing,
electromagnetic stress wave propagating into a weakly ionized
gas. The wave creates ion-electron pairs, which it then
separates, providing axial current and continuing the propa-
gation of the fields. In the process, the ionized gas is
accelerated inward. This acceleration results in the second
aspect of the dynamic discharge; while some of the plasma is
accelerated to the sheet velocity and is thereby carried along
with the wave, additional plasma follows the wave inward at a
lesser velocity. The discharge thus appears as a plasma blob,
created and accelerated by an electromagnetic stress wave, and
propagating inward with nonuniform velocity.

APPENDIX II.   DIAGNOSTIC TECHNIQUES FOR UNSTEADY
PLASMAS: ABSTRACTS AND REVIEWS OF
SELECTED PAPERS   (Turchi)

To insure continued contact with work done outside
our own laboratory, a collection of abstracts and brief re-
views of papers dealing with plasma diagnostics was compiled.
The papers described were selected on the bases of: 1) their
fundamental importance to plasma diagnostic work; 2) their
discussion of experimental techniques involving very short
time scales (~ 1 μsec), high speed flows ($\sim 10^4$ mis), and
nonequilibrium and/or nonuniform plasmas.

The sources from which these papers were selected
are:

1.   References in Huddlestone and Leonard, _Plasma
Diagnostic Techniques_, Academic Press, New York, (1965).

2.   "Bibliography on Magnetohydrodynamics, Plasma
Physics, and Controlled Thermonuclear Processes," compiled
by B. A. Spence, Avco-Everett Research Laboratory, AMP-36,
October, 1959.

3.   "Physics Abstracts," published by the Institution
of Electrical and Electronic Engineers. These monthly col-
lections of abstracts, from over 75 journals, were scanned
from January, 1964 through June, 1967.

4.   References from the Ph.D. theses of: F. Y. Sor-
rell, Jr.: "On the Generation of Shock Waves in an Inverse
Pinch," California Institute of Technology, Pasadena, Calif.,
(1966); R. L. Burton: "Structure of the Current Sheet in a
Pinch Discharge," Princeton University, Princeton, N. J.,
(1966); W. R. Ellis, Jr.: "An Investigation of Current Sheet
Structure in a Cylindrical Z-Pinch," Princeton University,
Princeton, N. J., (1967).

5.   Files of Professor Robert G. Jahn, Princeton
University, Princeton, N. J.

PROJECT REFERENCES

1. Proposed Studies of the Formation and Stability of an Electromagnetic Boundary in a Pinch, proposal for NASA Research Grant NsG-306-63, Princeton University, 5 March 1962.

2. Pulsed Electromagnetic Gas Acceleration, 1st Semi-Annual Progress Report for the period 1 July 1962 to 31 December 1962, _Princeton University Aeronautical Engineering Report No. 634_, January 1963.

3. "The Plasma Pinch as a Gas Accelerator," AIAA Electric Propulsion Conference, 11-13 March 1963, AIAA Preprint 63013.

4. Pulsed Electromagnetic Gas Acceleration, 2nd Semi-Annual Progress Report for the period 1 January 1963 to 30 June 1963, _Princeton University Aeronautical Engineering Report No. 634a_, June 1963.

5. Structure of a Large-Radius Pinch Discharge, _AIAA Journal 1_, 8, 1809-1814 (1963).

6. Gas-Triggered Inverse Pinch Switch, _Review of Scientific Instruments 34_, 12, 1439-1440 (1963).

7. A Gas-Triggered Inverse Pinch Switch, technical note, _Princeton University Aeronautical Engineering Report No. 660_, August, 1963.

8. "Pulsed Electromagnetic Gas Acceleration," 4th NASA Intercenter Conference on Plasma Physics, Washington, D. C., Paper No. II, 8, 2-4 December, 1963.

9. "Current Distributions in Large-Radius Pinch Discharges," AIAA Aerospace Sciences Meeting, 20-22 January 1964, AIAA Preprint No. 64-25.

10. Current Distributions in Large-Radius Pinch Discharges, _AIAA Bulletin 1_, 1, 12 (1964).

11. Current Distributions in Large-Radius Pinch Discharges, _AIAA Journal 2_, 10, 1749-1753 (1964).

12. Pulsed Electromagnetic Gas Acceleration, 3rd Semi-Annual Progress Report for the period 1 July 1963 to 31 December 1963, _Princeton University Aeronautical Engineering Report No. 634b_, December, 1963.

13. Pulsed Electromagnetic Gas Acceleration, renewal proposal for 15-months extension of NASA Research Grant NsG-306-63, Princeton University, 15 January 1964.

14. Pulsed Electromagnetic Gas Acceleration, 4th Semi-Annual Progress Report for the period 1 January 1964 to 30 June 1964, _Princeton University Aerospace and Mechanical Sciences Report No. 634c_, July, 1964.

PROJECT REFERENCES-contd

15. Gas-Triggered Pinch Discharge Switch, Princeton University Aerospace and Mechanical Sciences Technical Note No. 101, July, 1964.

16. Gas-Triggered Pinch Discharge Switch, Review of Scientific Instruments 36, 1, 101-102 (1965).

17. J. M. Corr, "Double Probe Studies in an 8" Pinch Discharge," M.S.E. thesis, Department of Aerospace and Mechanical Sciences, Princeton University, Princeton, New Jersey, 1964.

18. Exhaust of a Pinched Plasma From an Axial Orifice, AIAA Bulletin 1, 10, 570 (1964).

19. "Exhaust of a Pinched Plasma From an Axial Orifice," AIAA 2nd Aerospace Sciences Meeting, New York, New York, 25-27 January 1965, AIAA Paper No. 65-92.

20. Ejection of a Pinched Plasma From an Axial Orifice, AIAA Journal 3, 10, 1862-1866 (1965).

21. Pulsed Electromagnetic Gas Acceleration, 5th Semi-Annual Progress Report for the period 1 July 1964 to 31 December 1964, Princeton University Aerospace and Mechanical Sciences Report No. 634d, July, 1964.

22. On the Dynamic Efficiency of Pulsed Plasma Accelerators, AIAA Journal 3, 6, 1209-1210 (1965).

23. Linear Pinch Driven by a High-Current Pulse-Forming Network, AIAA Bulletin 2, 6, 309 (1965).

24. "Linear Pinch Driven by a High-Current Pulse-Forming Network," 2nd AIAA Annual Meeting, San Francisco, California, 26-29 July 1965, AIAA Paper No. 65-336.

25. E. S. Wright, "The Design and Development of Rogowski Coil Probes for Measurement of Current Density Distribution in a Plasma Pinch," M.S.E. thesis, Department of Aerospace and Mechanical Sciences, Princeton University, Princeton, New Jersey, 1965.

26. The Design and Development of Rogowski Coil Probes for Measurement of Current Density Distribution in a Plasma Pinch, Princeton University Aerospace and Mechanical Sciences Report No. 740, June, 1965.

27. Pulsed Electromagnetic Gas Acceleration, renewal proposal for 12-months extension of NASA Research Grant NsG-306-63, Princeton University, 7 June 1965.

28. Miniature Rogowski Coil Probes for Direct Measurement of Current Density Distribution in Transient Plasmas, Review of Scientific Instruments 36, 12, 1891-1892 (1965).

PROJECT REFERENCES-contd

29. Pulsed Electromagnetic Gas Acceleration, 6th Semi-Annual
     Progress Report for the period 1 January 1965 to 30 June
     1965, Princeton University Aerospace and Mechanical
     Sciences Report No. 634e, July, 1965.

30. G. A. Rowell, "Cylindrical Shock Model of the Plasma Pinch,"
     M.S.E. thesis, Department of Aerospace and Mechanical
     Sciences, Princeton University, Princeton, New Jersey, 1966.

31. Cylindrical Shock Model of the Plasma Pinch, Princeton
     University Aerospace and Mechanical Sciences Report No. 742,
     February, 1966.

32. Pulsed Electromagnetic Gas Acceleration, 7th Semi-Annual
     Progress Report for the period 1 July 1965 to 31 December
     1965, Princeton University Aerospace and Mechanical Sciences
     Report No. 634f, January, 1966.

33. Electric and Magnetic Field Distributions in a Propagating
     Current Sheet, AIAA Bulletin 3, 1, 35 (1966).

34. "Electric and Magnetic Field Distributions in a Propagating
     Current Sheet," AIAA 5th Electric Propulsion Conference,
     San Diego, California, 7-9 March 1966, AIAA Paper No. 66-200.

35. "Pulse-Forming Networks for Propulsion Research," paper pre-
     sented at the 7th Symposium on Engineering Aspects of Mag-
     netohydrodynamics, Princeton University, Princeton, New
     Jersey, March 30-April 1, 1966 (p. 10-11 of proceedings).

36. N. A. Black, "Dynamics of a Pinch Discharge Driven by a High
     Current Pulse-Forming Network," Ph.D. thesis, Department of
     Aerospace and Mechanical Sciences, Princeton University,
     Princeton, New Jersey, 1966.

37. Dynamics of a Pinch Discharge Driven by a High Current Pulse-
     Forming Network, Princeton University Aerospace and Mechanical
     Sciences Report No. 778, May, 1966.

38. "Pulsed Plasma Propulsion," paper presented at the 5th NASA
     Intercenter and Contractors Conference on Plasma Physics,
     Washington, D. C., 24-26 May 1966, p. 75-81, part V of
     proceedings.

39. Pulsed Electromagnetic Gas Acceleration, renewal proposal
     for 24-months extension of NASA Research Grant NsG-306-63,
     Princeton University, 25 May 1966.

40. A Large Dielectric Vacuum Facility, AIAA Journal 4, 6,
     1135 (1966).

41. R. L. Burton, "Structure of the Current Sheet in a Pinch
     Discharge," Ph.D. thesis, Department of Aerospace and
     Mechanical Sciences, Princeton University, Princeton, New
     Jersey, 1966.

PROJECT REFERENCES-contd

42. Structure of the Current Sheet in a Pinch Discharge, Princeton University Aerospace and Mechanical Sciences Report No. 783, September, 1966.

43. Pulsed Electromagnetic Gas Acceleration, 8th Semi-Annual Progress Report for the period 1 January 1966 to 30 June 1966, Princeton University Aerospace and Mechanical Sciences Report No. 634g, July, 1966.

44. Electromagnetic Propulsion, Astronautics and Aeronautics 4, 69 (1966).

45. W. R. Ellis, Jr., "An Investigation of Current Sheet Structure in a Cylindrical Z-Pinch," Ph.D. thesis, Department of Aerospace and Mechanical Sciences, Princeton University, Princeton, New Jersey, 1967.

46. "Current Status of Plasma Propulsion," AIAA 2nd Propulsion Joint Specialist Conference, Colorado Springs, Colorado, 13-17 June 1966, AIAA Paper No. 66-565.

47. Pulsed Electromagnetic Gas Acceleration, 9th Semi-Annual Progress Report for the period 1 July 1966 to 31 December 1966, Princeton University Aerospace and Mechanical Sciences Report No. 634h, January, 1967.

48. Pulsed Electromagnetic Gas Acceleration, 10th Semi-Annual Progress Report for the period 1 January 1967 to 30 June 1967, Princeton University Aerospace and Mechanical Sciences Report No. 634i, July, 1967.

49. "Current Pattern Stabilization in Pulsed Plasma Accelerators," AIAA Electric Propulsion and Plasmadynamics Conference, Colorado Springs, Colorado, 11-13 September 1967, AIAA Paper No. 67-656.

50. An Investigation of Current Sheet Structure in a Cylindrical Z-Pinch, Princeton University Aerospace and Mechanical Sciences Report No. 805, July, 1967.

GENERAL REFERENCES

A-1 Mirels, H.: "Test Time in Low-Pressure Shock Tubes,"
     Phys. of Fluids 6, 1201-1214, September, 1963.

A-2 Milligan, M. W.: "Nozzle Characteristics in the Tran-
     sition Regime Between Continuum and Free Molecular Flow,"
     AIAA Journal 2, 1088-1091, June, 1964.

A-3 Mirels, H., and King, W. S.: "Lewis Solution for Shock-
     Tube Laminar Boundary Layer and Test Time," AIAA Journal 4,
     5, May, 1966.

A-4 Duff, R. E.: "Shock Tube Performance at Low Initial Pres-
     sure," Physics of Fluids 2, 2, March-April, 1959.

A-5 Dougal, A. A.: Bull. Am. Phys. Soc. (II), 8, 163 (1963).

A-6 Ashby, D. E. T. F., and Jephcott, D. F.: Appl. Phys.
     Letters 3, 1, 13 (1963).

A-7 Gerardo, J. B., Verdeyen, J. T., and Gusinow, M. A.: "Theory
     of the Laser Interferometer and Its Use in Plasma Diagnos-
     tics," Scientific Report No. 1, Grant No. DA-ARO-D-31-124-
     G582, University of Illinois, (1964).

A-8 Gerardo, J. B., and Verdeyen, J. T.: Appl. Phys. Letters 3,
     7, 121 (1963).

A-9 Sutton, G. W., and A. S. Sherman: "Engineering Magneto-
     hydrodynamics," p. 190, eq. 5.167, McGraw-Hill Book Company,
     New York, 1965.

A-10 Spitzer, L., Jr.: "Physics of Fully Ionized Gases," p. 139,
     eq. 5-37, 2nd ed., Interscience Publishers, New York, 1962.